Study on Ammonia Utilization and Alternative Anode Materials for Solid Oxide Fuel Cells

Ahmed Fathi Salem Molouk

2016

Study on Ammonia Utilization and Alternative Anode Materials for Solid Oxide Fuel Cells

Ahmed Fathi Salem Molouk

Department of Energy and Hydrocarbon Chemistry

Graduate School of Engineering

Kyoto University

Kyoto, Japan

2016

Contents

General Introduction

Background of the work

1. Ecosystem and renewable energy

Greenhouse gases are constituents of the atmosphere. They exist naturally as water vapour, carbon dioxide, methane, nitrous oxide, and ozone or anthropogenic such as halocarbons, sulphur hexafluoride (SF_6), and other chlorine and bromine-containing substances. Greenhouse gases effectively absorb thermal infrared radiation emitted by the earth's surface and then release it in all directions including downward to the earth's surface. Thus, greenhouse gases trap heat within the surface-troposphere system causing what so–called greenhouse effect. The natural greenhouse effect is indispensable for supporting life and maintaining the balance in earth's temperature. An increase in the concentration of greenhouse gases caused by human activity mainly burning of fossil fuels to produce energy leads to increase the opacity of the atmosphere for infrared radiation (global warming) which has fatal consequences for ecosystem.

Increasing demand in electrical energy at the same time with growing concern environmentally and economically from the use of fossil fuels is a motivation to find a new green source for the production of electricity. Fuel cells are one of the most promising candidates for solving this dilemma. We have to admit that the average output of power generation system based on fossil fuels is still higher than that for system based on the renewable energy. However, fuel cells demonstrated higher efficiency as compared with other power generation system[1, 2] (see Fig. 1).

Fuel cells are electrochemical devices converting the chemical energy directly to the electrical energy and heat without passing through other energy forms, which ensures high efficiency for energy conversion. Since the fourth decade in 19th century the concept of fuel

cells was established. In 1839, Christian Friedrich discovered the possibility of a fuel cell that combined hydrogen with oxygen [3]. In the same year, Sir Grove published his work about the observation of voltage output in a concentration cell with combining hydrogen and oxygen in the presence of platinum and it was called as "gas cell" at that time [4]. There are two basic differences between fuel cells and rechargeable batteries. Fuel cells use gaseous or liquid reactants for the reactions instead of solid reactants. The other difference is that fuel cells can be operated for a long time without a need for periodic replacement or recharging if the reactant is continually supplied and the reaction products are continually removed. The most common classification of fuel cells was based on the electrolyte type. Among various types of fuel cells, solid oxide fuel cells (SOFCs) have huge advantages such as high energy conversion efficiency, high power density, long term stability, and high fuel flexibility [2, 5–7]. Solid oxide fuel cells can be fed directly with variety of fuels beside H_2; *e.g.* hydrocarbons can be directly supplied to the anode without the external reforming process because of high operating temperature of SOFC.

2. Working principle and components of solid oxide fuel cells

2. 1. Working principle of solid oxide fuel cells

Both designs of planar- and tubular-type SOFCs fundamentally consist of two porous electrodes separated by a dense oxygen ion or proton conducting electrolyte. The schematic diagram in Fig. 2 illustrates the working principle of SOFC using the oxygen ion conducting electrolyte with feeding hydrogen and oxygen as a fuel and an oxidant, respectively. Electrons from the cathode react with oxygen molecules at the triple phase boundary (TPB) to form oxygen ions (O^{2-}) (Eq. 1). According to the difference in oxygen partial pressure between anode and cathode, oxygen ions migrate through the oxygen conducting electrolyte

to the anode with the vacancy hopping mechanism. At the anode H_2 and O^{2-} react to generate steam in the gas-phase and then electrons are released to an external circuit (Eq. 2). The electrons produced at the anode from electrochemical oxidation of hydrogen will flow through the load and back to the cathode as long as a load is connected between the anode and cathode.

Cathode $\frac{1}{2}O_2 + 2e^- \rightleftharpoons O^{2-}$ (1)

Anode $H_2 + O^{2-} \rightleftharpoons H_2O + 2e^-$ (2)

Over all reaction $H_2 + \frac{1}{2}O_2 \rightleftharpoons H_2O$ (3)

The relationship between the chemical energy of fuel and the voltage of a fuel cell was established. Therefore, the ideal thermodynamic reversible voltage (E_{OCV}) of single cell under the open circuit condition can be estimated from Nernst equation (4)

$$E_{OCV} = E^o + \frac{RT}{nF} \ln\left(\frac{P_{H_2} P_{O_2}^{\frac{1}{2}}}{P_{H_2O}}\right) \quad (4)$$

where E^o is the standard cell voltage, R is the gas constant, T is the temperature, n is the number of transferred electron, F is the Faraday constant, P_{H_2O} is the partial pressure of H_2O at the anode, P_{H_2} is the partial pressure of H_2 at the anode, and P_{O_2} is the partial pressure of O_2 at the cathode. However, the actual cell voltage (E_{cell}) will be deviated from the open-circuit potential under operating conditions because of several internal irreversible losses (polarization losses). The actual cell voltage (E_{cell}) can be calculated from Eq. (5)

$$E_{\text{cell}} = E_{\text{OCV}} - \left(\eta_{\text{ohm}} + \eta_{\text{act,a}} + \eta_{\text{conc,a}} + \eta_{\text{act,c}} + \eta_{\text{conc,c}}\right) \quad (5)$$

As shown in equation (5) there are three major losses which are ohmic loss(η_{ohm}), anodic and cathodic activation overpotential ($\eta_{\text{act,a}}$, $\eta_{\text{act,c}}$) and anodic and cathodic concentration overpotential ($\eta_{\text{conc,a}}$, $\eta_{\text{conc,c}}$). They can be explained as follow;

(a) Activation overpotential (η_{act})

The activation loss is noticeable in the low current region and it is due to the slow electrochemical reactions at the electrode surface, where the species are oxidized or reduced in a fuel cell reaction. The activation overpotential can be represented by Eq. (6)

$$\eta_{\text{act}} = \frac{RT}{\alpha nF} \ln\left(\frac{i}{i_{\text{o}}}\right) \quad (6)$$

where α is the the charge transfer coefficient, i is the current density, and i_{o} is the exchange current density.

(b) Ohmic loss (η_{ohm})

The ohmic loss is originated from electronic and ionic resistivity of the fuel cell components. The ohmic loss increases over the entire range of current due to the constant nature of fuel cell resistance and it is represented by Eq. (7)

$$\eta_{\text{ohm}} = iR_{\text{cell}} \quad (7)$$

where R_{cell} is the cell resistance.

(c) Concentration overpotential (η_{conc})

The concentration overpotential is dominant at high limiting currents where the diffusion of reactant gas to the reaction sites and removal of reaction products from those sites become difficult. A concentration gradient in the system was formed because the reactant gas is consumed at the electrode through the electrochemical reaction. The concentration overpotential can be represented by Eq. (8).

$$\eta_{\mathrm{conc}} = \frac{RT}{nF} \ln\left(1 - \frac{i}{i_{\mathrm{lim}}}\right) \quad (8)$$

where i_{lim} is the limiting current density.

The activation, ohmic and concentration losses can be decreased by modifying component and the design of SOFCs.

2. 2. Solid oxide fuel cells components

2. 2. 1. Electrolyte

The name of SOFCs comes from using a dense solid ceramic electrolyte. Solid oxide fuel cells operate at high temperature (700–1000^{o}C) because of the ionic conductivity of solid ceramic electrolyte is low at ambient temperature [8, 9]. The research in SOFCs has started since discovering ionic conductivity at high temperature for the so-called “Nernst mass” of a ceramic material consisting of 85 mol% ZrO_2–15 mol% Y_2O_3 [10]. The dense solid ceramic electrolyte plays an essential role in conducting ionic species between electrodes. The current flow occurs by the movement of ions through the crystal lattice. This movement is a result of thermally activated hopping of the ions moving from one crystal lattice site to its neighbor site [11, 12]. Moreover, the electrolyte prevents the flow of electrons and the mixing of oxidant

and fuel. Until now yttria–stabilized zirconia (YSZ) remains the most conventional electrolyte material for SOFCs which provides high oxygen ion conductivity at temperature more than 700^{o}C. On the other hand, rare earth doped ceria and rare earth doped bismuth oxide have been widely investigated as electrolytes for an intermediate temperature solid oxide fuel cell [13–15] (500–800^{o}C). The electrolyte material should satisfy various requirements such as high ionic conductivity, the lowest level of electronic conduction, chemical stability over wide ranges of temperature and oxygen partial pressure, compatible thermal expansion coefficient with electrodes, and negligible interaction with electrode materials under operating and fabrication conditions [16].

2. 2. 2. Cathode

The cathode of solid oxide fuel cell is called an air electrode where oxygen is electrochemiccally reduced. The oxygen reduction reaction requires the presence of oxygen ion and electrons as shown in reaction (1). Therefore, the cathode material should be a good catalyst for oxygen reduction and needs to have following properties, high electronic conductivity, chemical stability under operating conditions, compatible thermal expansion coefficient with an electrolyte, and sufficient porosity to facilitate transport of molecular oxygen from the gas phase to the triple phase boundary (TPB) [17]. The perovskite–type oxide of Sr–doped $LaMnO_3$ (LSM) is the conventional cathode material for SOFCs.

2. 2. 3. Anode

The anode (fuel electrode) generally consists of electronic and ionic conductors. Usually, the electronic conductor is a metal and the ionic conductor is the same material of electrolyte to ensure the good contact between anode and electrolyte. Such a mixture is called a cermet. SOFC anodes have a dual role one is to provide an active reaction sites for the

electrochemical reaction and the other is to provide a path for electrons to transfer from reaction sites to the external circuit. Nickel is the conventional metallic component in the anode cermet because of its high catalytic activity for fuel oxidation, high electronic conductivity, low cost, and high stability under reducing conditions. However, nickel metal suffers from some disadvantages such as sintering at high temperature and during the long-term operation, and the decline in catalytic activity because of sulphur poisoning and carbon deposition in the case of using hydrocarbon fuels [18].

The reaction mechanism over the anode is extremely complex because of many parameters governing this reaction. However, understanding the mechanism of fuel oxidation over the anode and revealing the chemical and electrochemical kinetics are the key factors for the optimization of anodes and operating conditions.

The hydrogen-spillover mechanism over Ni anode was first discussed by Mogensen [19] which can be explained by the following steps;

(1) Adsorption on the nickel surface

$$H_2(g) + 2(Ni) \rightleftharpoons 2H(Ni)$$

(2) Dissociation of adsorbed hydrogen on the Ni surface

$$2H(Ni) \rightleftharpoons 2H^+(Ni) + 2e^-$$

(3) Diffusion of adsorbed proton, $H^+(Ni)$, to the TPB

(4) Charge transfer reaction at the TPB region

$$H^+(Ni) + O^{2-}(electrolyte) \rightleftharpoons (Ni) + OH^-(electrolyte)$$

(5) Formation of water on the electrolyte surface

$$2OH^-(electrolyte) \rightleftharpoons H_2O(g) + O^{2-}(electrolyte) + (electrolyte)$$

However, other researchers proposed different mechanisms for electrochemical hydrogen oxidation depending on different operating and anode preparation conditions [20–26].

3. Ammonia as a promising fuel for SOFCs

As described earlier, the fuel flexibility is one of the most important advantages for SOFCs which makes it unique among other types of fuel cells and renewable power generation systems. Pure H_2 is the cleanest fuel ever known and H_2O is the only product of its combustion. However, the commercialization of H_2 as a fuel has been restrained due to obstacles related to production, storage, and safety problems. Hydrogen provides extremely low volumetric energy density [27, 28]. For the reasons described above, hydrocarbons are preferable as a fuel especially for SOFCs. However, the carbon which produced as a by-product from hydrocarbons will cause a severe damage on SOFC performance and long-term stability of the anodes [29–35]. Much effort was devoted to overcome the carbon deposition problem thermodynamically or to design anode materials with high tolerant to carbon deposition [36]. However, the cell performance in hydrogen is much higher than that in hydrocarbons.

Ammonia recently attracted a great attention to use it as a fuel for SOFCs. This is because ammonia has various advantages, such as a carbon free fuel, high safety in handling, ease in storage and transportation (Ammonia can be liquefied at room temperature and at pressures of 8-10 bar) [37]. Furthermore, ammonia has high energy density which is comparable to that of natural gas [38, 39]. Therefore, ammonia is considered as a viable and alternative fuel for fuel cells.

4. Direct NH_3–Fueled SOFCs

4. 1. NH_3 utilization within SOFCs

Two possible mechanisms can be considered for the utilization of ammonia as a fuel in SOFCs; direct ammonia oxidation as in Eq. (9) and two–step process as in Eqs. (10) and (11).

$$4NH_3(g) + 3O_2(g) \rightleftharpoons 2N_2(g) + 6H_2O(g) \quad (9)$$

$$2NH_3(g) \rightleftharpoons N_2(g) + 3H_2(g) \quad (10)$$

$$2H_2(g) + O_2(g) \rightleftharpoons 2H_2O(g) \quad (11)$$

Fuerte *et al.* have studied the effect of operating temperature on the open circuit voltage (OCV) with feeding ammonia or hydrogen fuels to the commercial microtubular SOFC, Ni–YSZ | YSZ | LSM. The experimental OCV essentially decreased with increasing temperature under both humidified hydrogen and ammonia supplied conditions. On the other hand, the theoretical OCV for the direct ammonia oxidation as in Eq. (9) increases with a rise in temperature [40]. This means that NH_3 follows the two–step process over anode; NH_3 is catalytically decomposed to H_2 and N_2 and then H_2 produced is electrochemically oxidized over anode.

4. 2. NH_3– fueled SOFCs based on oxygen-conducting electrolytes

There are many studies focusing on the performance of NH_3– fueled SOFCs. There are some efforts have been conducted to enhance the cell performance by using different anode materials, and thinner electrolytes.

Wojcik *et al.* used a tubular SOFC based on 200 µm-thick YSZ electrolyte for the power generation [41]. They prepared three different anodes, Pt, Ag and Ag with Fe catalyst. Tests

were conducted at 973-1273 K. The cathode was Ag for all cells. They found that ammonia can be directly used as a fuel in a SOFC based on silver anode without iron catalyst. When silver anode was coupled with Fe catalyst, the performance of SOFC in NH_3 was comparable to that in H_2 fuel. Furthermore, the power density increased significantly by using platinum anode.

Fournier and co–worker used 1000 µm-thick YSZ and 400 µm-thick calcia stabilized zirconia (CaSZ) electrolytes to prepare a tubular and pellet design cells, respectively [42]. Silver, platinum, and nickel cermets were used as anodes. At 800^{o}C, the nickel cermet achieved the ammonia conversions of more than 90%, which was significantly higher than those obtained with silver and platinum.

Zhang *et al*. fabricated an anode-supported tubular SOFC using 15µm-thick YSZ electrolyte, Ni–YSZ anode, and YSZ–LSM cathode [43]. They found that at 800^{o}C, the peak power densities were 202 and 200 mW cm^{-2} in H_2 and NH_3 fuels, respectively and by increase operating temperature, the performance of the cell running on NH_3 approached to that of the cell in H_2 fuel. The effluent from the anode contained considerable amounts of nitrogen and hydrogen, but no trace of NO_x was detected when NH_3 was used as a fuel.

Another study was carried out by Qianli and co-worker with using anode-supported cell (ASC) based on thin YSZ electrolyte (*ca*. 30µm in thickness) 60 wt.% Ni–YSZ anode and YSZ–LSM cathode [44]. The liquefied ammonia was directly supplied to the anode and the cell was operated at 650-850^{o}C. The maximum power densities were 299 and 526 mW cm^{-2} at 750^{o}C and 850^{o}C, respectively. These values were, slightly lower than those fueled with hydrogen. The analysis of open current voltages (OCVs) of the cell indicated the oxidation of ammonia proceeded via a two-step process. Impedance spectra showed the electrolyte resistance was comparable to each other both in ammonia and hydrogen, but the interfacial polarization resistance was slightly larger in the ammonia fuel.

The mixed ionic–electronic conductive electrolyte was tested in the NH_3. Liu *et al.* compared the cell performances with feeding liquid methanol, ammonia and hydrogen as fuels. The cell configuration used was as follows, 60 wt. % Ni–SDC | 24 μm–thick SDC | $Sm_{0.5}Sr_{0.5}CoO_3$ (SSC)–SDC cathode [45]. At 650°C, the obtained peak power densities were 698, 870, and 467 mW cm^{-2} in CH_3OH, NH_3, and H_2 fuels, respectively.

Qianli *et al*. also used a thin SDC electrolyte (*ca*. 50 μm in thickness), 35 wt. % Ni–SDC anode and SSC–SDC cathode [46]. Maximum power densities were 168.1 and 191.8 mW cm^{-2} at 600^{o}C in NH_3 and H_2 fuels, respectively. Furthermore, the outlet gas was examined in this study and NO gas was not detected at different operating temperatures and NH_3 flow rates.

Meng *et al*. fabricated a cell consisting of 10 μm-thick SDC electrolyte, 50 wt. % Ni–SDC anode and $Ba_{0.5}Sr_{0.5}Co_{0.8}Fe_{0.2}O_{3-\delta}$ (BSCF) cathode [47]. A peak power density of 1190 and 1872 mWcm^{-2} was obtained in ammonia and hydrogen fuels, respectively at 650 °C. The observed power density was the highest among reported in the literature.

Wang *et al*. proved that NH_3 is not only a promising fuel but also suppress the coke formation in the anode when it is mixed with methane [48].

4. 3. NH_3– fueled SOFCs based on proton-conducting electrolytes

The working principle of SOFCs based on proton-conducting and oxygen-conducting electrolytes is similar. However, the steam is produced at the cathode for a SOFC based on a proton-conducting electrolyte while at the anode in the case of a SOFC based on an oxygen-conducting electrolyte [49]. The thermodynamic analysis of NH_3–fueled SOFCs was reported by Ni *et al* [50]. According to thermodynamic calculations, the equilibrium potential of a SOFC based on a proton-conducting electrolyte is significantly higher than that of a SOFC based on an oxygen-conducting electrolyte. Moreover, this difference in equilibrium potential between two cells increased with increasing the fuel utilization. They mentioned that the

higher performance of an NH_3–fueled SOFC based on a proton-conducting electrolyte is caused by the higher hydrogen partial pressure. In a SOFC based on an oxygen-conducting electrolyte, steam is produced at the anode which leads to the dilution of the fuel concentration. Another advantage of using a SOFC based on a proton-conducting electrolyte is that the chances of producing NO_x are significantly reduced since oxygen ions are not conducted through the electrolyte [47, 51]. Table 1 summarizes the peak power density for NH_3–fueled SOFCs based on proton-conducting electrolyte.

5. Ammonia thermal catalytic decomposition

Ammonia is an excellent hydrogen carrier and it can be used directly as a fuel for SOFCs. Because of high operating temperature of SOFCs, hydrogen can be generated from NH_3 by the thermal decomposition or the catalytic cracking.

The ammonia decomposition reaction is an endothermic reaction with ΔH = 46.19 kJ/mol. The reaction (10) proceeds to the right as the temperature increases or to the left as the pressure increases. Therefore, the decomposition of ammonia is favourable at high temperature and low pressure [60]. Ammonia is unstable at high temperature and decomposes at 200^{o}C [61]. The equilibrium conversion of NH_3 at different temperatures under normal pressure (1atm) can be calculated [62] using Eq. (12);

$$\left[40100 - (25.46T \times \ln T) + (0.00917T^2) - \left(\frac{103000}{T}\right) + 64.81T\right] = -RT \ln\left[\frac{1.3X^2}{(1-X^2)}\right] \quad (12)$$

where T is the reaction temperature (K) and X is the equilibrium NH_3 conversion (%).

NH_3 can be converted thermodynamically to H_2 and N_2 at temperatures as low as 200^{o}C. However, in practice, the conversion depends on temperature as well as catalysts [63].

5. 1. Effect of metal catalyst on NH_3 conversion

It was found that ammonia decomposition rate depends greatly on metal catalysts. Papaolymerou *et al.* [64] studied the NH_3 decomposition over polycrystalline wires or foils of Pd, Ir, Pt, and Rh at the partial pressure of NH_3 of 1 Torr. The order of the catalytic activity for NH_3 conversion at 227–927^oC was as follows, Ir > Rh > Pt > Pd. Ammonia conversion and hydrogen formation rate over different metal catalysts were studied by Goodman and co–workers [65]. They found that the catalytic activity for NH_3 decomposition was in the order of Ru>Ir>Ni when the metal loading was equal.

Shuang-Feng Yin *et al*. conducted a systematic investigation on the effects of active metals (Ru, Rh, Pt, Pd, Ni, Fe) supported on CNTs for NH_3 conversion [62]. They found that the NH_3 conversion over Ru is much higher than those over the other metals. Moreover, TOFs data revealed that Ru is the most active catalyst and the order was Ru > Rh ≈ Ni > Pt ≈ Pd > Fe. Furthermore, the formation of inactive ruthenium nitride was not detected during ammonia catalytic decomposition reaction. Thus, Ruthenium metal is a favourable catalyst for ammonia conversion. However, nickel is a cheap metal and directly come after Ru, Ir, and Rh in activity for ammonia decomposition.

The differences in activity of these metal catalysts can be explained by the reaction kinetics. Usually, it was considered that the rate-determining step for ammonia decomposition reaction is desorption of the nitrogen. Therefore, the catalytic activity of metals for ammonia decomposition reaction depend on the apparent activation energy (E_a) for desorption of the nitrogen [64, 65].

In the case of iron catalysts, it was suggested that the active component was unstable FeN_x [66]. Although the characteristics of some metal nitrides and carbides are qualitatively similar to those of noble metals, nitrides and carbides show much lower catalytic activity for NH_3 decomposition [67, 68].

5. 2. Effect of support on NH_3 conversion

Usually the support is used to enhance the dispersion and surface area of the active metal catalyst. A good support should be stable under reaction conditions and has high specific surface area. S.F. Yin *et al.* revealed that the catalytic performance of Ru catalyst for NH_3 conversion was dependent on the support materials [62]. The order of catalytic activity was Ru/CNTs > Ru/MgO > Ru/TiO_2 ≈ Ru/Al_2O_3 ≈ Ru/ZrO_2 > Ru/AC. Thus, Ru/CNTs was the most active catalyst for NH_3 conversion and three main reasons can be considered for this matter as follows;

(i) The high dispersion and smaller particle size of Ru were demonstrated on CNTs support.

(ii) The utilization of conductive support is preferable for transferring the electrons from support to metal catalyst, which promotes the recombinative desorption of surface N atoms

(iii) The support with strong and sufficient basic sites is highly favourable for high catalytic efficiency of NH_3 conversion.

Zhong and Aika [69] found that the elimination of electronegative impurities such as S, N, O, and Cl from activated carbon support by heating commercial activated carbon (AC) in hydrogen at 800^{o}C for 12 h had a promotion effect on the catalytic behaviour of the supported catalyst for NH_3 conversion.

Therefore, it was proven that basicity, conductivity, surface area, concentration of electron-withdrawing groups, and thermal stability of supports are important parameter which directly affect ammonia conversion.

5. 3. Effect of promoted cations on NH_3 conversion

It was found that introducing alkali, alkaline earth, or rare earth metal ions to supported Ru or Fe catalysts were beneficial for promoting ammonia synthesis [70, 71]. Therefore, Wang *et al*. studied the effect of rare earth, alkali, and alkaline earth elements on the catalytic activity of ruthenium supported carbon nanotubes (Ru/CNTs) for ammonia decomposition [72]. The catalytic activity of modified catalysts for NH_3 decomposition was in the following order, K–Ru > Na–Ru > Li–Ru > Ce–Ru > Ba–Ru > La–Ru > Ca–Ru > Ru. They concluded that the ammonia decomposition increased as the electro-negativity of the promoter decreased and the promoter effectively prevented the sintering of Ru metal catalyst. On the other hand, the catalytic activity of Ru for ammonia decomposition was inhibited by electron-withdrawing groups such as F^-, Cl^-, Br^-, SO_4^{2-}, and PO_4^{3-}.

5. 4. Kinetics and mechanism of catalytic decomposition of ammonia

The reaction steps for ammonia decomposition (Eq. 13–15) includes the adsorption of ammonia onto active sites of catalyst surface (*), the splitting of N–H bond for adsorbed ammonia, and the recombinative desorption of N_2 atoms [63].

$$NH_3 + * \rightarrow NH_3^* \quad (13)$$

$$NH_3^* + * \rightarrow NH_2^* + H^* \quad (14)$$

$$2N^* \rightarrow N_2 + 2\,^* \quad (15)$$

Bradford *et al* [73] found that the rate of NH_3 decomposition over Ru/C catalyst at 370–390 °C and NH_3 partial pressure of 1.3–12.0 kPa followed the equation (16):

$$r = kP_{\mathrm{NH_3}}^{\alpha} P_{\mathrm{H_2}}^{\beta} \quad (16)$$

where r is the rate of ammonia decomposition reaction, P_{NH_3} and P_{H_2} are the partial pressure of ammonia and hydrogen, respectively, k, α, and β are constants. The value of α varied from 0.69 to 0.75 and β varied from -1.5 to -2.0. The above equation suggested the strong inhibition effect of hydrogen partial pressure on the thermal decomposition of NH_3 at temperature below 400^{o}C.

Outline of the work

Recently ammonia emerged as a suitable fuel for solid oxide fuel cells. Therefore, it is important to investigate the catalytic and electrochemical behaviour of ammonia fuel within SOFCs. This work was dedicated to understand the utilization of ammonia over SOFC anode. This systematic investigation helps in designing an active anode for direct NH_3–fueled SOFCs. This thesis consists of five chapters.

In Chapter 1, the conventional electrolyte supported cell of Ni–YSZ | YSZ | LSM was prepared and its performance was investigated in hydrogen, ammonia and methane fuels under almost the same partial pressure of oxygen at different temperatures. The mechanism of ammonia utilization within SOFC was confirmed. Furthermore, the kinetics study on ammonia decomposition over Ni–YSZ anode was conducted at 600^{o}C and 850^{o}C.

In Chapter 2, the performance of SOFCs with Ni–yttria-stabilized zirconia (Ni–YSZ) and Ni–gadolinia-dope ceria (Ni–GDC) cermet anodes fueled with H_2 or NH_3 was investigated in terms of the catalytic activity of ammonia decomposition. The effect of preparation method of Ni–GDC anode on the cell performance was studied in ammonia and hydrogen fuels.

In Chapter 3, Ru–promoted Ni–GDC anode was prepared by the infiltration technique and the electrochemical performance was studied and compared with that of Ni–GDC and Fe–promoted Ni–GDC anodes with supplying hydrogen and ammonia fuels.

In Chapter 4, the cell with a proton conducting electrolyte was prepared. Ni–$BaCe_{0.75}Y_{0.25}O_{3-\delta}$ (Ni–BCY25) was investigated as an anode for direct NH_3–fueled solid oxide fuel cells. The poisoning effect of water and hydrogen on ammonia decomposition reaction over Ni–BCY25 was evaluated.

In Chapter 5, stability study of Ni–YSZ anode for direct NH_3–fueled SOFCs was conducted. The influence of ammonia exposure on the microstructure of Ni was investigated.

References

[1] A. B. Stambouli, E. Traversa, *Renew. Sust. Energ. Rev.*, **6**, 297–306 (2002).

[2] A. Kirubakaran, S. Jain, R.K. Nema, *Renew. Sust. Energ. Rev.*, **13,** 2430–2440 (2009).

[3] C. F. Schoenbein, *Phil. Mag. (III)*, **14,** 43–45 (1839).

[4] W. R. Grove, *Phil. Mag. (III)*, **14**, 127–130 (1839).

[5] X. Huang, Z. Zhang, J. Jiang, *IEEE Symposium on Industrial Electron*, 1613–1618 (2006).

[6] M.W. Ellis, M.R. Von Spakovsky, D.J. Nelson, *IEEE Proc.*, **89**, 1808–1818 (2001).

[7] M. Farooque, H.C. Maru, *IEEE Proc.*, **89**, 1819–1829 (2001).

[8] J.M. Dixon, L.D. LaGrange, U. Merten, C.F. Miller, J.T. Porter, *J. Electrochem. Soc.*, **110**, 276–280 (1963).

[9] B. Bagchi, R. N. Basu, *J. Alloys Compd.*, **647**, 620–626 (2015).

[10] W. Nernst, US patent 685 730, filed on August 24, (1899).

[11] P.S. Manning, J.D. Sirman, R.A. De Souza, J.A. Kilner, *Solid State Ionics* **100**, l–10 (1997).

[12] C. León, M. L. Lucía, and J. Santamaría**,** *Phys. Rev. B***, 55,** 882 (1997).

[13] M. A. Khan, R. Raza, R. B. Lima, M. A. Chaudhry, E. Ahmed, G. Abbas, *Int. J. Hydrogen Energ.*, **38,** 16524–16531 (2013).

[14] Y. Jing, J. Patakangas, P. D. Lund, B. Zhu, *Int. J. Hydrogen Energ.*, **38**, 16532–16538 (2013).

[15] S. S. Baek, N. Lee, B. K. Kim, H. Chang, S. Song, J. Y. Park, *Int. J. Hydrogen Energ,* **37** 16823–16834 (2012).

[16] J. W. Fergus, *J. Power Sources*, **162**, 30–40 (2006).

[17] R. Pelosato, G. Cordaro, D. Stucchi, C. Cristiani, G. Dotelli, *J. Power Sources*, **298** 46–67 (2015).

[18] S. P. S. Shaikh, A. Muchtar, M. R. Somalu, *Renew. Sust. Energ. Rev.*, **51**, 1–8, (2015).

[19] M. Mogensen, S. Skaarup, *Solid State Ionics*, **86-88**, 1151–1160 (1996).

[20] C. Sun, U. Stimming, *J. Power Sources*, **171**, 247–260 (2007).

[21] R. E. Williford, L. A. Chick, G. D. Maupin, S. P. Simner, J. W. Stevenson, *J. Electrochem. Soc.*, , **150**, A1067–A1072 (2003).

[22] J. Mizusaki, H. Tagawa, T. Saito, K. Kamitani, T. Yamamura, K. Hirano, S. Ehara, T. Takagi, T. Hikita, M. Ippommatsu, S. Nakagawa, K. Hashimoto, *J. Electrochem. Soc.*, **141**, 2129–2134 (1994).

[23] A. Bieberle, L. J. Gauckler, *Solid State Ionics* , **146**, 23–41 (2002).

[24] W. Y. Lee, D. Wee, A. F. Ghoniem, *J. Power Sources*,**186**, 417–427 (2009).

[25] S. P. Jiang, S. P. S. Badwal, *Solid State Ionics,* **123**, 209–224 (1999).

[26] S. P. Jiang, S. P. S. Badwal, *J. Electrochem. Soc.*, **144**, 3777– 3784 (1997).

[27] C. Zamfirescu, I. Dincer, *Fuel Process. Technol.*, **90**, 729–737 (2009).

[28] A.S. Chellappa, C.M. Fischer, W.J. Thomson, *Appl. Catal. A: Gen.*, **227**, 231–240 (2002).

[29] Hyuk Kan, Hyunjoo Lee, *App. Catal. B: Environ.*, **97**, 108–114 (2010).

[30] Caine M. Finnerty, Neil J. Coe, Robert H. Cunningham, R. Mark Ormerod, *Catal.Today*, **46**, 137-145 (1998).

[31] Kasra Nikooyeh, Ryan Clemmer, Vanesa Alzate-Restrepo, Josephine M. Hill, *Appl.Catal. A: Gen.*, **347**, 106–111 (2008).

[32] Nikolaos C. Triantafyllopoulos , Stylianos G. Neophytides, *J.Catal*., **217**, 324–333 (2003).

[33] S. McIntosh, J. Gorte, *Chem. Rev*., **104**, 4845-4865 (2004).

[34] Robert J. Kee, Huayang Zhu, David G. Goodwin, *Procee. Combus. Inst*., **30**, 2379–2404 (2005).

[35] Nikolaos C. Triantafyllopoulos, Stylianos G. Neophytides, *J. Catal*., **239**, 187–199 (2006).

[36] Gang Chen, Guoqing Guan, Shawket Abliz, Yutaka Kasai, Abuliti Abudula, *Electrochim. Acta*, **56**, 9868– 9874 (2011).

[37] Claus Hviid Christensen , Tue Johannessen b,Rasmus Zink Sørensen , Jens K. Nørskov, *Catal. Today*, **111**, 140–144 (2006).

[38] C. Zamfirescu, I. Dincer, J. Power Sources, **185**, 459–465 (2008).

[39] V. Hacker and K. Kordesch, , *Handbook of Fuel Cells – Fundamentals, Technology and Applications*, **3**, Part 2, 121–127 (2003).

[40] A. Fuerte et al., *J. Power Sources*, **192**, 170–174 (2009).

[41] A. Wojcik, H. Middleton, I. Damopoulos, J. Van herle, *J. Power Sources*, **118**(1–2):342–348 (2003).

[42] G.G.M. Fournier, I.W. Cumming, K. Hellgardt, *J. Power Sources*, **162**, 198–206 (2006).

[43] L. Zhang, Y. Cong, W. Yang, L. Lin, *Chin. J. Catal.*, **28**, 749–751 (2007).

[44] Q. Ma, J. Ma, S. Zhou, R. Yan, J. Gao, G. Meng, *J. Power Sources*, **164**, 86–89 (2007).

[45] M. Liu, R. Peng, D. Dong, J. Gao, X. Liu, G. Meng, *J. Power Sources*, **185**:188–192 (2008).

[46] Q. Ma, R. Peng, L. Tian, G. Meng, *Electrochem. Comm.*, **8**, 1791–1795 (2006).

[47] G. Meng, C. Jiang, J. Ma, Q. Ma, X. Liu, *J. Power Sources*, **173**, 189–193 (2007).

[48] W. Wang, R. Ran, C. Su, Y. Guo, D. Farrusseng, Z. Shao, J. Power Sources, **240**, 232–240 (2013).

[49] M. Ni, M. K. H. Leung, D. Y. C. Leung, *Int. J. Energy Res.*, **33**, 943–959 (2009).

[50] M. Ni, D. Y.C. Leung, M. K.H. Leung, *J. Power Sources*, **183**, 682–686 (2008).

[51] N. Maffei, L. Pelletier, J.P. Charland , A. McFarlan, *J. Power Sources*, **162**, 165–167 (2006).

[52] L. Pelletier, A. McFarlan, N. Maffei, *J. Power Sources*, **145,** 262–265 (2005).

[53] N. Maffeia, L. Pelletier, J.P. Charland, A. McFarlan, *J. Power Sources*, **140**, 264–267 (2005).

[54] N. Maffei, L. Pelletier, A. McFarlan, *J. Power Sources*, **175**, 221–225 (2008).

[55] Q. Ma, R. Peng, Y. Lin, J. Gao, G. Meng, *J. Power Sources*, **161**, 95–98 (2006).

[56] L. Zhang, W. Yang, *J. Power Sources*, **179**, 92–95 (2008).

[57] Y. Lin, R. Ran, Y. Guo, W. Zhou, R. Cai, J. Wang, Z. Shao, int. *J. hydrogen energy*, **35**, 2637–2642 (2010).

[58] K. Xie, Q. Ma, B. Lin, Y. Jiang, J. Gao, X. Liu, G. Meng, *J. Power Sources*, **170**, 38–41 (2007).

[59] K. Xie, R. Yan, G. Meng, X. Liu, *Ionics*, **15**, 115–119 (2009).

[60] F. Ishak, I. Dincer, C. Zamfirescu *J. Power Sources*, **202**, 157– 165 (2012).

[61] R. Lan, J. T.S. Irvine, S. Tao, *int. j. hydrogen energy*, **37**, 1482-1494 (2012).

[62] S. F. Yin, Q. Zhang, B. Xu, W. Zhu, C. Ng, C. Au, *J. Catal*, **224**, 384–396 (2004)

[63] S. F. Yin, B.Q. Xu, X.P. Zhou, C.T. Au, *Appl. Catal. A: Gen.*, **277**, 1–9 (2004).

[64] G. Papapolymerou, V. Bontozoglou, *J. Mol. Catal. A: Chem*., **120**,165–171 (1997).

[65] T. V. Choudhary, C. Svadinaragana, D.W. Goodman, *Catal. Lett*., **72**, 197–201 (2001).

[66] W. Arabczyk, J. Zamlynny, *Catal. Lett*., **60**, 167–171 (1999).

[67] J. G. Choi, J. Ha, J.W. Hong, *Appl. Catal. A: Gen*., **168**, 47–56 (1998).

[68] C. Liang,W. Li, Z. Wei, Q. Xin, C. Li, *Ind. Eng. Chem. Res*., **39**, 3694–3697 (2000).

[69] Z. H. Zhong, K. Aika, *J. Catal*., **173**, 535–539 (1998).

[70] S. Murata, K. Aika, *J. Catal*., **136**, 110–117 (1992).

[71] Z. H. Zhong, K. Aika, *Inorg. Chim. Acta*, **280**, 183–188 (1998).

[72] S. J. Wang, S.F. Yin, L. Li, B.Q. Xu, C.F. Ng , C.T. Au , *Appl. Catal. B: Environ*., **52**, 287–299, (2004).

[73] M. C. J. Bradford, P. E. Fanning, M. A. Vannice, J. Catal., **172**, 479–484 (1997).

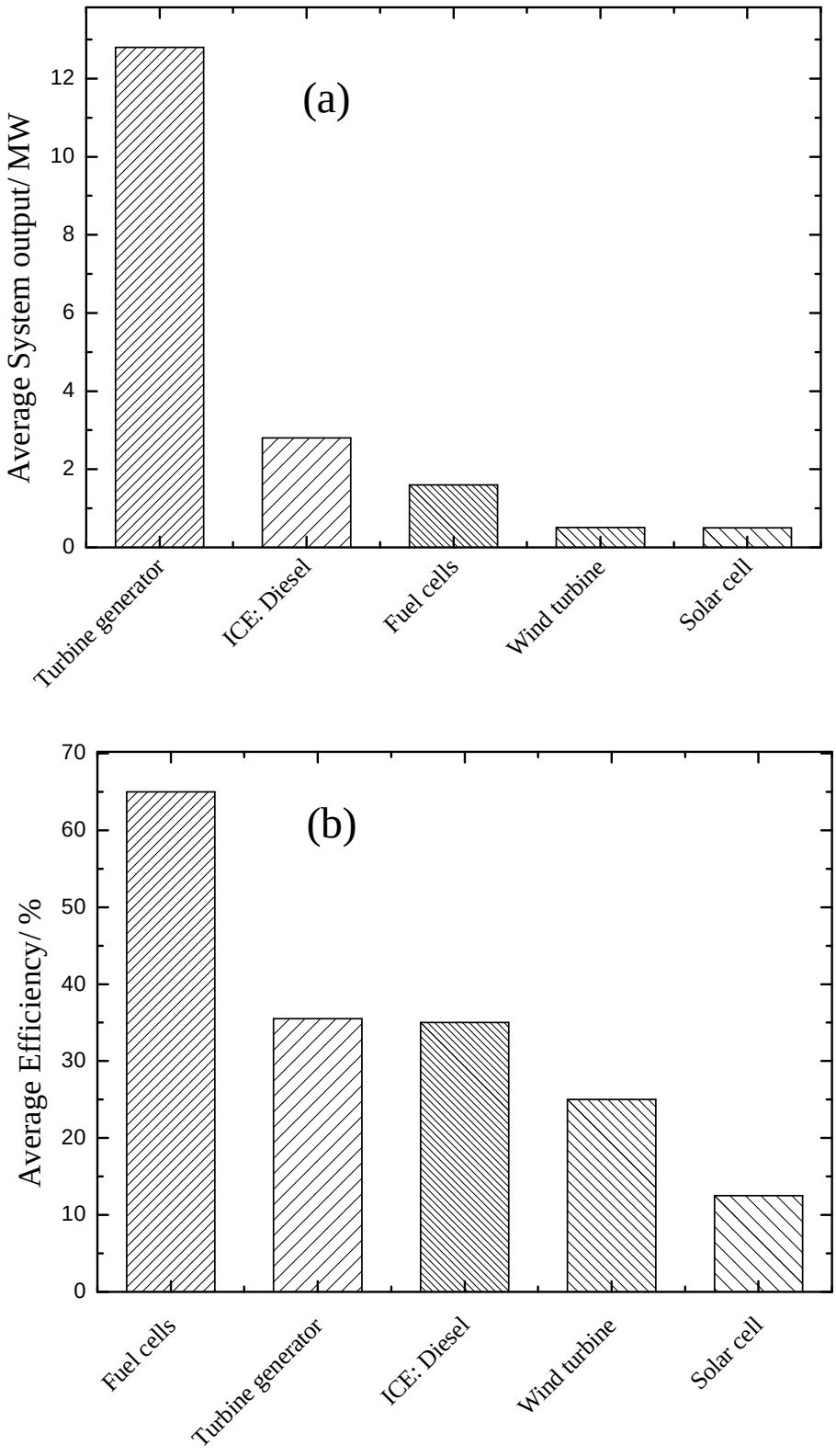

Figure 1. Average (a) system output and (b) efficiency of different power generation systems.

ICE: Diesel, abbreviation for internal combustion engine work in diesel.

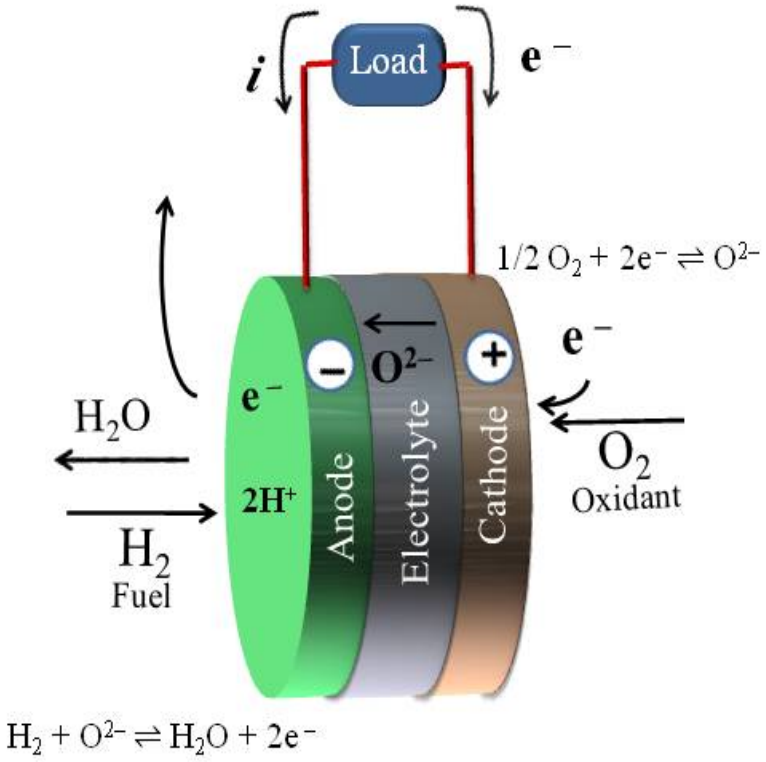

Figure 2. Primary components and functions of an SOFC.

Table 1

Peak power density for NH_3–fueled SOFCs based on proton-conducting electrolytes.

SOFC–H^+ System (anode/electrolyte/cathode)	Electrolyte Thickness (μm)	Fuel	Oxidant	Temperature (^oC)	Power Density (mW/cm^2)	REF
Pt|BCE|Pt	1000	NH_3	Air	700	32	51
Pt|BCGP|Pt	1300	NH_3	Air	700	35	52
Pt|BCGO|Pt					25	
Pt|BCGP|Pt	1300	NH_3	Air	700	40	53
Ni–BCE|BCGP|Pt	1000	NH_3	Air	600	28	54
Pt|BCGP|Pt					23	
Ni–BCGO|BCGO|LSCO–BCGO	50	Liquid ammonia	97% O_2/3% H_2O	750	384	55
Ni–CGO|BCGO|BSCFO–CGO	30	Liquid ammonia	O_2	650	200	56
Ni–BZCY|BZCY|BSCFO	35	NH_3	Air	750	400	57
Ni–BCNO|BCNO|LSCO–BCNO	20	Liquid ammonia	Air	700	315	58
Ni–BCSO| BCSO|NSMO	10	NH_3	O_2	700	540	59

BCE = $BaCe_{0.85}Eu_{0.15}O_{3-\delta}$ BCGP = $BaCe_{0.8}Gd_{0.19}Pr_{0.01}O_{3-\delta}$ BCGO = $BaCe_{0.8}Gd_{0.2}O_{2.9}$

LSCO = $La_{0.5}Sr_{0.5}CoO_{3-\delta}$ CGO = $Ce_{0.8}Gd_{0.2}O_{1.9}$ BSCFO = $Ba_{0.5}Sr_{0.5}Co_{0.8}Fe_{0.2}O_{3-\delta}$

BZCY = $BaZr_{0.1}Ce_{0.7}Y_{0.2}O_{3-\delta}$ BCNO = $BaCe_{0.9}Nd_{0.1}O_{3-\delta}$ BCSO = $BaCe_{0.8}Sm_{0.2}O_{3-\delta}$

NSMO = $Nd_{0.7}Sr_{0.3}MnO_{3-\delta}$

Chapter 1

Electrochemical and Catalytic Behaviors of Ni–YSZ Anode for the Direct Utilization of Ammonia Fuel in Solid Oxide Fuel Cells

1. 1. Introduction

Nowadays one of the most important challenges is producing energy from clean, renewable, durable, efficient and economically feasible sources. Solid oxide fuel cells (SOFCs) meet these goals. Variety of fuels can be used without the external reforming process because of high operating temperature of SOFCs [1-3]. Hydrogen is an ideal energy carrier and water is the only product of its combustion. For the massive utilization of hydrogen, however, there are still some difficulties in production, transportation, storage, and safety control [4, 5]. Therefore, it is important to use hydrogen containing chemicals such as methane, ethanol and ammonia as alternative fuels.

Methane has been studied extensively as a fuel for direct internal reforming SOFCs due to higher energy density compared to hydrogen. In SOFCs, Ni–based cermet anodes such as Ni–YSZ are widely used because nickel is a good catalyst for methane steam reforming as well as electrochemical hydrogen oxidation. However, the low tolerance to carbon deposition of Ni–based cermets is the main obstacle for the direct use of methane. In most of cases, the excess amount of steam is added to the fuel gas to prevent the coke formation, leading to the reduction in the energy conversion efficiency. The development of alternative anodes such as copper–based and perovskite–based materials will be a fundamental solution to this matter [6, 7]. At the current state, however, the catalytic activity of these anodes for methane steam reforming is not sufficiently high [8-10]. The cell performance is also insufficient for the practical application since this catalytic activity significantly affected the hydrogen

concentration in the vicinity of anode [11, 12].

Recently ammonia was proven as one of the promising hydrogen carriers for SOFCs because of following reasons; high energy density comparable to that of methane [4], carbon free, ease in liquefaction at ambient temperature, low production cost, and ease in leakage detection [13-17]. The ammonia decomposition reaction is an endothermic process with an enthalpy of ΔH^o = 46.19 kJ mol^{-1} at 25°C, which is lower than that of methane steam reforming, ΔH^o = 165 kJ mol^{-1}. Even if ammonia is directly supplied to the anode, the temperature distribution in the anode will be reduced significantly as compared to the case of methane. This will be beneficial for the direct use of ammonia fuel and the construction of simplified generation system. Therefore, much effort has been devoted to enhance the performance of direct ammonia–fuelled SOFCs employing oxide-ion [18-21] or proton [22-26] conducting electrolytes.

It was proven that the utilization of ammonia as a fuel in SOFCs follows the two–step process over anode; NH_3 is catalytically decomposed to H_2 and N_2 and then H_2 produced is electrochemically oxidized over anode [27–29]. Thus, the activity for the ammonia decomposition as well as the electrochemical hydrogen oxidation over anode can be considered as one of the key factors for direct ammonia-fuelled SOFCs. However, the superiority of ammonia to methane as a hydrogen carrier for the direct use in SOFCs has not been investigated sufficiently. Thus, it is indispensable to make clear the property of fuels, especially ammonia, and its influence on the cell performance. In this chapter, then, the cell performance was compared with feeding humidified H_2, NH_3, and CH_4 fuels directly to the conventional Ni–YSZ cermet anode at 500–800°C. The mechanism of ammonia utilization over Ni–YSZ anode was also investigated in detail from the aspect of kinetics study on ammonia decomposition rate to clarify the factors affecting to the cell performance.

1. 2. Experimental

Electrolyte–supported cells were used in electrochemical experiments. A commercial disk of 8 mol% Y_2O_3–ZrO_2 (YSZ, Tosho, 500 μm thickness and 24 mm diameter) was used as an electrolyte. The anode cermet was prepared by mechanical mixing of NiO (Wako Pure Chemical Industries) and YSZ (8 mol% Y_2O_3–ZrO_2, Tosoh) powders. The mixing ratio was controlled to be 50 vol.% Ni after reduction treatment at 1000°C. Two powders were ball–milled in ethanol for 24 h and then dried. The mixture obtained was calcined at 1200°C in air for 5 h. After calcination, the resulting powder was mixed with 10 wt.% carbon black as a pore former and subsequently ball–milled in ethanol for 24 h. The oxide of $(La_{0.8}Sr_{0.2})_{0.97}MnO_3$ (LSM) was selected as a cathode and prepared as follows; $La(CH_3CO_2)_3 \cdot 1.5H_2O$ (Alfa Aesar), $Sr(CH_3CO_2)_2 \cdot 0.5H_2O$ (Wako Pure Chemical Industries), and $Mn(CH_3CO_2)_2 \cdot 4H_2O$ (Wako Pure Chemical Industries) were dissolved with a stoichiometric ratio in an ultra-pure water. The mixture was heated on hot plate until combustion occurs. The resultant ash was calcined at 900°C in air for 5 h and then ball-milled overnight [29, 30]. The obtained NiO–YSZ and LSM powders were mixed with polyethyleneglycol (PEG, Wako Pure Chemical Industries) to form slurry.

The cell was fabricated by screen printing the anode slurry of NiO–YSZ on one side of YSZ electrolyte and then fired at 1400°C in air for 5 h. The cathode slurry of LSM was screen–printed on the other side of electrolyte followed by the firing at 1150°C in air for 5 h. The electrode geometry was controlled to be 6 mm in diameter and 60 μm and 40 μm in thickness for anode and cathode, respectively. A platinum wire was fixed by the platinum paste (Metalor Technologies (Japan) Corp.) around the edge of YSZ disk to serve as a reference electrode and fired at 900°C in air for 2 h. Finally, the cell was placed between two alumina tubes and sealed by Pyrex glass rings to prevent gas leakage.

Before the performance test, the anode was reduced at 1000°C for 1 h in H_2–Ar

atmosphere. Humidified gases of H_2–H_2O–Ar, NH_3–H_2O–Ar, or CH_4–H_2O–Ar were supplied to the anode. The composition of three fuels were controlled to give almost the same theoretical partial pressure of oxygen, $P(O_2)$, at each temperature. The $P(O_2)$ for hydrogen and methane fuels was calculated from the thermodynamic calculation (MALT v1.0, Kagaku,Gijutsu-Sha). In the case of NH_3 fuel, the $P(O_2)$ was calculated assuming that ammonia completely decomposed to H_2 and N_2 at each temperature.

The rate equation for ammonia decomposition reaction was evaluated with supplying NH_3-containing anode gases to Ni–YSZ anode. The oxygen partial pressure at the anode was calculated from OCV using Nernst equation,

$$E_{OCV} = \frac{RT}{nF} \ln\left(\frac{P(O_2)_c}{P(O_2)_a}\right) \quad (1\text{–}1)$$

where E_{OCV} is the cell potential under the open circuit state, R is the gas constant, T is the temperature, n is the number of transferred electron, F is the Faraday constant, and $P(O_2)_c$ and $P(O_2)_a$ are the oxygen partial pressure at the cathode and anode, respectively. The partial pressure of hydrogen, $P(H_2)$, produced from ammonia decomposition reaction was determined by using Eq. (1–2).

$$P(H_2) = \sqrt{\left(\frac{P(H_2O)^2}{K_1 \times P(O_2)_a}\right)} \quad (1\text{–}2)$$

where $P(H_2O)$ is the partial pressure of steam in the anode gas mixture, and K_1 is the equilibrium constant for hydrogen oxidation reaction. The decomposition percent of ammonia was calculated according to the following Eq. (1–3);

$$\mathrm{NH_3\ decomposition\ /\ \%} = \left(\frac{n\,(\mathrm{NH_3\ inlet}) - n\,(\mathrm{NH_3\ unreacted})}{n\,(\mathrm{NH_3\ inlet})}\right) \times 100 \qquad (1\text{–}3)$$

where $n(\mathrm{NH_3}$ inlet) and $n(\mathrm{NH_3}$ unreacted) are the number of moles of ammonia in the inlet gas and unreacted ammonia in the outlet gas, respectively. The hydrogen concentration produced from ammonia decomposition reaction, $C(\mathrm{H_2}$ produced) / %, can be calculated from Eq. (1–4).

$$C(\mathrm{H_2\ produced})\ /\ \% = \left(\frac{n(\mathrm{H_2\ produced})}{n_t}\right) \times 100 \qquad (1\text{–}4)$$

where $n(\mathrm{H_2}$ produced) is the number of moles of hydrogen produced from ammonia decomposition reaction, and n_t is the total number of moles of outlet gases. In all experiments, 100% O_2 was supplied to the cathode with a total flow rate of 100 ml min^{-1}. Electrochemical measurements were conducted by the CellTest system (Solartron Analytical, potentiostat/galvanostat 1470E and frequency response analyzer 1455A).

1. 3. Results and discussion

1.3. 1. Cell performance with three different fuels

The fuel gas mixtures supplied to the anode were 45% H_2–20% H_2O–35% Ar, 30% NH_3–20% H_2O–50% Ar, and 9% CH_4–20% H_2O–71% Ar (flow rate; 100ml min^{-1}). The theoretical partial pressure of oxygen and corresponding OCV at 500–800^oC for each fuel are summarized in Tables 1.1 and 1.2, respectively; in this study, the gas composition was controlled to be almost the same $P(O_2)$ as well as theoretical OCV.

Figure 1. 1 shows current-voltage (*I*-*V*) characteristics of the single cell operated at different temperatures with feeding humidified fuels. In the case of wet H_2 fuel, the

experimental OCV was identical to the theoretical one at each temperature. Although at 800^{o}C the OCV was almost the same to the theoretical value for both wet NH_3 and CH_4 fuels, slight deviation was observed at 700^{o}C. At 500–600^{o}C, the experimental OCVs in wet NH_3 and CH_4 fuels were significantly lower than the theoretical value. The order of OCV at 500–700^{o}C was dependent on fuels as follows, H_2 > NH_3 > CH_4. This order reflects the difference in hydrogen concentration in the vicinity of anode. The cell performance was changed in accordance with this trend.

Electrochemical impedance spectroscopy was carried out under the open circuit condition for the anode. The spectra in various fuels at 700^{o}C are shown in Fig. 1. 2(a) and the anodic polarization resistance at each temperature is summarized in Fig. 1. 2(b). The polarization resistance was almost the same regardless of fuels at 800^{o}C. Below 700^{o}C, however, the polarization resistance in wet NH_3 and CH_4 started to deviate from that in wet H_2, which become prominent in wet CH_4. A series of results suggests that the hydrogen concentration in the vicinity of anode determines the cell performance. In this respect, thus, NH_3 is a preferable fuel rather than CH_4 for the direct use in SOFCs because ammonia decomposes readily over wide temperature range. Hereafter, the physicochemical properties of NH_3 over Ni–YSZ cermet anode and its influence on the cell performance were studied.

1.3. 2. Effect of total flow rate on cell performance and NH_3 decomposition rate

To investigate the effect of total flow rate of fuels on the cell performance and ammonia decomposition, two gaseous mixtures of 20% NH_3–5% H_2O–75% Ar and 30% H_2–5% H_2O–65% Ar were supplied to the Ni–YSZ anode with varying the total flow rate from 100 to 300 ml min^{-1}. Figure 1. 3 show (a) *I-V*, current–power (*I-P)* curves for a single cell and (b) impedance spectra of Ni–YSZ in wet NH_3 fuel at 600^{o}C. The OCV decreased with an increase in total flow rate. Furthermore, the cell performance was deteriorated due to an

increment in polarization resistance. Figure 1. 4 shows the ammonia decomposition as a function of residence time. The definition of residence time is as follow;

$$\text{Residence time} = \frac{W}{F} \qquad (1\text{–}5)$$

where W is the anode weight and F is the total flow rate of inlet gas. The ammonia decomposition decreased with decreasing the residence time. This can be explained by the difference in the contact time between anode and NH_3. On the other hand, in the case of wet H_2 fuel, OCV and cell performance were almost independent of gas flow rate (see Fig. 1. 5). These results also support that the cell performance is determined by the hydrogen concentration in the vicinity of anode, which depends on the ammonia decomposition over Ni–YSZ anode. Therefore, we can conclude that NH_3 is mainly utilized via the two-step process over anode; NH_3 is catalytically decomposed to H_2 and N_2 and then H_2 produced is electrochemically oxidized over anode.

1. 3. 3. Effect of H_2, N_2 and steam on NH_3 decomposition over Ni–YSZ anode

Below 800°C the gas in the vicinity of anode consists of N_2, H_2, H_2O, Ar, and unreacted NH_3 when the NH_3-containing fuel is directly supplied to the anode. Thus, these gases may affect the ammonia decomposition rate over Ni–YSZ anode, which is an important factor to determine the cell performance.

At first, the nitrogen concentration dependence on ammonia decomposition was studied in 40% NH_3–0.5% H_2O–x% N_2–(59.5–x)% Ar atmosphere (x = 10-25, flow rate; 100 ml min^{-1}) at 600°C under the open circuit condition (see Fig. 1. 6). It is apparent that the ammonia decomposition was independent of N_2 concentration. Next, the influences of NH_3 and H_2 concentrations were evaluated at 600°C in two different atmospheres, n% NH_3–0.5% H_2O–(99.5–n)% Ar and n% NH_3–0.5% H_2O–10% H_2–(89.5–n)% Ar (n = 20-80, flow rate; 100 ml min^{-1}). Figure 1. 7 shows the concentration of H_2 produced from NH_3 decomposition

reaction, $C(H_2$ produced) / %, over Ni–YSZ anode as a function of NH_3 concentration in the absence and presence of 10% of H_2. An increase in $C(H_2$ produced) was confirmed with an increment in NH_3 concentration under both atmospheres. Note that $C(H_2$ produced) decreased by *ca*. 50% in the presence of 10% H_2 in the feed gas as compared to the case without hydrogen addition. This indicates that hydrogen has a negative influence on ammonia decomposition rate. The effect of H_2 concentration on ammonia decomposition rate was studied at 600°C in 40% NH_3–0.5% H_2O–*y*% H_2–(59.5–*y*)% Ar (*y* = 10-25, flow rate; 100 ml min^{-1}), as can be seen in Fig. 1. 8. The ammonia decomposition decreased significantly with increasing H_2 concentration. Since the rate of ammonia decomposition reaction was dependent on NH_3 and H_2 concentrations, the rate equation for ammonia decomposition reaction can be represented as follow;

$$r_{NH_3} = k\, P(\mathrm{NH_3})^{\alpha}\, P(\mathrm{H_2})^{\beta} \qquad (1\text{–}6)$$

where r_{NH3} is the rate of ammonia decomposition reaction, $P(NH_3)$ and $P(H_2)$ are the partial pressure of ammonia and hydrogen, respectively, k, α, and β are constants. The values of α and β at 600°C were 0.47 and –2.02, respectively, which were calculated from the slope in Fig. 1. 9. The positive sign of α suggests that the rate of ammonia decomposition reaction is accelerated by increasing NH_3 concentration, while the negative sign of β indicates that there was a strong inhibition effect of hydrogen (H_2 poisoning) on the catalytic decomposition of NH_3. On the other hand, at 850°C ammonia decomposition was independent of the hydrogen concentration (not shown). Thus, the rate equation is first order with respect to partial pressure of ammonia as in the following equation,

$$r_{NH_3} = k\, P(\mathrm{NH_3})^{\alpha} \qquad (1\text{–}7)$$

In this case, α was estimated to be 1.0. This means that the hydrogen inhibition effect can be negligible at 850^{o}C because the hydrogen desorbs readily from active sites.

Likewise it is important to study the effect of steam concentration on ammonia decomposition rate, because steam is formed via the electrochemical reaction at the anode when the oxide ion conducting electrolyte is used. The gaseous mixture of 20% NH_3–*m*% H_2O–(80–*m*)% Ar (*m* = 0.5-20, flow rate; 100 ml min^{-1}) was supplied to the anode at 600^{o}C. Figure 1. 10 shows the NH_3 decomposition as a function of steam concentration. There was no appreciable change in ammonia decomposition in the steam concentration range of 0.5-20%. In our previous study, the effect of steam concentration on ammonia decomposition over Ni–YSZ catalyst using a fixed bed reactor was studied [31]; reactant gas: 42.9% NH_3–*x*% H_2O– (57.1–*x*)% Ar (*x* = 0-8), gas space velocity: 14000 l kg^{-1} h^{-1}, and reaction temperature: 600^{o}C. A gradual decrease in ammonia decomposition observed with an increase in steam concentration. The discrepancy between previous and current results will be caused by the difference in the experimental condition, especially the gas space velocity and apparatus setup. In this study, the gas space velocity was 2.4×10^{6} l kg^{-1} h^{-1} because of the cell configuration, which was 170 times higher than that in previous study. Thus, the influence of steam might be reduced due to the low residence time in this study.

Throughout this study, it was clarified that the performance of direct NH_3–SOFCs significantly depends on the catalytic activity of anode material for ammonia decomposition. For the design of excellent anode, the high tolerance to hydrogen poisoning will be a crucial factor.

1. 4. Conclusion

In this chapter the performance of Ni–YSZ anode for three different fuels (H_2, NH_3 and CH_4) was compared under almost the same $P(O_2)$. The order of cell performance was dependent on fuel species as follow, $H_2 > NH_3 > CH_4$ at 500-700^oC. This behavior was caused by the difference in the catalytic activity of Ni–YSZ for ammonia decomposition and methane steam reforming. Thus, we concluded that the ammonia is a preferable fuel for the direct use in SOFCs because of the ease in catalytic decomposition over wide temperature range. The influential factors for the ammonia decomposition over Ni–YSZ anode were also studied in detail.

Ammonia decomposition was affected by NH_3, and H_2 concentrations, and total flow rate, while it was independent of steam and N_2 concentrations. It was clarified that hydrogen serves as a poisoning species in the ammonia decomposition process. Thus, the development of anode with high catalytic activity for ammonia decomposition as well as the high tolerance to hydrogen poisoning will be required for the performance enhancement of direct NH_3–SOFCs.

References

[1] A. Bertei, J. Mertens, C. Nicolella, *Electrochim. Acta*, **146**, 151–163 (2014).

[2] S.C. Singhal, *Solid State Ionics*, **135**, 305–313 (2000).

[3] P. Aguiar, C.S. Adjiman, N.P. Brandon, *J. Power Sources*, **138**, 120–136 (2004).

[4] C. Zamfirescu, I. Dincer, *Fuel Process. Technol.*, **90**, 729–737 (2009).

[5] A.S. Chellappa, C.M. Fischer, W.J. Thomson, *Appl. Catal. A–Gen.*, **227**, 231–240 (2002).

[6] J. L. Brett, A. Atkinson, D. Cumming, E. R. Cabrera, R. Rudkin, N. P. Brandon, *Chem. Eng. Sci.*, **60**, 5649–5662 (2005).

[7] T. Caillot, G. Gauthier, P. Delichère, C. Cayron, F.J. Cadete S. Aires, *J. Catal.*, **290**, 158–164 (2012).

[8] Y.H. Huang, R.I. Dass, Z.L. Xing, J.B. Goodenough, *Science*, **312**, 254–257 (2006).

[9] B. C. Enger, R. Lødeng, A. Holmen, *Int. J. Hydrogen Energy*, **37**, 10418–10424 (2012).

[10] W. Wang, R. Ran, C. Su, Y. Guo, D. Farrusseng, Z. P. Shao, *J. Power Sources*, **240**, 232–240 (2013).

[11] B. Hua, M. Li, B. Chi, L. Jian, *J. Mater. Chem. A*, **2**, 1150–1158 (2014).

[12] E. W. Park, H. Moon, M. Park, S. H. Hyun, *Int. J. Hydrogen Energy*, **34**, 5537–5545 (2009).

[13] L. Zhang, Y. Cong, W. Yang, L. Lin, *Chinese J Catal.*, **28**, 749–751 (2007).

[14] C. Zamfirescu, I. Dincer, *J. Power Sources*, **185**, 459–465 (2008).

[15] G. Cinti, U. Desideri, D. Penchini,G. Discepoli, *Fuel Cells*, **14**, 221–230 (2014).

[16] C. H. Christensen, T. Johannessen, R. Z. Sørensen, J. K. Nørskov, *Catal. Today*, **111**, 140–144 (2006).

[17] F. Ishak, I. Dincer, C. Zamfirescu, *J. Power Sources*, **202**, 157–165 (2012).

[18] A. Wojcik, H. Middleton, I. Damopoulos, J. V. herle, *J. Power Sources*, **118**, 342–348 (2003).

[19] G.G.M. Fournier, I.W. Cumming, K. Hellgardt, *J. Power Sources*, **162**, 198–206 (2006).

[20] M. Qianli, M. Jianjun, S. Zhou, Y. Ruiqiang, G. Jianfeng, G. Meng, *J. Power Sources*, **164**, 86–89 (2007).

[21] L. Liu, K. Sun , X. Wu, X. Li, M. Zhang, N. Zhang, X. Zhou, *int. J. Hydrogen Energy*, **37**, 10857–10865 (2012).

[22] L. Pelletier, A. McFarlan, N. Maffei, *J. Power Sources*, **145**, 262–265 (2005).

[23] N. Maffei, L. Pelletier, J.P. Charland, A. M. Farlan, *J. Power Sources*, **140**, 264–267 (2005).

[24] N. Maffei, L. Pelletier, J.P. Charland , A. M. Farlan, *J. Power Sources*, **162**, 165–167 (2006).

[25] N. Maffei, L. Pelletier, A. M. Farlan, *J. Power Sources*, **175**, 221–225 (2008).

[26] Q. Ma, R. Peng, Y. Lin, J. Gao, G. Meng, *J. Power Sources*, **161**, 95–98 (2006).

[27] A. Fuerte, R. X. Valenzuela, M. J. Escudero, L. Daza, *J. Power Sources*, **192,** 170–174 (2009).

[28] J. Yang, T. Akagi, T. Okanishi, H. Muroyama, T. Matsui, K. Eguchi, *Fuel Cells,* **15**, 390–397 (2015).

[29] A. F. S. Molouk, J. Yang, T. Okanishi, H. Muroyama, T. Matsui, K. Eguchi, *ECS Trans*, **68**, 2751–2762 (2015).

[30] T. Matsui R. Kishida, J. Kim, H., K. Eguchi, *J. Electrochem. Soc*., **157**, B776–B781 (2010).

[31] J. Yang, A. F. S. Molouk, T. Okanishi, H. Muroyama, T. Matsui, K. Eguchi, *ACS Appl. Mater. Interfaces,* **7**, 7406–7412 (2015).

Table 1. 1

Theoretical partial pressure of oxygen for H_2, NH_3 and CH_4 fuels at 500–800^{o}C.

	Partial pressure of oxygen (atm)			
	500^{o}C	600^{o}C	700^{o}C	800^{o}C
45% H_2–20% H_2O–35% Ar	3.9×10^{-29}	2.5×10^{-25}	2.8×10^{-22}	8.4×10^{-20}
30% NH_3–20% H_2O–50% Ar (2–step reaction)	3.9×10^{-29}	2.5×10^{-25}	2.8×10^{-22}	8.4×10^{-20}
9% CH_4–20% H_2O–71% Ar	9.7×10^{-29}	1.6×10^{-25}	1.3×10^{-22}	4.6×10^{-20}

Table 2. 1

Theoretical OCVs for H_2, NH_3 and CH_4 fuels at 500–800^{o}C.

	Open circuit voltage (V)*			
	500^{o}C	600^{o}C	700^{o}C	800^{o}C
45% H_2–20% H_2O–35% Ar	1.089	1.065	1.040	1.015
30% NH_3–20% H_2O–50% Ar (2–step reaction)	1.089	1.065	1.040	1.015
9% CH_4–20% H_2O–71% Ar	1.074	1.073	1.056	1.029

* Cathode gas: 100% O_2 (flow rate; 100ml min^{-1}).

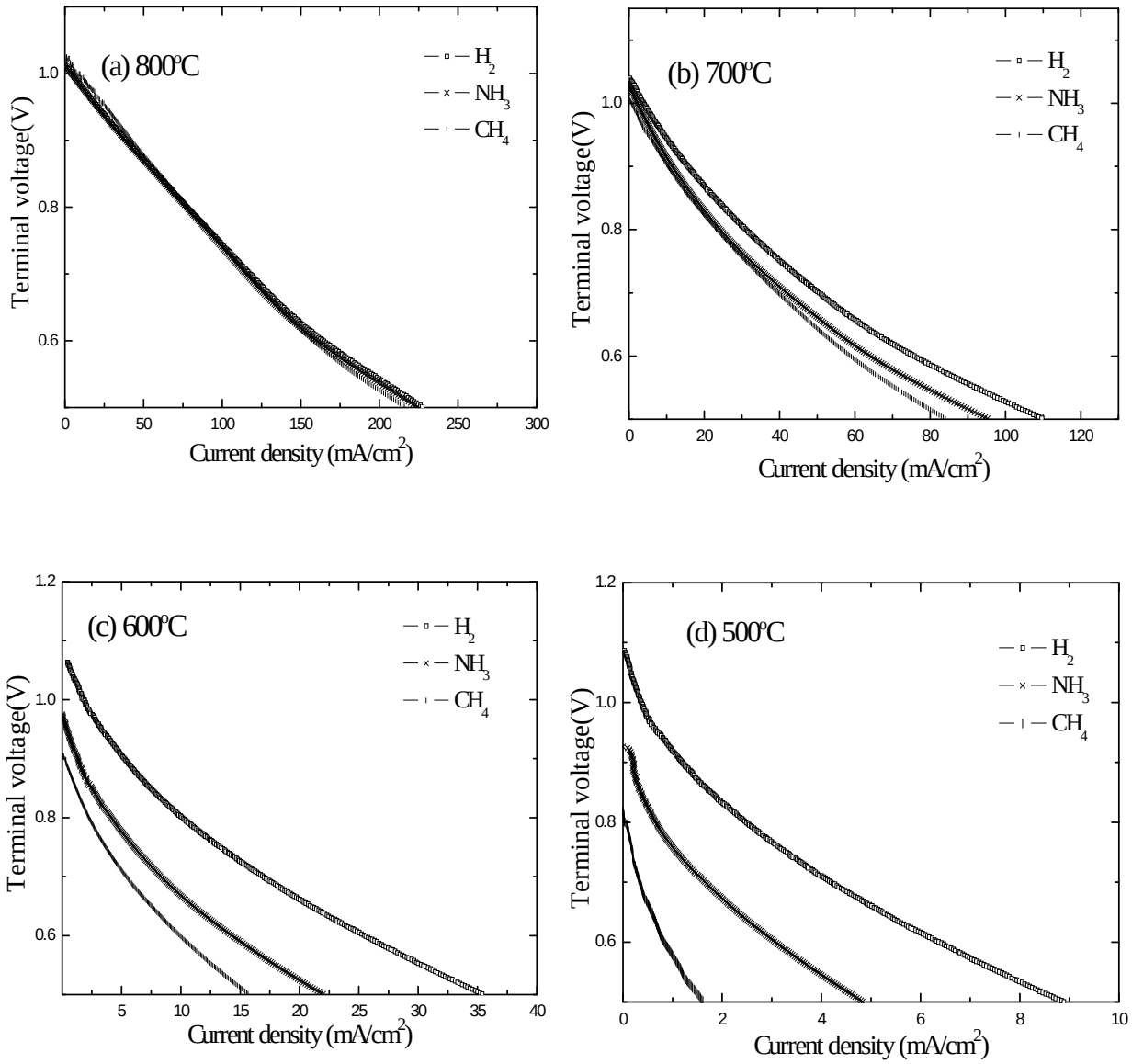

Figure 1. 1. *I-V* curves for the cell of Ni–YSZ|YSZ|LSM. Anode gas; 45% H_2–20% H_2O–35% Ar, 30% NH_3–20% H_2O-50% Ar, and 9% CH_4–20% H_2O–71% Ar (flow rate; 100 ml min^{-1}) at (a) 800°C, (b) 700°C, (c) 600°C and (d) 500°C. Cathode gas; O_2 (100 ml min^{-1}).

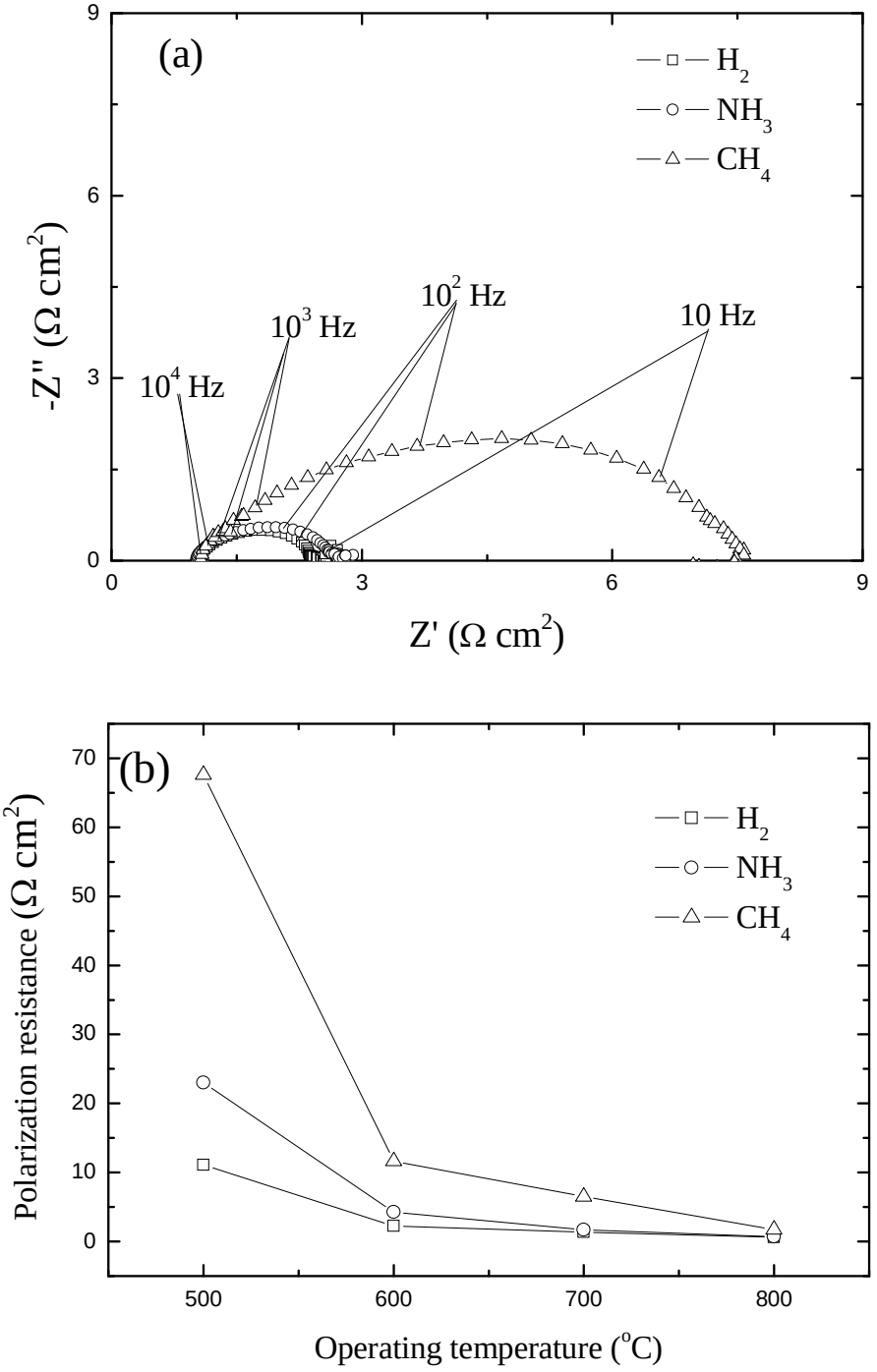

Figure 1. 2. (a) Impedance spectra for Ni–YSZ anode at 700°C, and (b) anodic polarization resistance of Ni–YSZ in three different fuels at each temperature. Anode gas; 45% H_2–20% H_2O–35% Ar , 30% NH_3–20% H_2O–50% Ar, and 9% CH_4–20% H_2O–71% Ar (flow rate; 100 ml min^{-1}). Cathode gas; O_2 (100 ml min^{-1}).

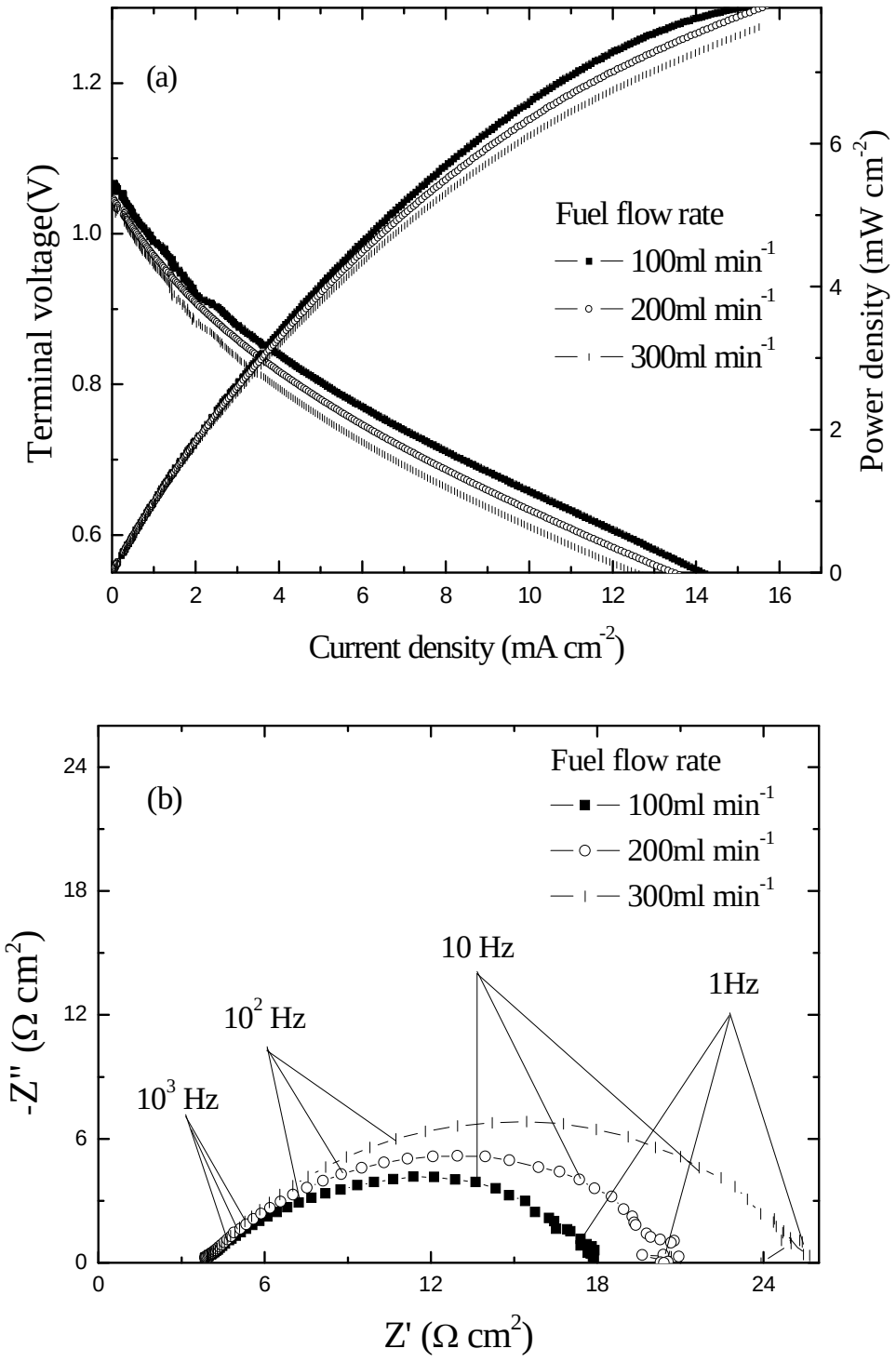

Figure 1. 3. (a) *I-V, I-P* curves for a single cell and (b) impedance spectra of Ni–YSZ anode in wet NH_3 at 600°C. Anode gas; 20% NH_3–5% H_2O–75% Ar (flow rate; 100-300 ml min^{-1}), and cathode gas; O_2 (100 ml min^{-1}).

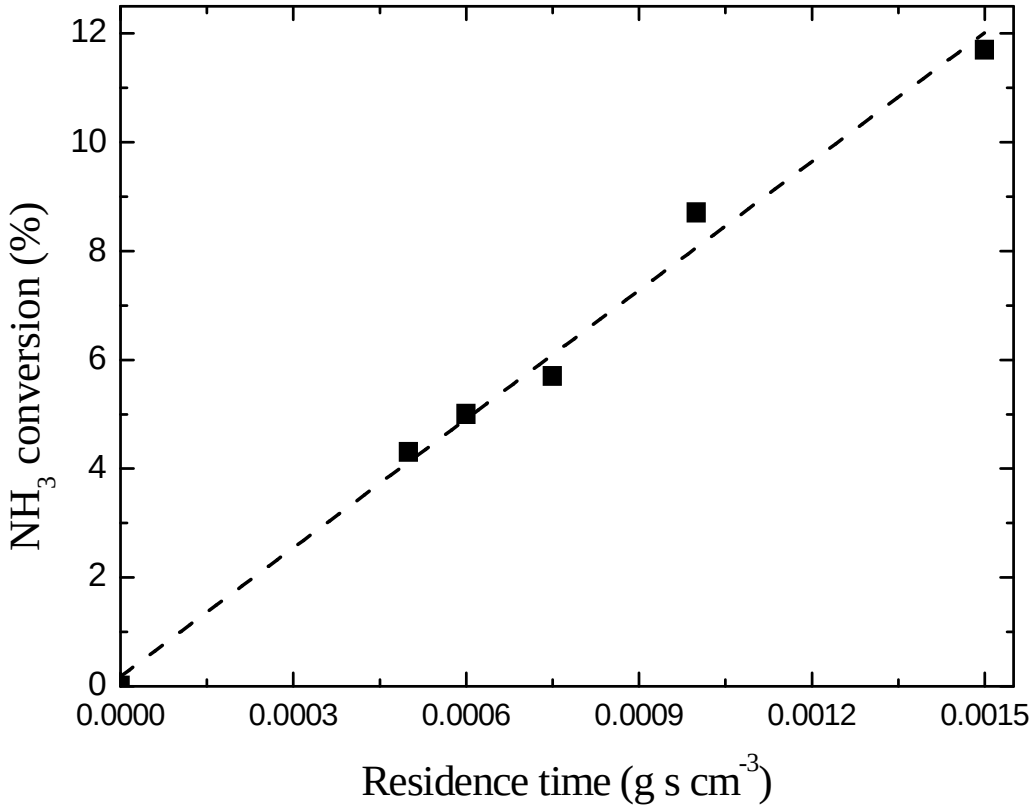

Figure 1. 4. NH_3 decomposition as a function of residence time at 600^{o}C.

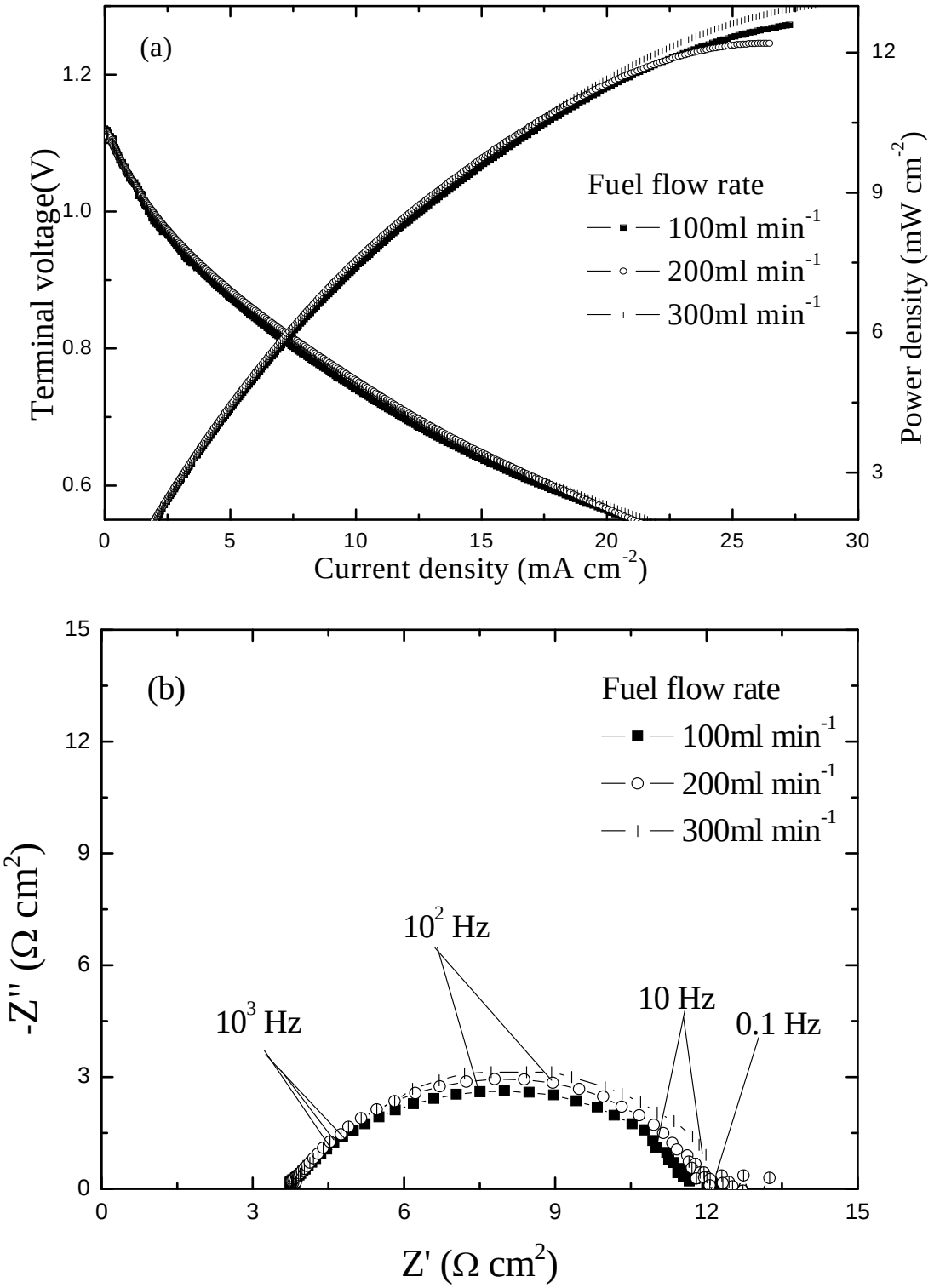

Figure 1. 5. (a) *I-V*, *I-P* curves for single cell and (b) impedance spectra for Ni–YSZ anode in wet H_2 at 600^{o}C. Anode gas; 30% H_2–5% H_2O–65% Ar (flow rate; 100-300 ml min^{-1}), and cathode gas; O_2 (100 ml min^{-1}).

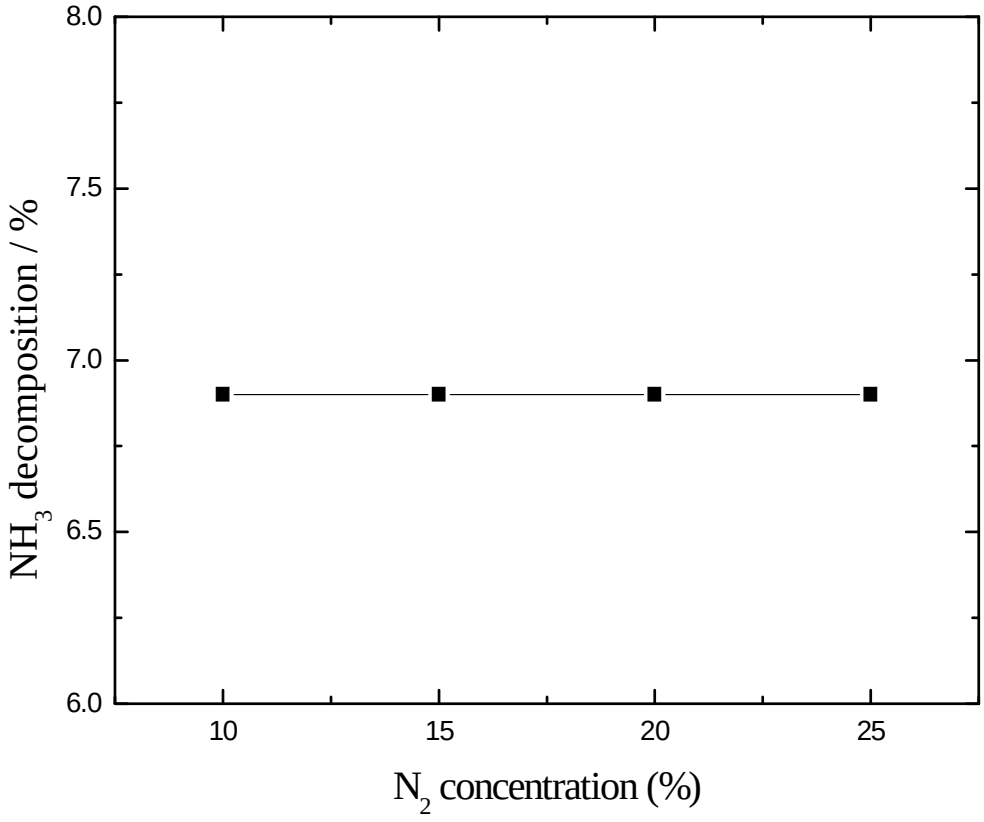

Figure 1. 6. NH_3 decomposition as a function of N_2 concentration at 600°C. Anode gas; 40% NH_3–0.5% H_2O–*x*% N_2–(59.5–*x*)% Ar (*x* = 10-25, flow rate: 100 ml min^{-1}). Cathode gas; O_2 (100 ml min^{-1}).

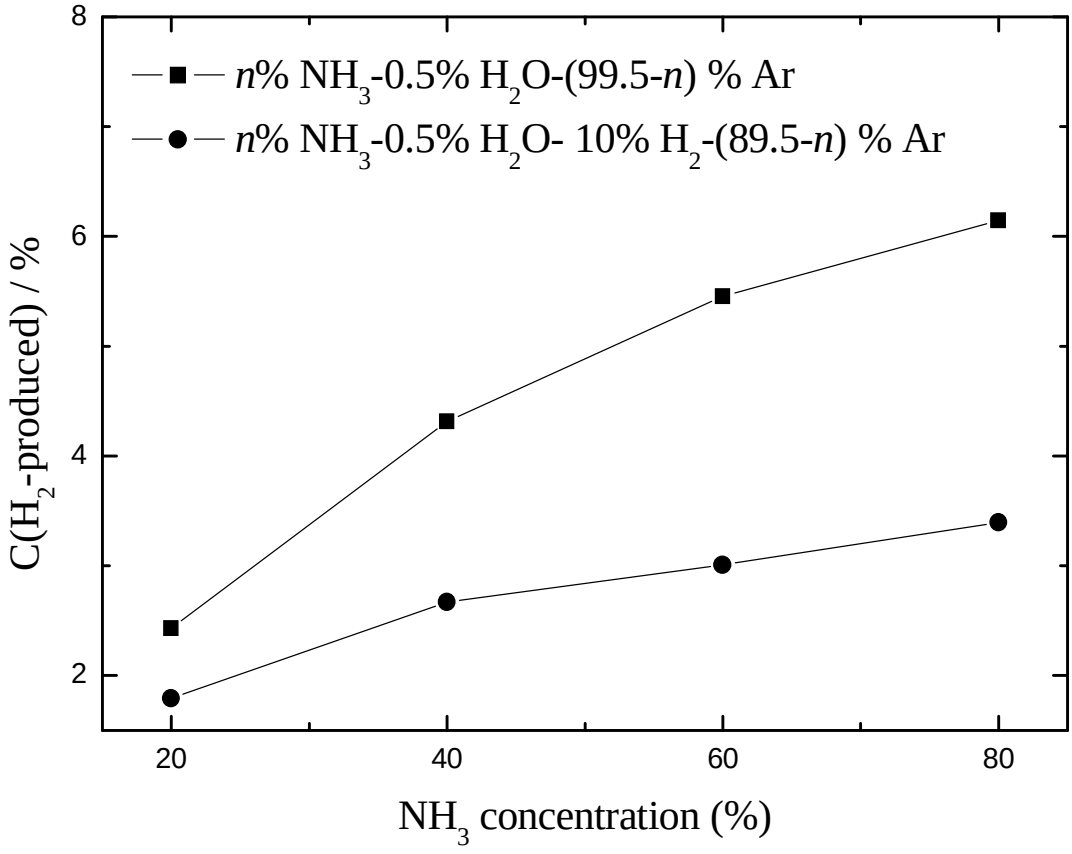

Figure 1. 7. Hydrogen concentration produced from NH_3 decomposition over Ni–YSZ anode at 600^{o}C as a function of NH_3 concentration in the presence and absence of 10% H_2. Anode gas; *n*% NH_3–0.5% H_2O–(99.5–*n*)% Ar, and *n*% NH_3–0.5% H_2O–10% H_2–(89.5–*n*)% Ar (*n* = 20-80, flow rate; 100 ml min^{-1}). Cathode gas; O_2 (100 ml min^{-1}).

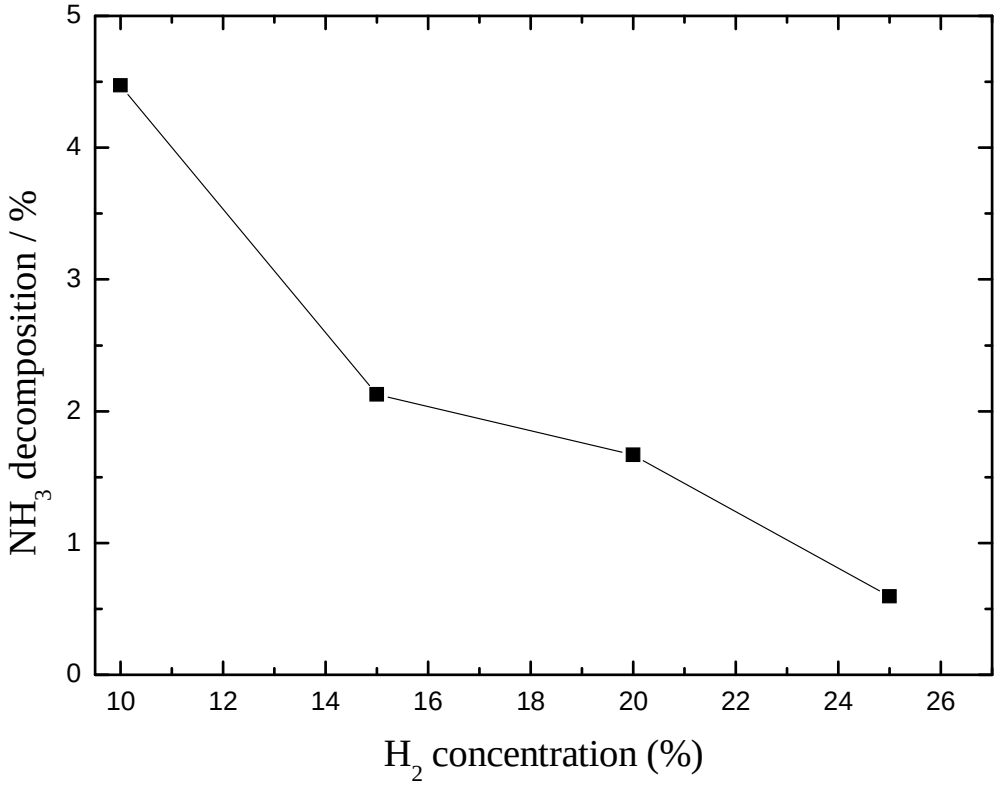

Figure 1. 8. NH_3 decomposition as a function of H_2 concentration at 600^{o}C. Anode gas; 40% NH_3–0.5% H_2O– *y*% H_2–(59.5–*y*)% Ar (*y* = 10-25, flow rate; 100 ml min^{-1}). Cathode gas; O_2 (100 ml min^{-1}).

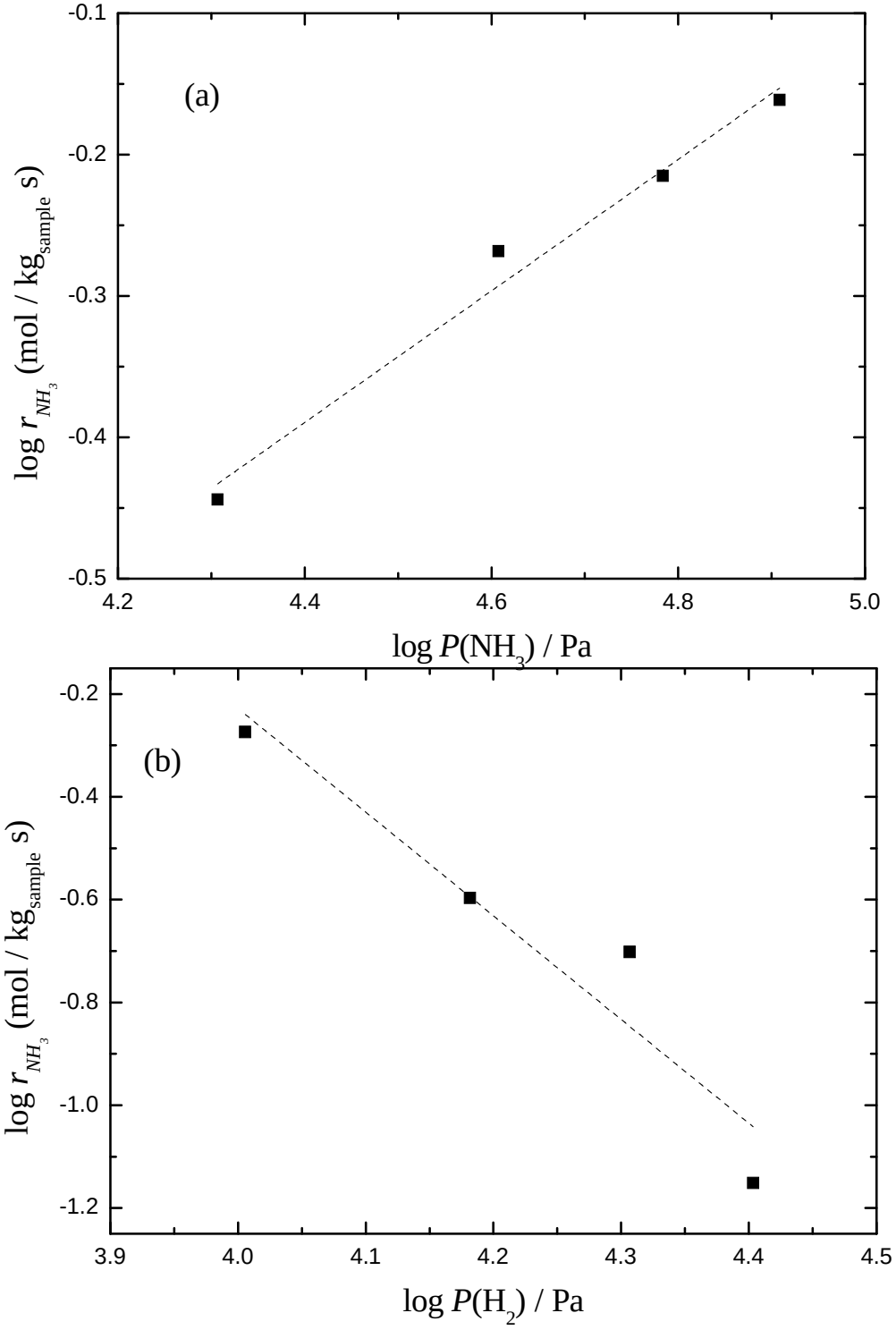

Figure 1. 9. (a) NH_3 and (b) H_2 partial pressure dependence of NH_3 decomposition over Ni-YSZ anode at 600°C.

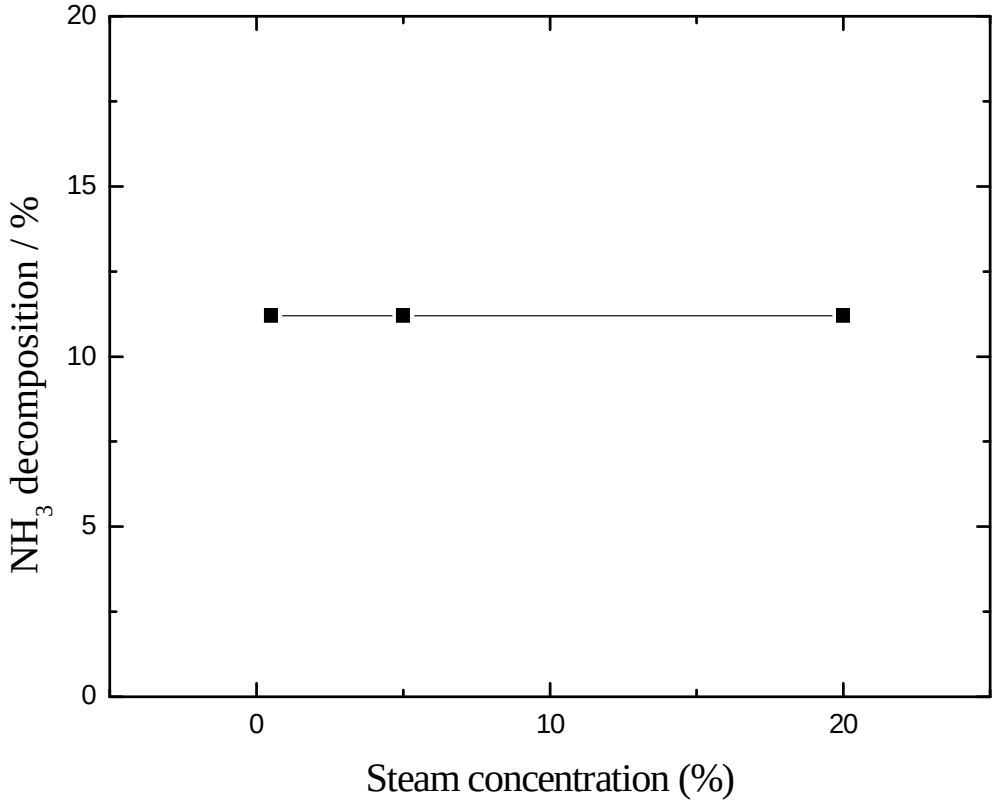

Figure 1. 10. NH_3 decomposition as a function of steam concentration at 600°C. Anode gas; 20% NH_3–*m*% H_2O–(80–*m*)% Ar (*m* = 0.5-20, flow rate was 100 ml min^{-1}). Cathode gas; O_2 (100 ml min^{-1}).

Chapter 2

Comparative Study on Ammonia Oxidation Over Ni-based Cermet Anodes for Solid Oxide Fuel Cells

2. 1. Introduction

Increasing demand in electrical energy inevitably gives rise to the consumption of a large amount of fossil fuels and the emission of greenhouse gases to the environment. Solid oxide fuel cells (SOFCs) are electrochemical generators with high efficiency [1–4]. The performance of SOFC is dependent on the kind of fuel, anode materials, and anodic reactions. High performance can be achieved with hydrogen and hydrocarbon fuels. Hydrogen has been considered as a future clean fuel with the least emission of greenhouse gases [5, 6]. However, the storage and transportation of hydrogen are major obstacles for the large-scale application due to its low volumetric density and boiling point [7, 8].

Recently, ammonia has attracted a great attention as a fuel because of many advantages; carbon free fuel with higher energy density, ease in liquefaction (boiling point: –33.4^{o}C at atmospheric pressure), and narrower flammable range than hydrogen, etc [9-13]. The worldwide distribution system is well established as widely produced commodity chemical and fertilizer. Based on these entire characteristics, ammonia, especially synthesized from the renewable energy, is considered as a future promising fuel and/or hydrogen carrier. Methane or natural gas has been considered as a suitable fuel for SOFCs because of its cleanliness among the fossil fuels and a higher energy density than hydrogen. However, its consumption inevitably accompanies CO_2 emission. The systematic study in the previous chapter indicated that the SOFC consisting of Ni–YSZ|YSZ|(La,Sr)$MnO_{3+\delta}$ demonstrated a higher performance with ammonia fuel than that with methane at the same temperature and anodic oxygen potential.

The preferable performance of direct NH_3–fueled SOFC resulted from a higher reactivity of NH_3 for decomposition than CH_4 reforming on Ni–YSZ [14].

The Ni–YSZ cermet is the most popular anode material, which achieves most of the requirements for efficient SOFCs [15-17]. However, the activity of Ni–YSZ anode for the electrochemical oxidation of fuels such as hydrocarbon and ammonia is often insufficient [18, 19]. On the other hand, gadolinia–doped ceria (GDC) has several advantages to YSZ as an oxide component for the cermet anode. GDC is a mixed ionic–electronic conductor under reducing atmospheres and its ionic conductivity is higher than that of YSZ [19]. Ceria has been known not only as a mixed conductor but also a catalyst material for oxidation–reduction reactions. Ceria also serves as a support for the Ni catalyst and prevents from sintering to provide a large and active triple–phase boundary (TPB) [20-22].

In this Chapter a comparative study on Ni–YSZ and Ni–GDC cermet anodes for SOFCs using H_2 and NH_3 fuels was conducted. We focused on the evaluation of the catalytic activity of Ni–YSZ and Ni–GDC for NH_3 decomposition and the polarization resistance of each anode. The effect of preparation method of NiO−GDC on NH_3 decomposition reaction was also studied for the development of active anode for direct NH_3–fueled SOFCs.

2. 2. Experimental

Electrolyte supported cells were used for the performance evaluation. Two different Ni–based cermet anodes (Ni–YSZ and Ni–GDC) were prepared. The NiO–YSZ anode powder was prepared by the physical mixing route as described in the previous chapter [14]. On the other hand, NiO–GDC anode powder was prepared by two methods; i) physical mixing and ii) glycine–nitrate combustion routes. The schematic diagram of the preparation routes is shown in Fig. 2. 1. The physical mixing was carried out by ball–milling of NiO (Wako Pure Chemical Industries), GDC ($Ce_{0.9}Gd_{0.1}O_{1.95}$, Shin–Etsu Chemical Co.), and 10 wt.% carbon

black as a pore former in ethanol for 24 h. The powder from the physical mixing is denoted as NiO–GDC (PM). For the glycine–nitrate combustion route, stoichiometric amounts of $Ce(NO_3)_3 \cdot 6H_2O$ (Wako Pure Chemical Industries), $Gd(NO_3)_3 \cdot 6H_2O$ (Wako Pure Chemical Industries), and $Ni(NO_3)_3 \cdot 6H_2O$ (Wako Pure Chemical Industries) were dissolved in water with stirring at room temperature. Glycine (Wako Pure Chemical Industries) was then added to the solution until the molar ratio of total metal ions/glycine reached to 1/2. After complete drying, the self–ignition takes place at *ca*. 350°C. The obtained ash was calcined at 850°C in air for 5 h. The resultant powder was mixed with 10 wt.% carbon black as a pore former and ball–milled in ethanol for 24 h. The powder thus prepared is abbreviated as NiO–GDC (GN). The Ni metal content in the anode was 60 wt.% after reduction treatment at 1000°C for every Ni–oxide cermet. The perovskite type oxide of $(La_{0.8}Sr_{0.2})_{0.97}MnO_3$ (LSM) was selected as a cathode and prepared as was reported in detail in the first chapter [23]. The obtained anode and LSM powders were mixed with polyethyleneglycol (PEG, Wako Pure Chemical Industries) to form slurry.

Cells were fabricated by screen printing the anode slurry on the flat face of YSZ disk electrolyte (8 mol% yttria-stabilized zirconia electrolyte, Tosoh, 500 μm in thickness and 24 mm in diameter) and firing at 1400°C in air for 5 h. Then, the cathode was printed and fired at 1150°C in air for 5 h. The electrode active area was 0.28 cm^2 and the thicknesses were 60 μm and 40 μm for anode and cathode, respectively. A platinum reference electrode was fixed by the platinum paste (Metalor Technologies (Japan) Corp.) around the edge of YSZ disk and fired at 900°C in air for 2 h. Finally, the cell was set between two alumina tubes and sealed by Pyrex glass rings to avoid the gas leakage.

The anode was reduced at 1000°C for 1 h prior to the electrochemical test. The anode gas mixtures were H_2–H_2O–Ar and NH_3–H_2O–Ar. The gas composition of NH_3–H_2O–Ar was controlled to achieve the same hydrogen concentration and flow rate of H_2–H_2O–Ar when the

complete decomposition of ammonia occurred. The cathode gas was 100% O_2 with a total flow rate of 100 ml min^{-1}. Electrochemical measurements were carried out by the CellTest system (Solartron Analytical, potentiostat/galvanostat 1470E and frequency response analyzer 1455A). After power generation test in hydrogen and ammonia fuels the anode microstructure was observed by a scanning electron microscopy (SEM, Nvision 40, Carl Zeiss-SIINT).

The catalytic activity for NH_3 decomposition over Ni–YSZ, Ni–GDC (PM), Ni–GDC (GN), YSZ, and GDC was studied using a fixed bed reactor. In these measurements, all samples were pre-calcined at 1400^oC for 5 h in air and then ball-milled in ethanol overnight. All powders were pressed into a pellet at 20 MPa and then pulverized to 12 mesh. The sample (0.6 g) was set in a fixed bed reactor and then reduced in H_2–Ar at 700^oC for 1 h. After that the temperature was reduced to 350^oC within 1 h in hydrogen, and then the reactor was purged with Ar (50 ml min^{-1} Ar for 30 min). The reactant gas of 66.7% NH_3–33.3% Ar (total flow rate; 60 ml min^{-1}) was supplied to each catalyst with a space velocity of 6000 l kg^{-1} h^{-1}. The outlet gas was passed through two traps containing 3.5M H_2SO_4 solution (Wako Pure Chemical Industries) to dissolve the unreacted NH_3 and then the flow rate of outlet gas containing H_2–N_2–Ar was measured by using a flow rate meter (VP3, Horiba STEC Co, Ltd.). The percentage of NH_3 decomposition can be calculated using Eq. (2–1).

$$\mathrm{NH_3\ decomposition\ /\ \%} = \left(\frac{F\ (\mathrm{NH_3\ inlet}) - F\ (\mathrm{NH_3\ unreacted})}{F\ (\mathrm{NH_3\ inlet})}\right) \times 100 \qquad (2\text{–}1)$$

where $F(NH_3$ inlet) and $F(NH_3$ unreacted) are the flow rate of ammonia in the inlet gas and unreacted ammonia in the outlet gas, respectively.

The surface basicity of YSZ and GDC was also measured by the temperature-programmed desorption of carbon dioxide (CO_2-TPD) using BELCAT-B (BEL

Japan, Inc.). The samples were preheated at 1400°C in air for 5 h and then ball-milled in ethanol overnight. The resultant powder was pressed into a pellet as in the catalyst test. Prior to the TPD experiment, 1 g of the sample was pre-treated in a helium atmosphere at 600°C for 1 h and then cooled to 50°C. Carbon dioxide was supplied with a flow rate of 30 ml min^{-1} for 1 h. After the sample was purged with helium at 50°C for 0.5 h, the sample was heated to 900°C at a heating rate of 10°C min^{-1} to monitor desorption of CO_2 using an on–line mass spectrometer (Pfeiffer Vacuum, OmniStare GSD320).

The specific surface area was determined by N_2 adsorption-desorption with the BET method at –196°C using BELSORP-miniII (BEL Japan, Inc.) The anode cermets were preheated at 1400°C for 5 h in air and then reduced at 1000°C in hydrogen. Prior to the BET experiment, 0.1 g of the sample was heated at 300°C in vaccum.

2. 3. Results and discussion

2. 3.1. Catalytic activity of Ni–based cermet for ammonia decomposition

In the previous study, it was suggested that the consumption of ammonia fuel proceeds via two step reactions over the anode in SOFCs [14, 24]. Ammonia decomposes over the Ni–based cermet to H_2 and N_2 by the thermal catalytic reaction followed by the electrochemical hydrogen oxidation. Therefore, the catalytic activity of Ni–based cermet for ammonia decomposition is one of the key factors to develop high performance anodes for direct NH_3–fueled SOFCs. In this chapter, the catalytic activities for ammonia decomposition over Ni–YSZ, Ni–GDC (PM), YSZ, and GDC were investigated using a fixed bed reactor. The Ni–GDC (PM) cermet demonstrated the highest activity for ammonia decomposition at 600°C among the catalysts tested (see Fig. 2. 2). Though Ni metal was indispensable for sufficient activity, GDC exhibited the catalytic activity to some extent compared with YSZ which was inactive for the ammonia decomposition. It is expected that activity of Ni metal

was further promoted by coexisting GDC because of the chemical interaction between Ni and GDC.

The catalytic decomposition of ammonia is composed of several reaction steps, *i.e.*, *i)* adsorption of ammonia onto catalyst sites, *ii)* cleavage of N-H bond of adsorbed ammonia, and *iii)* desorption of N_2 molecules. Generally, the last two steps control the rate of overall reaction [25-27]. The basic sites on the catalyst surface play an important role for promoting the rate determining step to achieve higher ammonia conversion. Therefore, CO_2–TPD experiment was conducted to YSZ and GDC. In the CO_2–TPD profiles in Fig. 2. 3, three peaks of CO_2 desorption were observed for GDC at *ca.* 120°C, 210°C, and 683°C. On the other hand, only two CO_2 desorption peaks were confirmed for YSZ at *ca.* 127°C, and 675°C. These results suggest that both oxides have weak and strong basic sites. The total amount of CO_2 desorbed from YSZ and GDC were 4.5 μmol g^{-1} and 42.7 μmol g^{-1}, respectively. Thus, it can be considered that the basic sites are abundant on the surface of the Ni–GDC (PM) cermet. Such a surface basicity is expected to be favorable for weakened adsorption of NH_3 and dissociation of N–H bond. On the other hand, it was proven that the hydrogen has a retardant effect for both Ni–YSZ and Ni–GDC anodes blew 800°C [14, 28], and the rate of ammonia decomposition reaction depends on ammonia and hydrogen partial pressure according to the following equation;

$$r_{NH_3} = k\, P(\mathrm{NH_3})^{\alpha}\, P(\mathrm{H_2})^{\beta} \qquad (2\text{–}2)$$

where r_{NH3} is the rate of ammonia decomposition reaction, $P(NH_3)$ and $P(H_2)$ are the partial pressure of ammonia and hydrogen, respectively, k, α, and β are constants. The values of β at 500°C for Ni–YSZ and Ni–GDC were –0.94 and –0.81, respectively [29]. This indicates that the retardant effect of hydrogen is less significant on the Ni–GDC (PM).

2. 3. 2. Electrochemical properties and fuel cell characteristics

Electrochemical impedance spectroscopy was carried out under the open circuit condition for the fuel cells employing the Ni–YSZ and Ni–GDC (PM) anodes with supplying 60% H_2–0.5% H_2O–39.5% Ar (flow rate; 100 ml min^{-1}) and 66.7% NH_3–0.8% H_2O–32.5% Ar (flow rate; 60 ml min^{-1}). The impedance spectra of anodes in wet H_2 and NH_3 at 600^{o}C and 1000^{o}C are shown in Fig. 2. 4. The anodic polarization resistance for Ni–GDC (PM) was smaller than that for Ni–YSZ both in wet H_2 and NH_3 fuels regardless of temperature. The polarization resistances in hydrogen and ammonia were almost the same for the respective anode at 1000^{o}C. On the other hand, the polarization resistance in ammonia was larger than in hydrogen for both anodes at 600^{o}C.

Figure 2. 5 summarises the temperature dependence of the anodic polarization resistance for two anodes in wet H_2 and NH_3 fuels at 600–1000^{o}C. The polarization resistance of Ni–YSZ in H_2 was larger than that of Ni–GDC (PM), especially at low operating temperatures. The polarization resistances of Ni–YSZ and Ni–GDC (PM) were almost the same at 900^{o}C and 1000^{o}C in both H_2 and NH_3 fuels. The difference in anodic polarization resistance for Ni–GDC (PM) and Ni–YSZ is larger in NH_3 fuel than in H_2 fuel at 600–800^{o}C. In the temperature range of 900–1000^{o}C, ammonia completely decomposed to produce H_2 with the similar concentration to that in H_2 fuel gas mixture in the present experimental condition. On the other hand, ammonia decomposed partially at 600–800^{o}C. The deviation of the polarization resistance between NH_3 and H_2 fuels is obviously small for Ni–GDC (PM) even in the low temperature range, whereas the polarization resistance of Ni–YSZ in NH_3 was very large. This tendency indicates that Ni–GDC (PM) is a more appropriate catalyst for NH_3–fueled SOFCs than Ni–YSZ.

It was found that the limiting current was easily observed for a dilute ammonia fuel. This means that hydrogen formed by the partial decomposition of ammonia can be consumed by

the electrochemical reaction. Therefore, the effect of ammonia concentration on the limiting current density was investigated to estimate the NH_3 conversion on the cermet. It was assumed that the concentration of hydrogen produced on the cermet corresponds to the limiting current of the cell. A dilute fuel gas mixture of *x*% NH_3–0.5% H_2O–(99.5–*x*)% Ar (*x* = 0.3-0.9, flow rate; 100 ml min^{-1}) was supplied to Ni–YSZ and Ni–GDC anodes at 700–1000°C to estimate the hydrogen concentration produced via ammonia decomposition from the limiting current. The hydrogen concentration was calculated by using following equations;

$$i_{\text{limiting}} = nF\left(\frac{dN}{dt}\right) \qquad (2\text{–}3)$$

where i_{limiting} is the limiting current (A), *dN/dt* is the rate of the electrochemical reaction (mol s^{-1}) which reflects the number of mole of hydrogen produced from ammonia decomposition, *n* is the number of electrons transferred for the hydrogen oxidation, and *F* is the Faraday's constant.

$$C(\text{H}_2\text{ produced})\ /\ \% = \left(\frac{dN/dt}{n_{\text{t}}}\right) \times 100 \qquad (2\text{–}4)$$

where $C(H_2$ produced) / % is the hydrogen concentration produced by ammonia decomposition reaction calculated from the limiting current, and n_t is the total number of moles of outlet gases (mol s^{-1}) which are unreacted NH_3, H_2, N_2, H_2O, and Ar .

Figure 2. 6 shows current-voltage *(I–V)* characteristics of single cells employing Ni–YSZ and Ni–GDC (PM) anodes at 700°C and 1000°C with feeding humidified NH_3. The *I–V* curves for both cells were almost identical at 1000°C, while at 700°C the cell with Ni–YSZ and Ni–GDC anodes reached to the limiting current of *ca.* 30 and 100 mA cm^{-2},

respectively. The hydrogen concentration produced from ammonia decomposition over anodes estimated from the limiting current is depicted in Fig. 2. 7(a) as a function of temperature. At 1000^{o}C the hydrogen concentration was almost the same for both anodes because ammonia was completely decomposed in this temperature range. Below 800^{o}C, the hydrogen concentration for the Ni–YSZ anode was significantly lowered as compared with that for the Ni–GDC (PM) anode. This tendency corresponds to the fact that Ni–GDC (PM) is more active for NH_3 decomposition in this temperature region. Thus, the high catalytic activity for ammonia decomposition of Ni–GDC (PM) is favorable. Furthermore, the hydrogen concentration in the vicinity of the anode was highly affected by the ammonia concentration in the fuel gas mixture and the anode material (see Fig. 2. 7(b)); the hydrogen concentration raised by increasing the ammonia concentration, and the conversion level was obviously higher for Ni–GDC (PM) anode.

2. 3. 3. Effect of preparation method for Ni–GDC

Further enhancement of anode performance for the direct NH_3–fueled SOFC was investigated by preparing a fine powder of Ni–GDC with large surface area [29]. It is expected that the activity for ammonia decomposition changes with the microstructure which is affected by the preparation method of the Ni-based cermet. Therefore, the Ni–GDC cermet was prepared through the glycine nitrate combustion route. The catalytic activity of Ni–GDC (GN) for ammonia decomposition was higher than that of Ni–GDC (PM) in the temperature range of 450-600^{o}C as shown in Fig. 2. 8. In Fig. 2. 9, the anodic overpotential in wet H_2 demonstrated no significant difference between two Ni–GDC cermets from different preparation routs. On the other hand, the anodic overpotential of Ni–GDC (GN) in NH_3 was lower than that of Ni–GDC (PM) at 600^{o}C. This led to the performance enhancement of the cell with Ni–GDC (GN) anode due to higher catalytic activity for ammonia decomposition.

The BET surface area for Ni–YSZ, Ni–GDC (PM), and Ni–GDC (GN) was 0.6, 0.7, and 1.3 m^2g^{-1}, respectively. Every cermet possessed the relatively small surface area after calcination at 1400^oC for 5 h and subsequent reduction at 1000^oC in hydrogen. However, the surface area of Ni–GDC (GN) was twice as that of Ni–GDC (PM). This indicates that the high activity of Ni–GDC (GN) is ascribed to the large surface area. The anodic polarization resistance for Ni–GDC (GN) was significantly lower in ammonia at 600 and 700^oC than that for Ni–GDC (PM), while that in hydrogen was almost comparable to each other (see Fig. 2. 10). The high catalytic activity of Ni–GDC (GN) for ammonia decomposition led to an increase in a hydrogen concentration in the vicinity of the anode, resulting in the high cell performance. Therefore, Ni–GDC prepared by the glycine nitrate process is preferable for direct NH_3–fueled SOFCs.

Furthermore, the microstructure of Ni–YSZ, Ni–GDC (PM), and Ni–GDC (GN) was observed by SEM (see Fig. 2. 11). A secondary electron detector and an in–lens detector were effective in observing the topographic image and in distinguishing Ni metal (bright particles) and oxide component (dark particles), respectively. In the case of Ni–YSZ, Ni metal aggregated to form large particles which were not dispersed well as in the case of Ni–GDC (PM) and Ni–GDC (GN). For Ni–GDC cermets, the ceria network prevented aggregation of Ni particles. The small particle size of Ni metal in the Ni–GDC (GN) anode led to the high ammonia decomposition activity, the abundant triple–phase boundary (TPB), and an increase in the rate of electrochemical oxidation of hydrogen produced from ammonia decomposition.

2. 4. Conclusions

High catalytic activity of anode material for ammonia decomposition plays a crucial role for direct NH_3–fueled SOFCs because the ammonia oxidation over the SOFC anode takes place in two steps; *i.e.*, catalytic ammonia decomposition to H_2 and N_2 followed by electrochemical hydrogen oxidation.

The comparison of catalytic activities of Ni–YSZ and Ni–GDC revealed that the Ni–GDC cermet demonstrated higher activity for ammonia decomposition and less retardation to hydrogen than Ni–YSZ. Doped–ceria possessed a large number of basic sites on its surface which were favourable for ammonia decomposition reaction. The performances of SOFCs with the Ni–YSZ and Ni–GDC anodes were compared in humidified H_2 and NH_3 fuels. The anodic polarization resistance of Ni–GDC anode in NH_3 was smaller than that of Ni–YSZ at 600^oC. The hydrogen concentration estimated from the limiting current for ammonia fuel was higher for Ni–GDC than for Ni–YSZ. This indicates that the SOFC performance was enhanced by using Ni–GDC anode because of the mixed ionic–electronic conductivity of GDC under reducing atmospheres as well as the high catalytic activity for ammonia decomposition. Moreover, the contribution of preparation method of anode material for the ammonia catalytic decomposition and the cell performance was investigated. It was found that the cell performance was enhanced by using Ni–GDC prepared through the glycine–nitrate combustion route because of a good distribution of the small Ni particles within anode microstructure which led to the extension of the triple–phase boundary (TPB) and the enhancement of the electrochemical oxidation of hydrogen produced from ammonia decomposition.

References

[1] P. E. Dodds, I. Staffell, A. D. Hawkes, F. Li, P. Grunewald, W. McDowall, P. Ekins, *Int. J. Hydrogen Energy*, **40**, 2065–2083 (2015).

[2] MC. Williams, *FuelCells*, **1**, 87–91 (2001).

[3] F. Zink, Y. Lu, L. Schaefer, *Energ. Convers. Manage.*, **48**, 809–818 (2007).

[4] R.A. George, *J. Power Sources*, **86**, 134–139 (2000).

[5] C. J. Winter, Int. *J. Hydrogen Energy*, **34**, S1–S52 (2009).

[6] T.N. Veziroglu, Int. Scien. *J. for Alternative Energy and Ecology*, **4**, 29–39 (2007).

[7] J.O. Jensen, A.P. Vestbo, Q. Li,N.J. Bjerrum, *J. of Alloys and Compounds*, **446–447**, 723–728 (2007).

[8] A.S. Chellappa, C.M. Fischer, W.J. Thomson, *Appl. Catal. A–Gen.*, **227**, 231–240 (2002).

[9] L. Zhang, Y. Cong, W. Yang, L. Lin, *Chinese J Catal.*, **28**, 749–751(2007).

[10] C. Zamfirescu, I. Dincer, *J. Power Sources*, **185**, 459–465 (2008).

[11] G. Cinti, U. Desideri, D. Penchini,G. Discepoli, **Fuel Cells**, **14**, 221–230 (2014).

[12] C. H. Christensen, T. Johannessen, R. Z. Sørensen, J. K. Nørskov, *Catal. Today*, **111**, 140–144 (2006).

[13] F. Ishak, I. Dincer, C. Zamfirescu, *J. Power Sources*, **202**, 157–165 (2012).

[14] A. F. S. Molouk, T. Okanishi, H. Muroyama, T. Matsui, K. Eguchi, *J. Electrochem. Soc.*, **162**, F1268–F1274 (2015).

[15] S.P. Jiang , P.J. Callus , S.P.S. Badwal, *Solid State Ionics*, **132**, 1–14 (2000).

[16] H.J. Cho, G.M. Choi, *J. Power Sources*, **176**, 96–101 (2008).

[17] W. Ana, D. Gatewoodb, B. Dunlapb, C. Heath Turner, *J. Power Sources*, **196**, 4724–4728 (2011).

[18] M. Marinsek, K. Zupan, J. Macek, *J. Power Sources*, **86**, 383–389 (2000).

[19] D.H. Prasad, H.I. Ji, H.R. Kim, J.W. Son, B.K. Kim, H.W. Lee, J.H. Lee, *Appl. Catal.*

B–Environ., **101**, 531–539 (2011).

[20] S. Souentie, M. Athanasiou, D.K. Niakolas, A. Katsaounis, S.G. Neophytides, C.G. Vayenas, *J.Catal*., **306**, 116–128 (2013).

[21] S. Zha, W. Rauch, M. Liu, *Solid State Ionics*, **166**, 241–250 (2004).

[22] C. Fu, S. H. Chan, Q. Liu, X. Ge, G. Pasciak, *Int. J. Hydrogen Energy*, **35**, 301–307 (2010).

[23] T. Matsui R. Kishida, J. Kim, H., K. Eguchi, *J. Electrochem. Soc*., **157**, B776–B781 (2010).

[24] J. Yang, T. Akagi, T. Okanishi, H. Muroyama, T. Matsui, K. Eguchi, *Fuel Cells*, **15**, 390–397 (2015).

[25] M.C.J. Bradford, P.E. Fanning, M.A. Vannice, *J. Catal*., **172**, 479–484 (1997).

[26] D.G. Löffler, L.D. Schmidt, *J. Catal*., **41**, 440–454 (1976).

[27] W. Tsai, W.H.Weinberg, *J. Phys. Chem*., **91**, 5302–5307 (1987).

[28] J. Yang, A. F. S. Molouk, T. Okanishi, H. Muroyama, T. Matsui, K. Eguchi, *ACS Appl. Mater. Interfaces*, **7**, 7406–7412 (2015).

[29] S. Zha, W. Rauch, M. Liu, *Solid State Ionics*, **166**, 241–250 (2004).

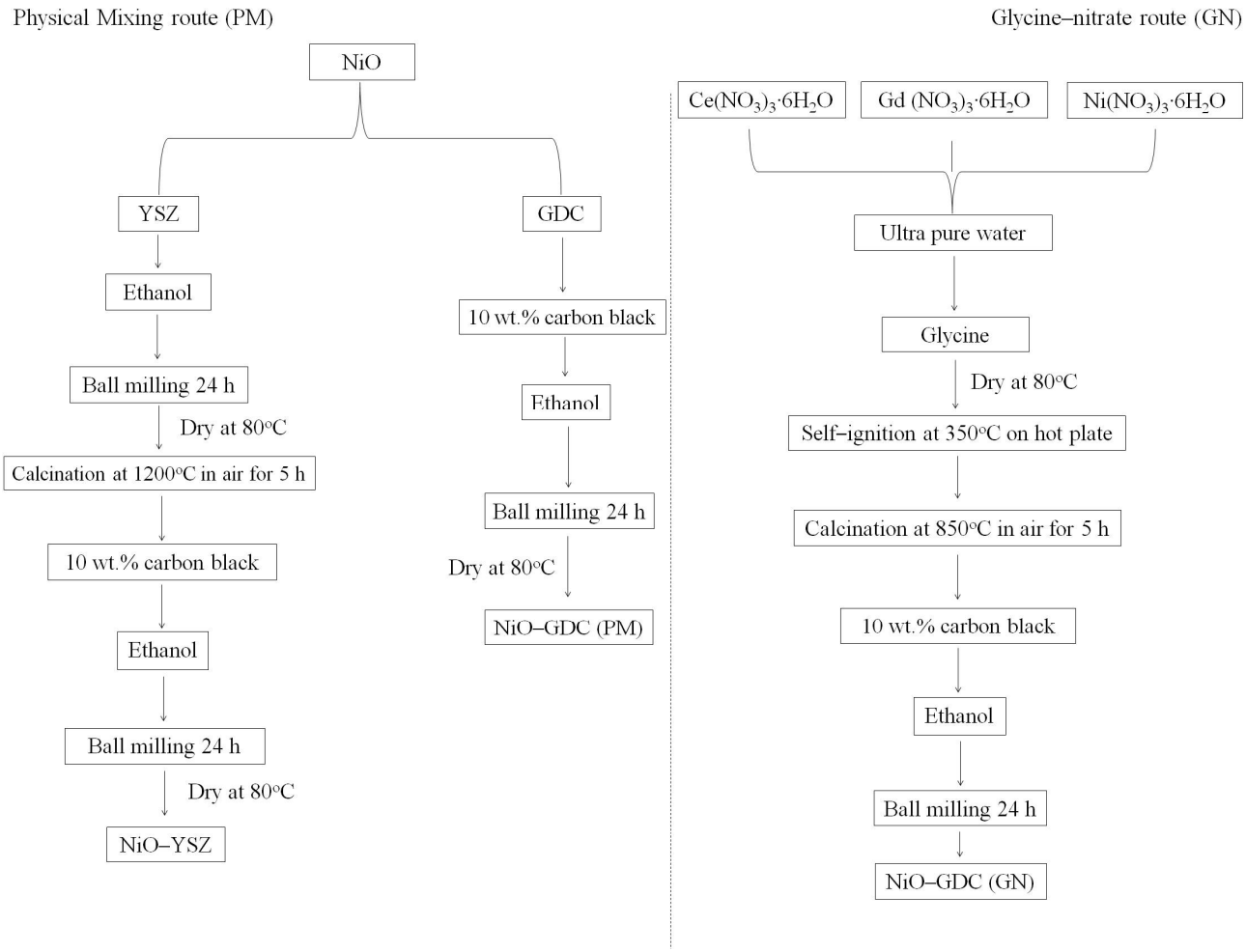

Figure 2. 1. Schematic diagram of the preparation routes for Ni–YSZ and Ni–GDC.

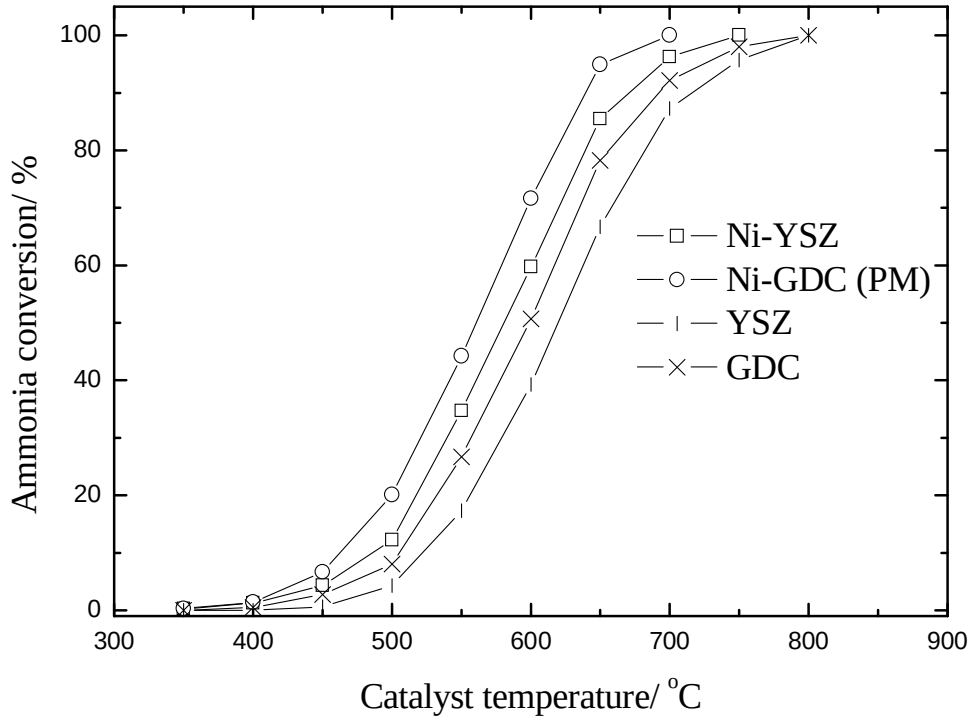

Figure 2. 2. Ammonia conversion over Ni–YSZ, Ni–GDC (PM), YSZ, and GDC as a function of catalyst temperature. Reaction condition; 66.7% NH_3−33.3% Ar, gas space velocity = 6000 l kg^{-1} h^{-1}.

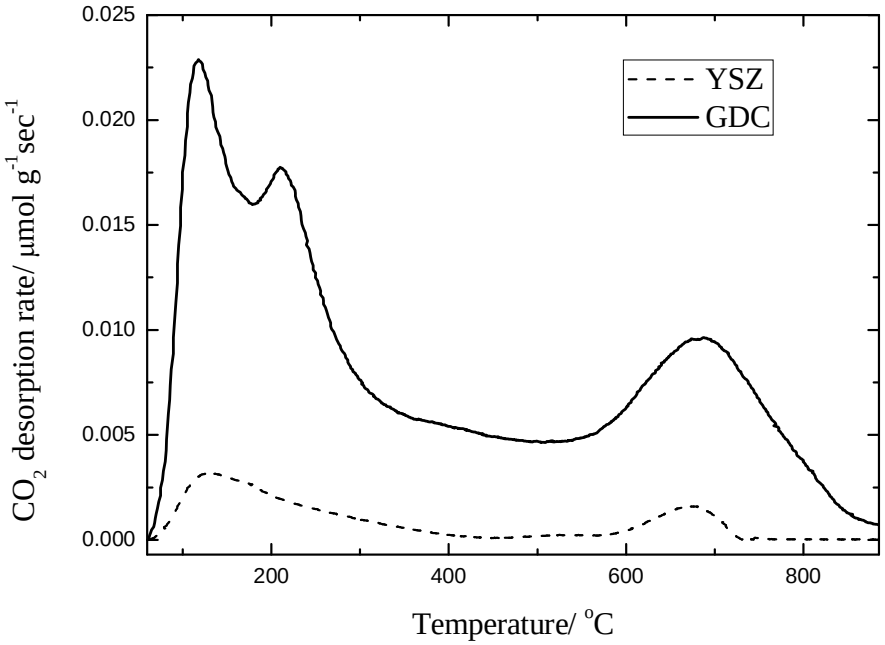

Figure 2. 3. Temperature programmed desorption of CO_2 (CO_2−TPD) for YSZ and GDC.

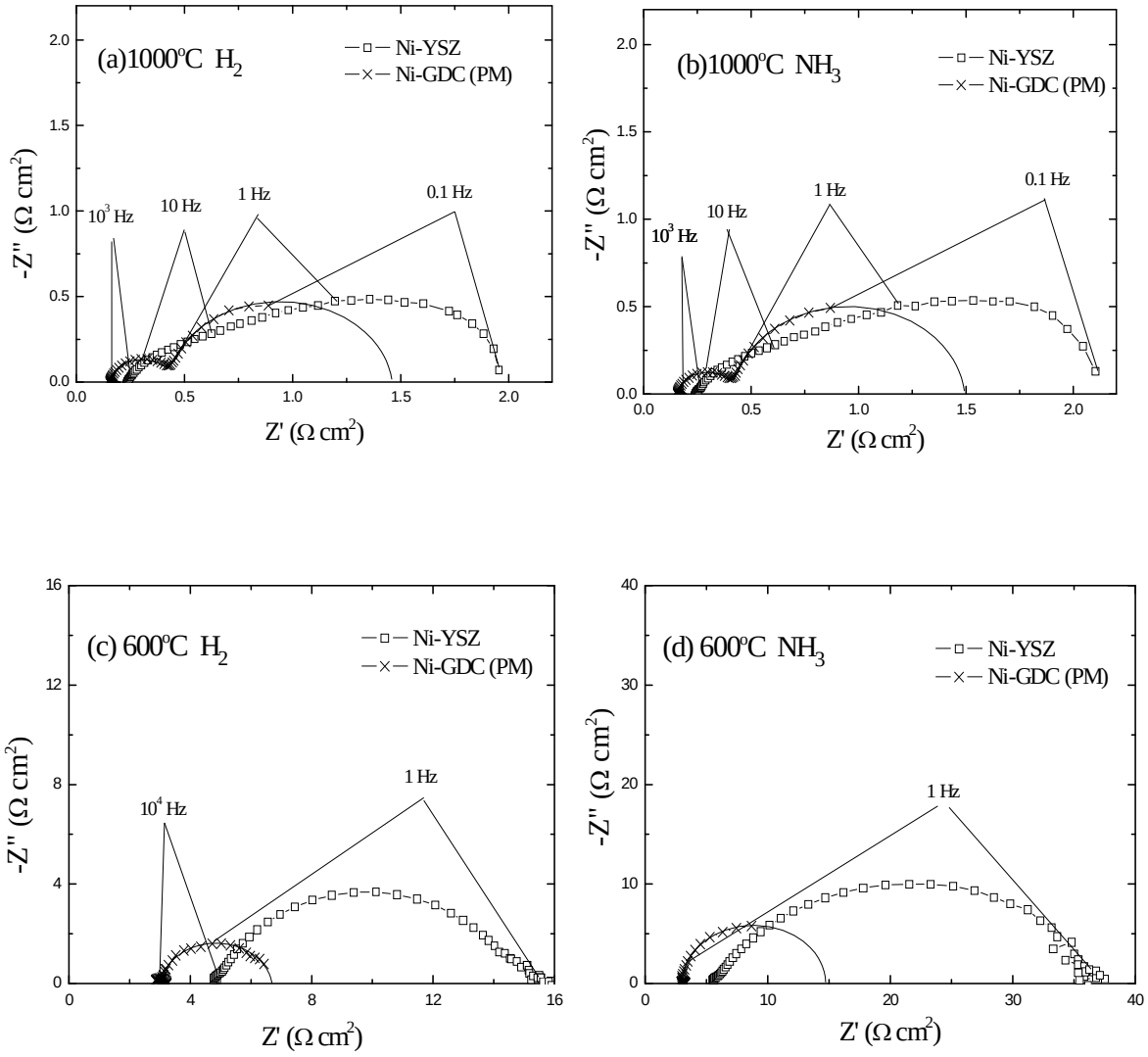

Figure 2. 4. Impedance spectra for Ni–YSZ and Ni–GDC (PM) anodes at 600°C and 1000°C in wet H_2 and NH_3 fuel. Anode gas; 60% H_2–0.5% H_2O–39.5% Ar (flow rate; 100 ml min^{-1}) and 66.7% NH_3–0.8% H_2O–32.5% Ar (flow rate; 60 ml min^{-1}). Cathode gas; O_2 (flow rate; 100 ml min^{-1}).

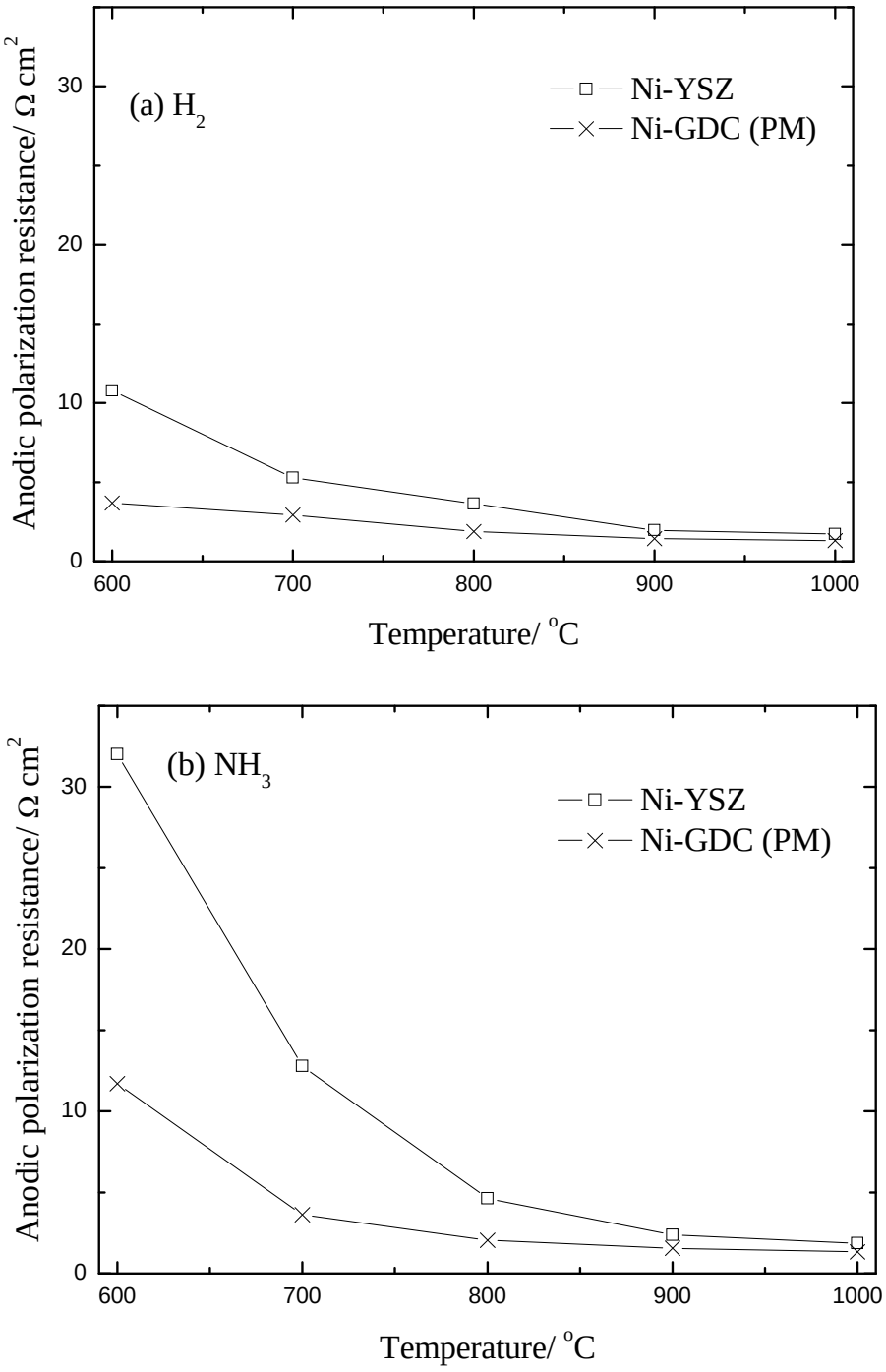

Figure 2. 5. Anodic polarization resistance for Ni−YSZ and Ni−GDC (PM) in wet (a) H_2 and (b) NH_3 at 600−1000°C. Anode gas; 60% H_2–0.5% H_2O–39.5% Ar (flow rate; 100 ml min^{-1}) and 66.7% NH_3–0.8% H_2O–32.5% Ar (flow rate; 60 ml min^{-1}). Cathode gas; O_2 (flow rate; 100 ml min^{-1}).

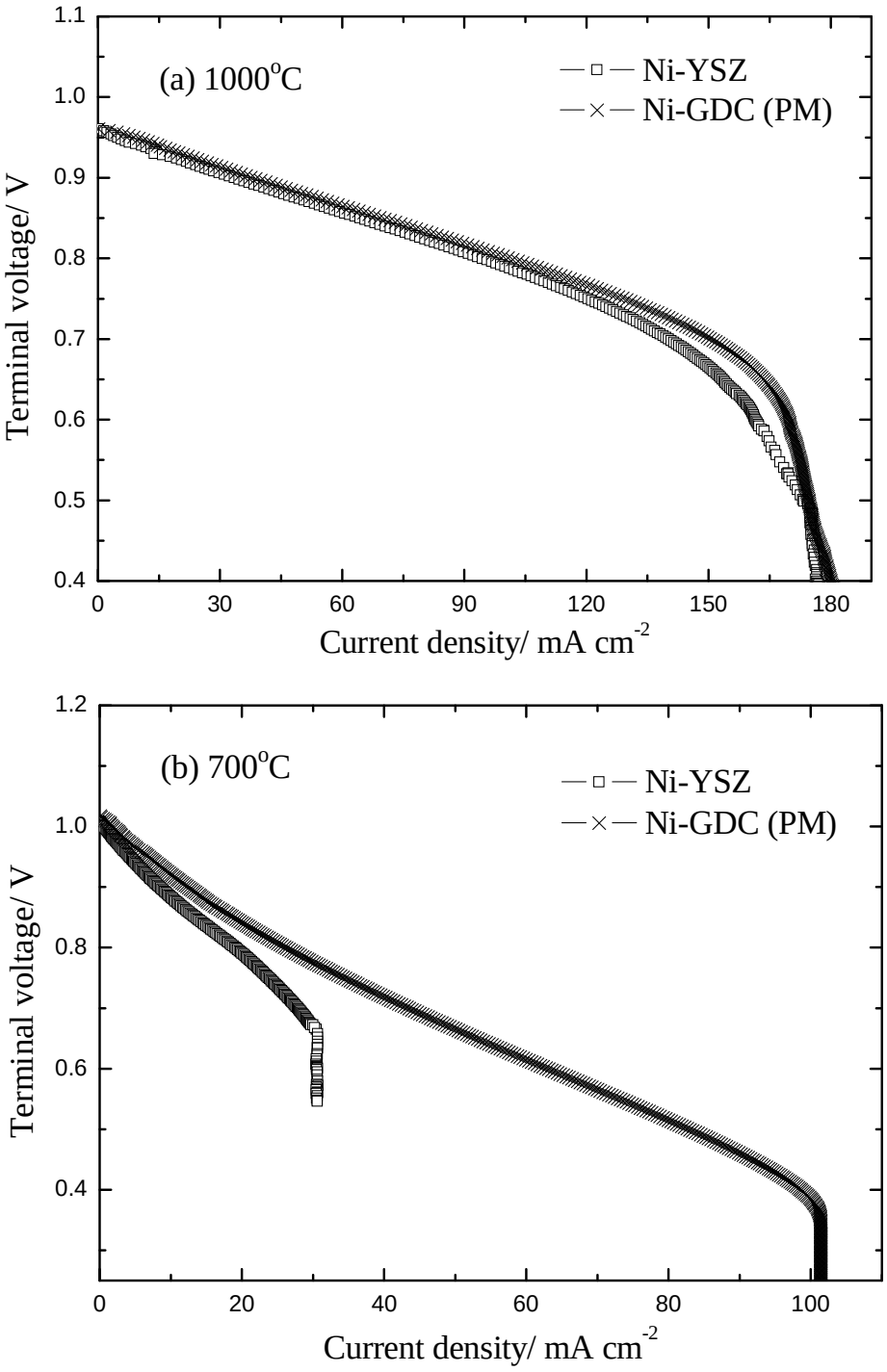

Figure 2. 6. *I*−*V* curves for the cell of Ni−YSZ|YSZ|LSM and Ni−GDC (PM)|YSZ|LSM at (a) 1000°C and (b) 700°C. Anode gas; 0.7% NH_3–0.5% H_2O–98.8% Ar (flow rate; 100 ml min^{-1}). Cathode gas; O_2 (flow rate; 100 ml min^{-1}).

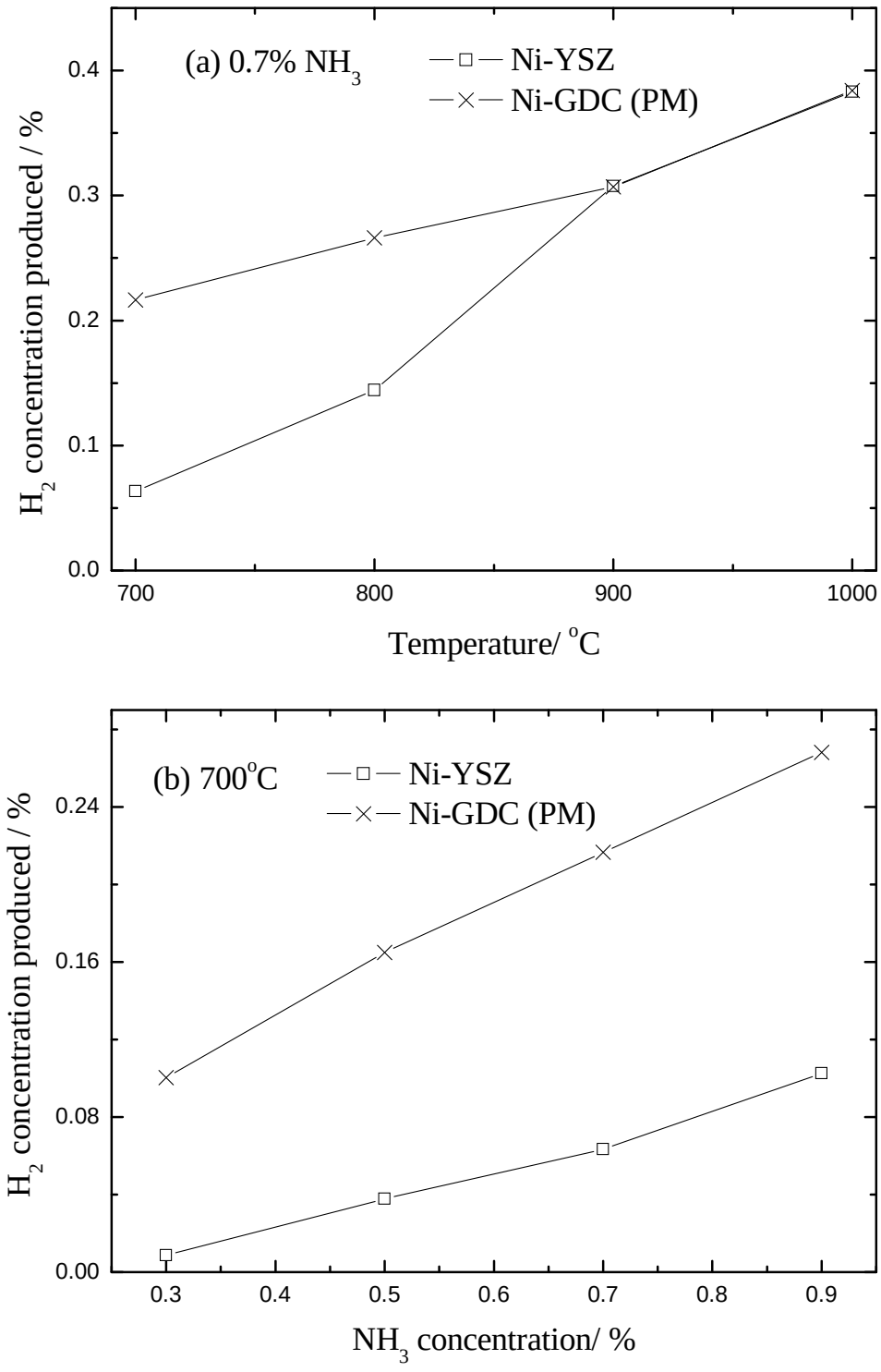

Figure 2. 7. H_2 concentration produced from ammonia decomposition at the limiting current as a function of (a) temperature and (b) ammonia concentration. Anode gas; *x*% NH_3–0.5% H_2O–(99.5–*x*)% Ar (*x* = 0.3-0.9%, flow rate; 100 ml min^{-1}). Cathode gas; O_2 (flow rate; 100 ml min^{-1}).

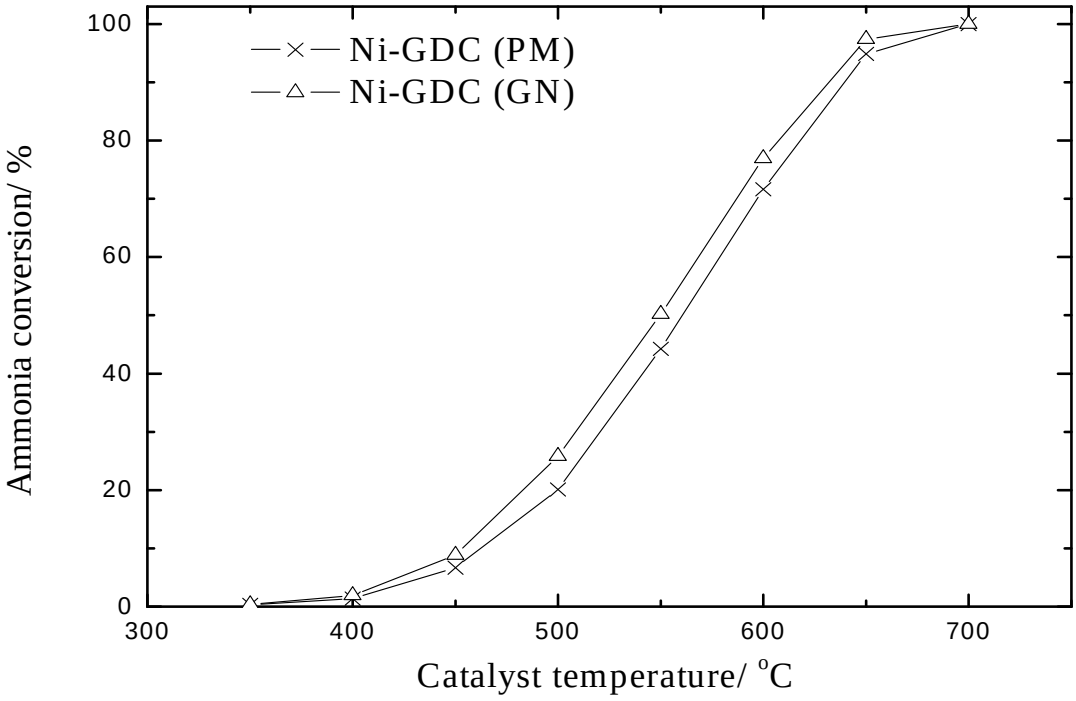

Figure 2. 8. Ammonia conversion over Ni−GDC (PM) and Ni−GDC (GN) as a function of catalyst temperature. Reaction condition; 66.7% NH_3−33.3% Ar, gas space velocity = 6000 l kg^{-1} h^{-1}.

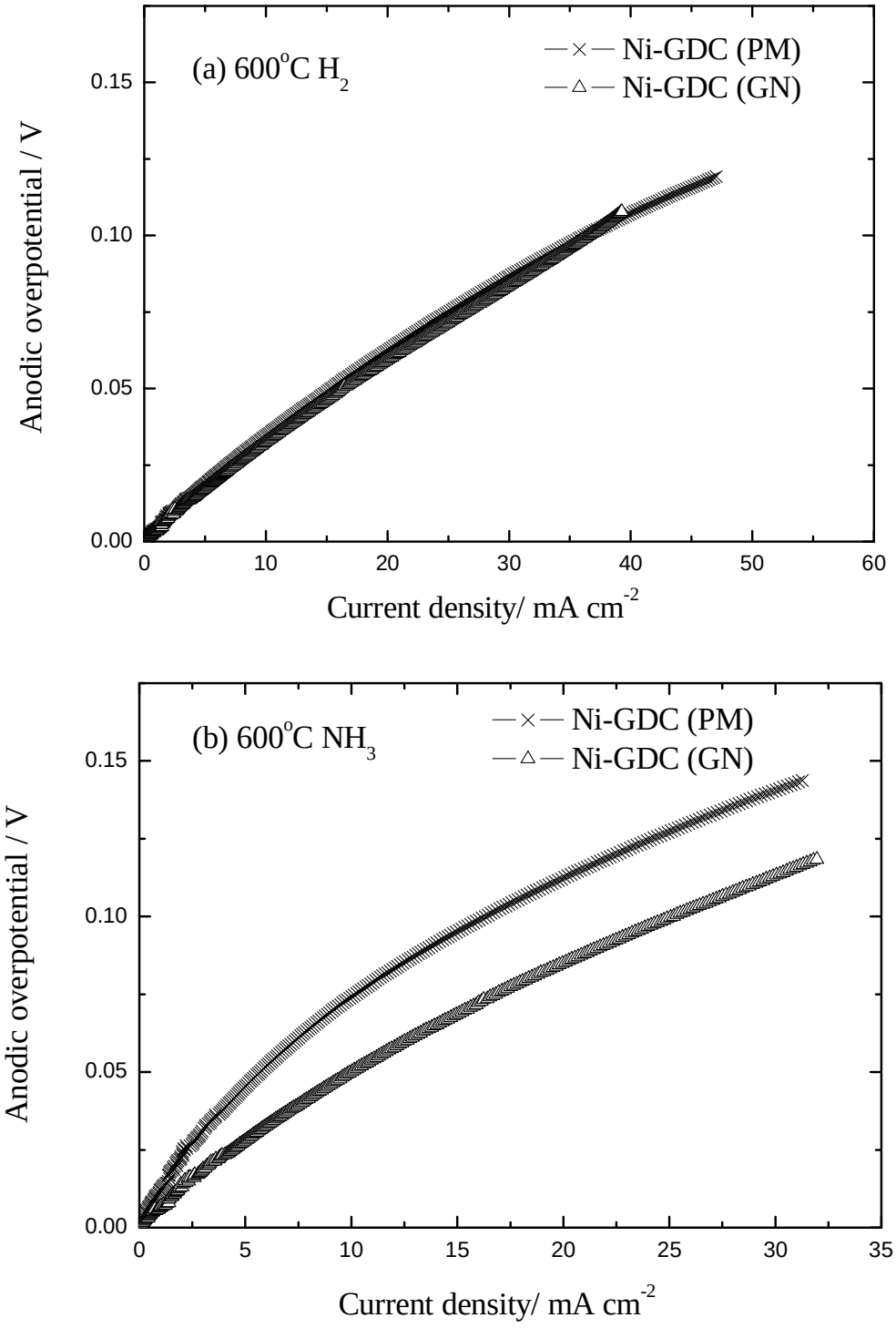

Figure 2. 9. Anodic overpotential for Ni−GDC (PM) and Ni−GDC (GN) in wet (a) H_2 and (b) NH_3 fuel at 600°C. Anode gas; 60% H_2–0.5% H_2O–39.5% Ar (flow rate; 100 ml min^{-1}) and 66.7% NH_3–0.8% H_2O–32.5% Ar (flow rate; 60 ml min^{-1}). Cathode gas; O_2 (flow rate; 100 ml min^{-1}).

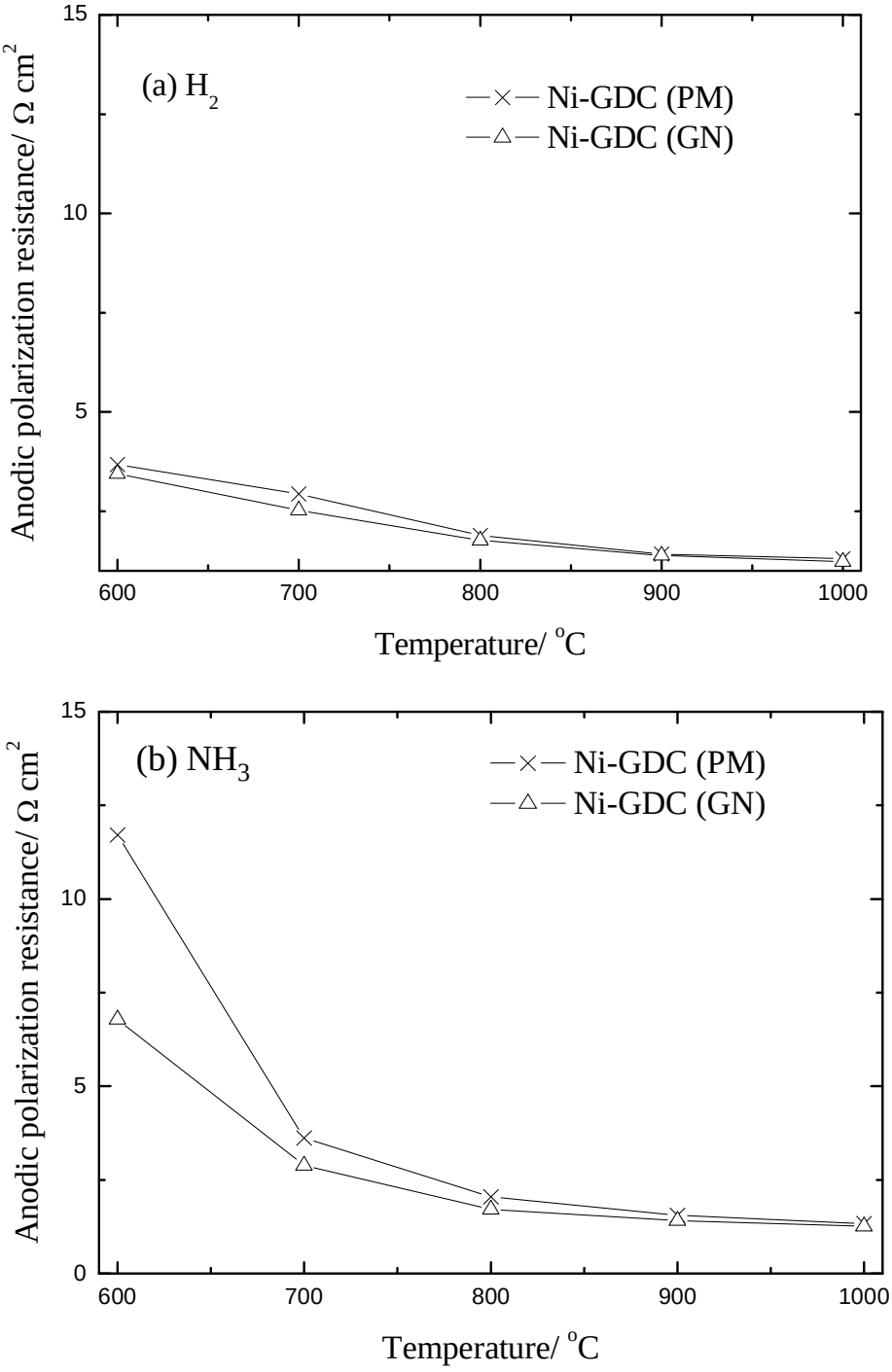

Figure 2. 10. Anodic polarization resistance (a) in H_2 and (b) NH_3 fuel. Anode gas; 60% H_2–0.5% H_2O–39.5% Ar (flow rate; 100 ml min^{-1}) and 66.7% NH_3–0.8% H_2O–32.5% Ar (flow rate; 60 ml min^{-1}). Cathode gas; O_2 (flow rate; 100 ml min^{-1}).

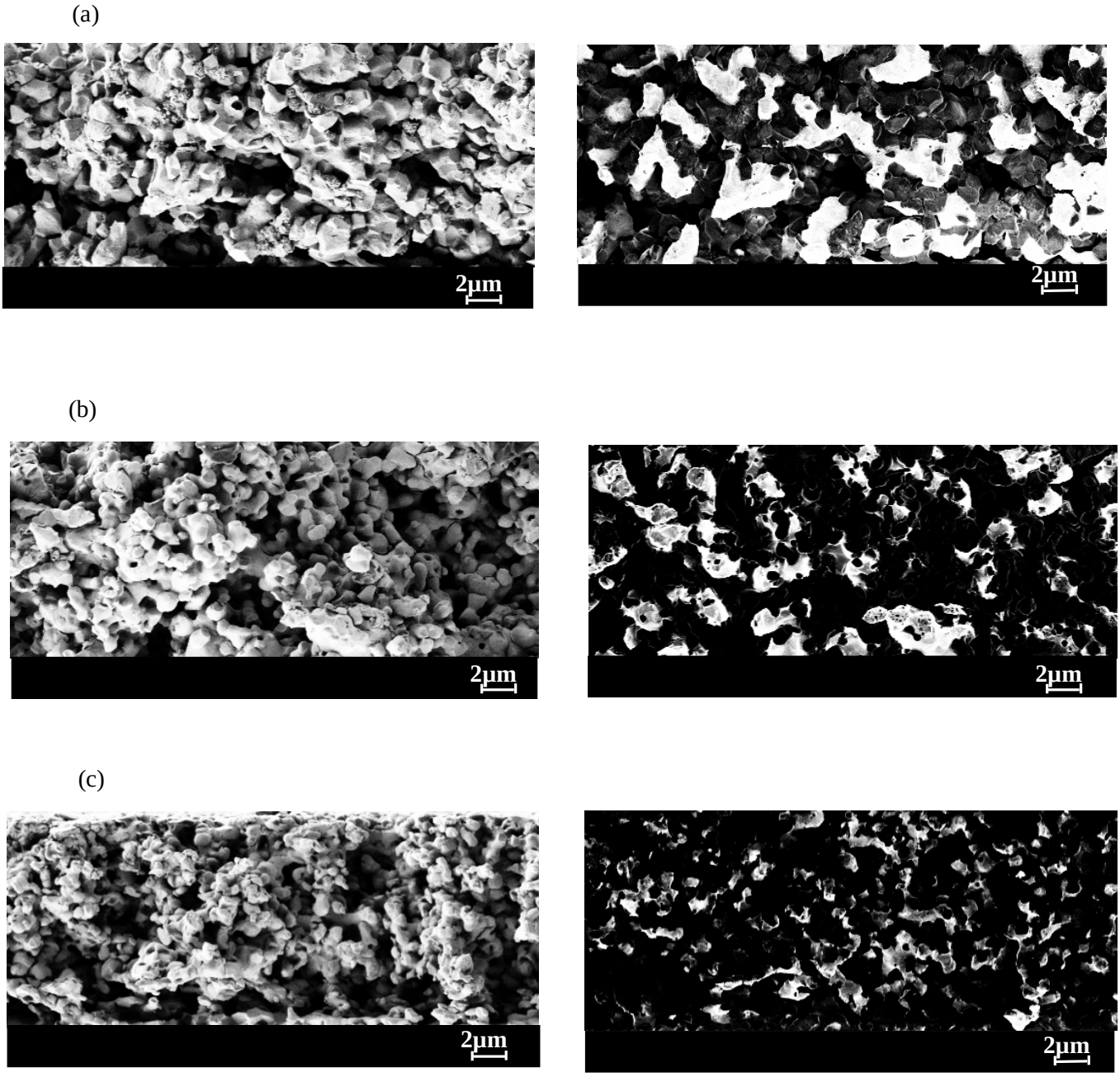

Figure 2. 11. Cross-sectional images of (a) Ni–YSZ, (b) Ni–GDC (PM), and (c) Ni–GDC (GN) anode obtained by a secondary electron detector (left images) and an in-lens detector (right images); bright particle Ni; dark phase YSZ or GDC.

Chapter 3

Ruthenium–promoted Nickel–ceria Anode Prepared by Infiltration Technique for Direct Ammonia Solid Oxide Fuel Cells.

3. 1. Introduction

Recently fuel cells emerged as an efficient power generation system because they convert the chemical energy stored in the fuels directly to electrical energy via electrochemical oxidation of fuel without need for direct combustion of fuel [1, 2]. Amongst the general advantages of fuel cells such as their high efficiency and environmentally benign characteristics, solid oxide fuel cell has additional advantages such as, higher power generation efficiency and fuel flexibility [3, 4]. Although hydrogen has been considered as fuel for solid oxide fuel cells (SOFCs) [5], problems arise on the production and storage of hydrogen [6–8]. Ammonia is an efficient hydrogen carrier because one mole of ammonia can produce 1.5 mole of hydrogen via thermal catalytic decomposition. Ammonia is carbon free fuel with higher energy density than hydrogen and is easy to store and transport [9–14]. The commercialization of direct NH_3–fueled SOFCs requires the development of appropriate anode materials with excellent performance at operation temperatures. It was reported that ammonia utilization with SOFCs proceeded in two steps; i.e., catalytic decomposition of ammonia to hydrogen and nitrogen and subsequent electrochemical oxidation of hydrogen [15, 16]. Therefore, in order to enhance the performance of direct NH_3–fueled SOFCs, it is necessary to find an active material for ammonia decomposition reaction as well as electrochemical oxidation of hydrogen.

Two possible routes for developing an anode material can be proposed. First approach is to optimize the conventional anode materials which have been demonstrated high performance. The other is to discover a novel material with high catalytic activity for fuel

oxidation as well as ionic and electronic conductivity [17, 18].

In general, the source oxide of anode (NiO–yttria–stabilized zirconia, YSZ) is sintered on the electrolyte at high temperature (*ca*. 1400^{o}C) to achieve good contact with YSZ electrolyte. The high temperature sintering accompanies significant grain growth and reduced electrocatalytic activity of the anode [19, 20]. This high temperature process limits the material choice because of melting point, thermal expansion mismatch, deleterious interaction between anode material and electrolyte [21, 22]. Infiltration is one of the most promising techniques for introducing variety of catalystic additives into the pre–sintered electrode scaffold. This process enables to design nanostructure composite electrodes with enlarged triple phase boundary [23]. Infiltration technique is carried out in two steps. At first, the electrode is sintered on the electrolyte at high temperature which ensures good bonding between them thereby achieving high conduction of electron or oxygen ion and structure stability of the electrode. Then, an additional catalyst component is deposited from its metal salt solution in the pre–sintered porous electrode body. The calcination of deposited additives can be carried out near the operation temperature of SOFC which is lower than that for sintering electrode on the electrolyte. Metal or perovskite type oxide have been so far introduced to the anode [24–27] or cathode [28–31] microstructure by using infiltration technique to improve the electrocatalytic activity, electronic and ionic conductivity of the electrode.

This study in the current chapter was devoted to enhance the performance of direct NH_3–fueled SOFC by designing an active anode material for ammonia decomposition reaction as well as electrochemical hydrogen oxidation reaction using infiltration technique. Therefore, ammonia decomposition reaction was investigated over metal promoted Ni–gadolinia–doped ceria (GDC) catalyst. Infiltration technique was used to introduce Ru nanocatalyst to Ni–GDC anode scaffold to avoid sublimation of RuO_2. The electrochemical performance of Ru and Fe promoted Ni–GDC anode was studied and compared with

conventional Ni–GDC anode in hydrogen and ammonia fuels. Furthermore, the effect of Ru loading on the cell performance in hydrogen and ammonia fuel was discussed.

3. 2. Experimental

A commercial electrolyte disks of 8 mol% Y_2O_3–ZrO_2 (YSZ, Tosoh, 500 μm thickness and 24 mm diameter) were used for electrolyte supported cell. NiO–GDC anode cermet was prepared by mechanical mixing of NiO (Wako Pure Chemical Industries), $Ce_{0.9}Gd_{0.1}O_{1.95}$ (GDC, Shin–Etsu Chemical Co.), and 10 wt.% carbon black as a pore former in ethanol for 24 h. The content of Ni metal in the anode was 60 wt.% after reduction treatment at 1000°C. The cathode was selected to be the perovskite type oxide of $(La_{0.8}Sr_{0.2})_{0.97}MnO_3$ (LSM) and prepared as described elsewhere [32]. The obtained anode, and cathode powders were mixed with polyethyleneglycol (PEG, Wako Pure Chemical Industries) to form slurry.

Cells were fabricated by screen printing the anode slurry on a flat face of YSZ electrolyte disk and firing at 1400°C for 5 h. Then, the cathode was printed on the other face of the YSZ electrolyte and fired at 1150°C in air for 5 h. The electrode active area was 0.28 cm^2 and their thicknesses were 60 μm and 40 μm for anode and cathode, respectively. A platinum reference electrode was fastened by the platinum paste (Metalor Technologies) around the circumference of the YSZ disk and fired at 900°C in air for 2 h. After complete cell fabrication, RuO_2, or Fe_2O_3 was introduced to NiO–GDC anode scaffold by dripping a solution of $Ru(NO_3)_3$ (Tanaka Kikinozku, 3.874 wt.%) or 0.7M of $Fe(NO_3)_3{\cdot}9H_2O$ (Wako Pure Chemical Industries) on to the surface of NiO–GDC anode and the solution infiltrated the porous anode in air. The cell with infiltrated anode was fired at 500°C in air for 2 h. The weight of the cell was measured before and after infiltration process to determine the amount of the infiltrated metal oxide. Six cells tested in this study, the infiltrated metal concentration and anode abbreviations are summarized in Table1. The anodes are expressed as Ni–GDC–metal additive (weight percentage). The concentration of the introduced metal

increased by repeating the infiltration process. Finally, the cell was placed between two alumina tubes and sealed by Pyrex glass rings to prevent gas leakage.

Prior to the electrochemical tests, the anode was reduced at 1000^{o}C for 1 h. The anode gas mixtures for all power generation tests were 60% H_2–0.5% H_2O–39.5% Ar (flow rate; 100 ml min^{-1}) and 66.7% NH_3–0.8% H_2O–32.5% Ar (flow rate; 60 ml min^{-1}). The gas composition of NH_3–H_2O–Ar was chosen to achieve the same hydrogen concentration and flow rate of H_2–H_2O–Ar when the decomposition of ammonia completed. The cathode gas was 100% O_2 with a total flow rate of 100 ml min^{-1}. Electrochemical measurements were carried out by the CellTest system (Solartron Analytical, potentiostat/galvanostat 1470E and frequency response analyzer 1455A). Electrochemical impedance spectroscopy was carried out under the open circuit condition for the fuel cell employing different anodes at temperatures between 600 and 1000^{o}C in a frequency range from 0.1 to 10^5 Hz. The anodic polarization resistance was determined from the differences in the low and high frequency intercepts on the impedance curves. After power generation test in hydrogen and ammonia fuels the anode microstructure was observed by a scanning electron microscopy (SEM, Nvision 40, Carl Zeiss-SIINT) equipped with energy dispersive spectroscopy system (EDS/EDX, X-Max^{N} Silicon Drift Detector SDD, Oxford Analytical Instruments).

The NiO–GDC catalyst powder was prepared via similar procedure to anode cermit and then fired at 1400^{o}C in air for 5 h. The calcined powder was ball milled for 24 h. The obtained powder was impregnated with metal solution of $Ru(NO_3)_3$ (Tanaka Kikinozku, 3.874 wt.%), $Pd[(NO_2)_2](NH_3)_2$ (Tanaka Kikinozku, 4.571 wt.%), $Fe(NO_3)_3{\cdot}9H_2O$ (Wako Pure Chemical Industries), $C_{10}H_{14}MoO_6$ (Wako Pure Chemical Industries), $IrCl_3$ (Tanaka Kikinozku, 8.598 wt.%), or $RhCl_3$ (Tanaka Kikinozku, 4.647 wt.%) and then calcined at 500^{o}C in air for 2 h. The weight ratio of metal/NiO–GDC was 5/95. All powders were pressed into a pellet at 20 MPa and then pulverized to 12 mesh. The sample (0.6 g) was set in

a fixed bed reactor and then reduced in H_2–Ar at 700°C for 1 h. After cooling the sample in H_2 to 350°C, the reactor was purged with Ar (50 ml min^{-1} Ar for 30 min). The reactant gas of 66.7% NH_3 –33.3% Ar (total flow rate; 60 ml min^{-1}) was supplied to each catalyst with a space velocity of 6000 l kg^{-1} h^{-1}. The outlet gas was passed through two traps containing 3.5M H_2SO_4 solution (Wako Pure Chemical Industries) to dissolve the unreacted NH_3 and then the flow rate of outlet gas containing H_2–N_2–Ar, was measured by using a flow rate meter (VP3, Horiba STEC Co, Ltd.). NH_3 decomposition percentage can be calculated using Eq. (1).

$$NH_3 \text{ decomposition / \%} = \left(\frac{F\,(NH_3 \text{ inlet}) - F\,(NH_3 \text{ unreacted})}{F\,(NH_3 \text{ inlet})}\right) \times 100 \qquad (1)$$

where $F(NH_3$ inlet) and $F(NH_3$ unreacted) are the flow rate of ammonia in the inlet gas and unreacted ammonia in the outlet gas, respectively. The crystal structure of ruthenium–impregnated Ni–GDC catalyst was analyzed by X–ray diffraction (XRD) before and after ammonia decomposition test using Cu Kα radiation (Rigaku, Ultima IV X–ray diffractometere).

3. 3. Results and discussion

3. 3. 1. Catalytic activity of metal promoted Ni–GDC for ammonia decomposition

It was proven that the catalytic activity for ammonia decomposition is the key factor for designing an active anode for direct NH_3–fueled SOFC [33, 34]. In other words, it is expected that the performance of direct NH_3–fueled SOFC is enhanced by increasing catalytic activity of anode for ammonia decomposition. Among different metal catalysts studied for ammonia decomposition, ruthenium shows the highest performance [35]. Therefore, the catalytic activity of Ni–GDC impregnated with 5 wt.% of different metals (Pd, Ru, Rh, Mo, Fe, or Ir) for

ammonia decomposition was studied using a fixed bed reactor. It was observed that the ammonia decomposition was promoted by the addition of Pd, Ru, Rh, Fe, or Ir to Ni–GDC but retarded by the addition of Mo. Ruthenium–impregnated Ni–GDC demonstrated the highest catalytic activity for ammonia decomposition followed by iron–impregnated Ni–GDC (Fig. 3. 1). The XRD pattern for ruthenium–impregnated Ni–GDC in Fig. 3. 2 shows three distinguish phase which are NiO, RuO_2, and GDC before ammonia conversion test and Ni, Ru, and GDC after ammonia conversion test.

3. 3. 2. Comparison between electrochemical activity of iron and ruthenium infiltrated Ni–GDC for direct NH_3–fueled SOFCs

Ni–GDC anode cermet was chosen as a base material for infiltration because of its higher electrochemical and catalytic activity than the conventional Ni–YSZ anode cermet. It was proven that gadolinia-dope ceria (GDC) acted as a network preventing nickel particles from aggregation and the number of basic site on GDC surface is much higher than that on YSZ. Such basic sites are important for high activity for ammonia decomposition reaction because of weakened adsorption of NH_3 and facilitated dissociation of N–H bond [33]. Furthermore, it was found that a retardation by formed hydrogen on ammonia decomposition reaction below 800^{o}C was weaker for Ni–GDC than for Ni–YSZ [34, 36]. Ruthenium and iron were chosen as promoters due to their high catalytic activity for ammonia decomposition.

Electrochemical impedance spectroscopy was measured for Ni–GDC, Ni–GDC–Ru (7wt. %), and Ni–GDC–Fe (7wt. %) anodes. The impedance spectra of anodes in wet H_2 and NH_3 at 600^{o}C is shown in Fig. 3. 3. The anodic polarization resistance decreased with infiltrated anodes regardless of fuel. Ni–GDC–Ru (7wt. %) anode shows the lowest anodic polarization resistance among the anodes under study. However, the difference in anodic polarization resistance for Ni–GDC and infiltrated Ni–GDC anode in ammonia fuel is much higher than

that in hydrogen fuel. This indicates that ruthenium metal plays a synergistic role with nickel for both ammonia decomposition reaction and electrochemical hydrogen oxidation reaction. The promoting effect of ruthenium was higher than that for iron.

Figure 3. 4 shows (a) current-voltage (*I-V*) characteristics of the cells with Ni–GDC, Ni–GDC–Ru (7wt. %), and Ni–GDC–Fe (7wt. %) anode in ammonia fuel and (b) ammonia conversion at 600^{o}C. The fuel cell performance enhanced significantly when Ni–GDC anode infiltrated with ruthenium metal (see Fig. 3. 4(a)). The ammonia conversion was estimated from open circuit voltage (E_{OCV}) from the following procedure. The oxygen partial pressure at the anode was calculated from OCV using Nernst equation,

$$E_{OCV} = \frac{RT}{nF} \ln\left(\frac{P(O_2)_c}{P(O_2)_a}\right) \quad (2)$$

where R is the gas constant, T is the temperature, n is the number of transferred electron, F is the Faraday constant, and $P(O_2)_c$ and $P(O_2)_a$ are the oxygen partial pressure at the cathode and anode, respectively. The partial pressure of hydrogen, $P(H_2)$, produced by ammonia decomposition reaction was determined by using Eq. (3).

$$P(H_2) = \sqrt{\left(\frac{P(H_2O)^2}{K_1 \times P(O_2)_a}\right)} \quad (3)$$

where $P(H_2O)$ is the partial pressure of steam in the anode gas mixture, and K_1 is the equilibrium constant for hydrogen oxidation reaction. The ammonia conversion was calculated according to the following Eq. (4);

$$NH_3 \text{ decomposition / \%} = \left(\frac{n\,(NH_3 \text{ inlet}) - n\,(NH_3 \text{ unreacted})}{n\,(NH_3 \text{ inlet})}\right) \times 100 \quad (4)$$

where $n(NH_3$ inlet) and $n(NH_3$ unreacted) are the number of moles of ammonia in the inlet gas and unreacted ammonia in the outlet gas, respectively. Only hydrogen and water ratio is assumed to determine the partial pressure of oxygen. The ammonia conversion over Ni–GDC–Ru (7wt. %) anode is higher than that over Ni–GDC or Ni–GDC–Fe (7wt. %) anodes. This means that the hydrogen concentration produced by ammonia decomposition is higher for ruthenium infiltrated Ni–GDC (see Fig. 3. 4).

The SEM images were taken for Ni–GDC–Ru (7wt. %) and Ni–GDC–Fe (7wt. %) anode using secondary electron detector. The ruthenium and iron nano–particles were identified by EDS. Both infiltrated metals are spherical in shape and deposited on both Ni and GDC particles (see Fig. 3. 5). Therefore, the active surface for ammonia catalytic decomposition increased on both Ni and GDC particles as well as extending the triple phase boundary (TPB) for the electrochemical oxidation of hydrogen.

3. 3. 3. Impedance behavior for Ru–promoted Ni–GDC anode in hydrogen and ammonia fuels

The impedance spectra for Ni–GDC and Ni–GDC–Ru (3wt. %) anodes in wet H_2 and NH_3 at 600 and 1000^oC are shown in Fig. 3. 6. The polarization resistances for Ni–GDC and Ni–GDC–Ru (3wt. %) anodes were 1.30 and *ca.* 1 Ωcm^2, at 1000^oC, respectively in both H_2 and NH_3 fuels. At such high temperature, ammonia was completely decomposed to H_2; thus, the concentration of H_2 after decomposition was almost the same as that in H_2 fuel in the current experimental condition. Introduction of 3 wt. % of Ru to the conventional Ni–GDC anode led to a slight decrease in anodic polarization resistance in both wet H_2 and NH_3 fuels at 1000^oC. Therefore, the anodic polarization resistance was slightly reduced in presence of Ru due to enhancement of the hydrogen electrochemical oxidation. On the other hand, addition of Ru to the Ni–GDC anode caused a decrease in anodic polarization resistance from

3.7 to 3.2 Ωcm^2 in H_2 fuel at 600^oC. However, the anodic polarization resistance was significantly different between Ni–GDC and Ni–GDC–Ru (3wt. %) anodes at 600^oC in NH_3 fuel. The promotion effect for Ni–GDC–Ru (3wt. %) anode at 1000^oC is small as compared with that at 600^oC in wet NH_3 fuel (Fig. 3. 6). Therefore, the large decrease in the anodic polarization resistance in the presence of ruthenium is related to enhancement in the ammonia decomposition reaction.

Figure 3. 7 summarises the anodic polarization resistance at different temperatures for two anodes in H_2 and NH_3 fuels at 600–1000^oC. The difference in anodic polarization resistance for Ni–GDC and Ni–GDC–Ru (3wt. %) anodes is small in all temperature range in the case of H_2 fuel. However, the difference in anodic polarization resistance for both anodes in wet NH_3 increased with decreasing temperature. This tendency indicates that addition of ruthenium to Ni–GDC anode scaffold promotes ammonia decomposition reaction.

3. 3. 4. Effect of ruthenium concentration on the electrochemical activity of the cell

The ruthenium concentration was changed by repeating the infiltration process. Mapping analysis was carried out for Ni–GDC, Ni–GDC–Ru (3wt. %), and Ni–GDC–Ru (8wt. %) anode after power generation test in hydrogen and ammonia fuels using EDS. The ruthenium spherical particles were deposited on both nickel and GDC particles in nanoscale with an average particle size *ca*. 200 nm. After first infiltration process, the ruthenium nano–particles was introduced to Ni–GDC microstructure; then the number of nano–particles increased with repeated infiltration process (see Fig. 3. 8). Ruthenium nano–particles were distributed along the Ni–GDC anode thickness reaching to the contact area between anode and YSZ electrolyte.

The impedance spectra for Ni–GDC, Ni–GDC–Ru (3wt. %), Ni–GDC–Ru (5wt. %), Ni–GDC–Ru (7wt. %), and Ni–GDC–Ru (8wt. %) anodes in wet H_2 and NH_3 fuels at 600^oC

are shown in Fig. 3. 9. The anodic polarization resistance for all anodes in H_2 fuel is lower than that in NH_3. However, addition of ruthenium to Ni–GDC anode led to dramatically decrease in the anodic polarization resistance in NH_3 fuel compared with that in H_2 fuel. Figure 3. 10 summarizes the ruthenium concentration dependence of the anodic polarization resistance in H_2 and NH_3 fuel at 600^oC. The anodic polarization resistance decreased significantly by increasing ruthenium concentration especially in NH_3 fuel. This indicates that, Ru–promoted Ni–GDC anode is an effective catalyst for ammonia decomposition reaction.

Figure 3. 11 (a) summarizes the anodic overpotential as a function of ruthenium concentration in H_2 and NH_3 fuels at 600^oC and current density 30 mA cm^{-2} and (b) ammonia decomposition dependence on the ruthenium concentration. With an increase of ruthenium concentration, anodic overpotential decreased and the difference in anodic overpotential with conventional Ni–GDC in NH_3 fuel became large. Ammonia decomposition was calculated from the OCV values with the previous method (eq. 2–4). An increase of ruthenium concentration in the Ni–GDC anode scaffold led to a noticeable enhancement of ammonia decomposition.

3. 4. Conclusions

For development of NH_3–fuled SOFCs, the catalytic activity of anode material for ammonia decomposition reaction was investigated. The catalytic activity test for ammonia decomposition was carried out employing the conventional Ni–GDC anode material with and without impregnation of Pd, Ru, Ir, Fe, Rh, and Mo. It was found that the ruthenium impregnated Ni–GDC demonstrated the highest catalytic activity for ammonia decomposition reaction followed by iron impregnated Ni–GDC. Infiltration technique was used to avoid such high temperature for anode processing. A ruthenium infiltrated Ni–GDC anode show a higher electrochemical and catalytic activity for NH_3–fuled SOFC compared with iron

infiltrated Ni–GDC and conventional Ni–GDC anode.

It was found that there is a great dependence between ruthenium concentration and both electrochemical and catalytic activity of anode for ammonia decomposition reaction.

References

[1] B. C. H. Steele, A. Heinzel, *Nature*, **414**, 345–352 (2001).

[2] B. C. H. Steele, *J. Mater. Sci*., **36**, 1053–1068 (2001).

[3] S. C. Singhal, *Solid State Ionics*, **135**, 305–313 (2000).

[4] O. Yamamoto, *Electrochim. Acta*, **45**, 2423–2435 (2000).

[5] C. J. Winter, *Int. J. Hydrogen Energy*, **34**, S1–S52 (2009).

[6] J. O. Jensen, A. P. Vestbo, Q. Li, N. J. Bjerrum, *J. Alloy. Compd.*, **446–447**, 723–728 (2007).

[7] S. Sharma, S. K. Ghoshal, *Renew. Sust. Energy Rev*., **43**, 1151–1158 (2015).

[8] C. Zamfirescu, I. Dincer, *Fuel Process. Technol*., **90**, 729–737 (2009).

[9] A. Klerke, C. H. Christensen, J. K. Nørskov, T. Vegge, *J. Mater. Chem.*, **18**, 2285–2392 (2008).

[10] C. Zamfirescu, I. Dincer, *J. Power Sources*, **185**, 459–465 (2008).

[11] C. H. Christensen, T. Johannessen, R. Z. Sørensen, J. K. Nørskov, *Catal. Today*, **111**, 140–144 (2006).

[12] F. Ishak, I. Dincer, C. Zamfirescu, *J. Power Sources*, **202**, 157–165 (2012).

[13] Z. Limin, C. You, Y. Weishen, L. Liwu, *Chin. J. Catal*., **28**, 749–751 (2007).

[14] G. Cinti, U. Desideri, D. Penchini, G. Discepoli, *Fuel Cells*, **14**, 221–230 (2014).

[15] A. F. S. Molouk, J. Yang, T. Okanishi, H. Muroyama, T. Matsui, K. Eguchi, *ECS Trans*., **68**, 2751-2762 (2015).

[16] J. Yang, T. Akagi, T. Okanishi, H. Muroyama, T. Matsui, K. Eguchi, *Fuel Cells*, **15**,

390–397 (2015).

[17] W. Z. Zhu, S. C. Deevi, *Mater. Sci. Eng.*, **A362**, 228–239 (2003).

[18] J. B. Goodenough, Y. H. Huang, *J. Power Sources*, **173**, 1–10 (2007).

[19] C. Sun, U. Stimming, *J. Power Sources*, **171**, 247–260 (2007).

[20] S. P. Jiang, Y. Duan, J. Love, G. *J. Electrochem. Soc*., **149**, A1175-A1183 (2002).

[21] S. P. Jiang, *Mater. Sci. Eng., A*, **418**, 199–210 (2006).

[22] R. J. Gorte, J. M. Vohs, S. McIntosh, *Solid State Ionics*, **175**, 1–6 (2004).

[23] R. J. Gorte, J. M. Vohs, *Curr. Opi. Colloid In. Sci.*, **14**, 236–244 (2009).

[24] L. Adijanto, A. Sampath, A. S. Yu, M. Cargnello, P. Fornasiero, R. J. Gorte, J. M. Vohs, *ACS Catal.*, **3**, 1801−1809 (2013).

[25] A. Babaei, S. P. Jiang, J. Li, *J. Electrochem. Soc*., **156**, B1022-B1029 (2009).

[26] S. P. Jiang, X. J. Chen, S. H. Chan, J. T. Kwok, *J. Electrochem. Soc*., **153**, A850-A856 (2006).

[27] W. Wang, S. P. Jiang, A. I. Y. Tok, L. Luo, *J. Power Sources*, **159**, 68–72 (2006).

[28] F. Liang, J. Chen, J. Cheng, S. P. Jiang, T. He, J. Pu, J. Li, *Electrochem. Commun.*, **10**, 42–46 (2008).

[29] J. Chena, F. Liang, B. Chi, J. Pu, S. P. Jiang, L. Jian, *J. Power Sources*, **194**, 275–280 (2009).

[30] T. Z. Sholklapper, C. Lu, C. P. Jacobson, J. S. Visco, L. C. D. Jonghe, *Electrochem. Solid-State Lett.*, **9**, A376-A378 (2006).

[31] M. Shah, S. A. Barnett, *Solid State Ionics*, **179**, 2059–2064 (2008).

[32] T. Matsui, R. Kishida, J. Kim, K. Eguchi, *J. Electrochem. Soc.*, **157**, B776–B781 (2010).

[33] A. F. S. Molouk, J. Yang, T. Okanishi, H. Muroyama, T. Matsui, K. Eguchi, *J. Power Sources*, **305**, 72–79 (2016).

[34] A. F. S. Molouk, J. Yang, T. Okanishi, H. Muroyama, T. Matsui, K. Eguchi, *J.*

Electrochem. Soc., **162**, F1268-F1274 (2015).

[35] S. F. Yin, Q. H. Zhang, B. Q. Xu, W. X. Zhu, C. F. Ng, C. T. Au, *J. Catal*., **224**, 384–396 (2004).

[36] J.Yang, A. F. S. Molouk, T. Okanishi, H. Muroyama, T. Matsui, K. Eguchi, *ACS Appl. Mater. Interfaces*, **7**, 7406–7412 (2015).

Table 3.1

Anode component and infiltrated metal concentration.

(60 wt.% Ni and 40 wt.% GDC)

Anode abbreviation	Infiltrated metal	Concentration of the infiltrated metal (wt. %)
Ni–GDC	—	0
Ni–GDC–Ru (3wt. %)	Ru	3
Ni–GDC–Ru (5wt. %)	Ru	5
Ni–GDC–Ru (7wt. %)	Ru	7
Ni–GDC–Ru (8wt. %)	Ru	8
Ni–GDC–Fe (7wt. %)	Fe	7

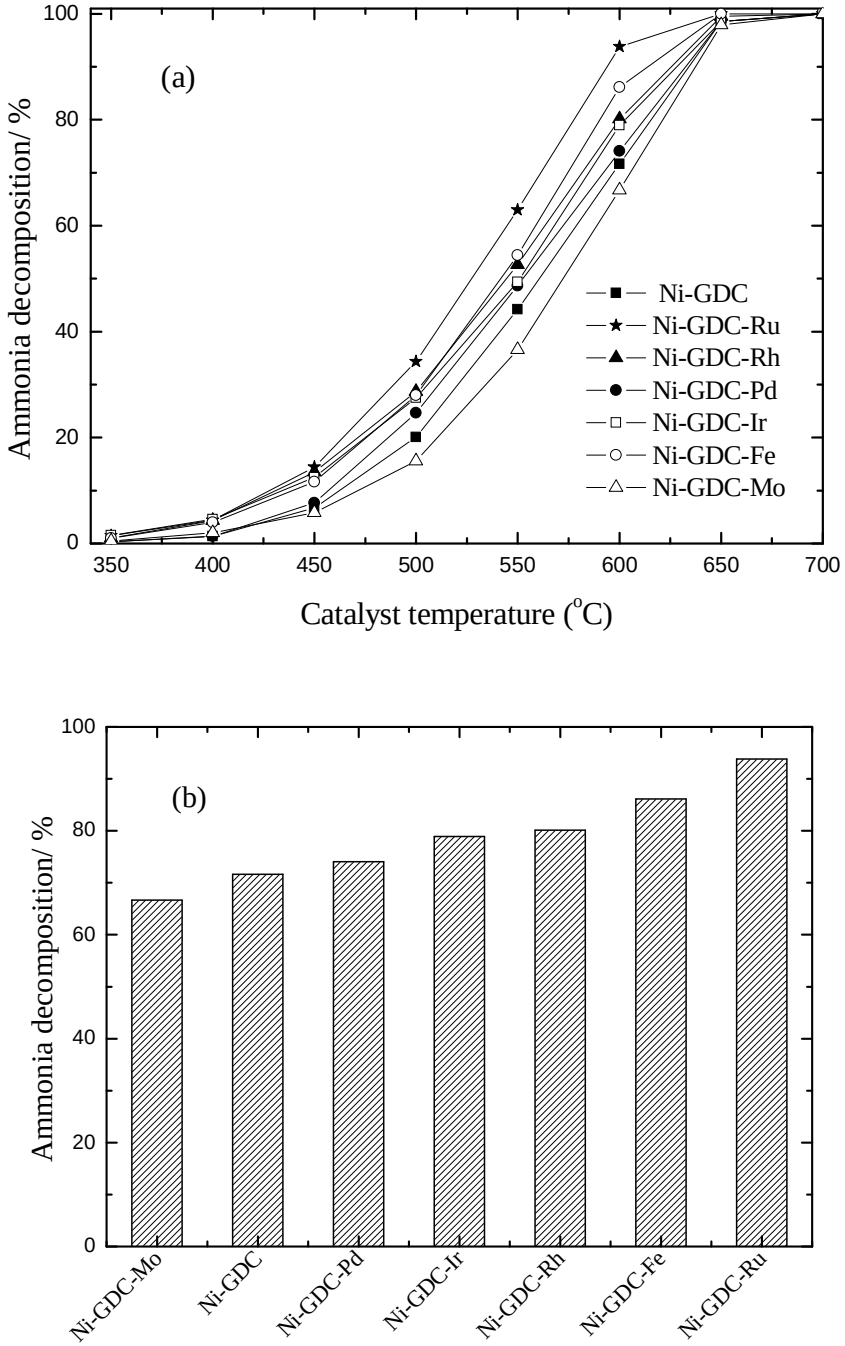

Figure 3. 1. (a) Ammonia decomposition over different catalysts as a function of catalyst temperature and (b) ammonia decomposition at 600°C over different catalysts. Reaction condition; 66.7% NH_3−33.3% Ar, gas space velocity = 6000 l kg^{-1} h^{-1}.

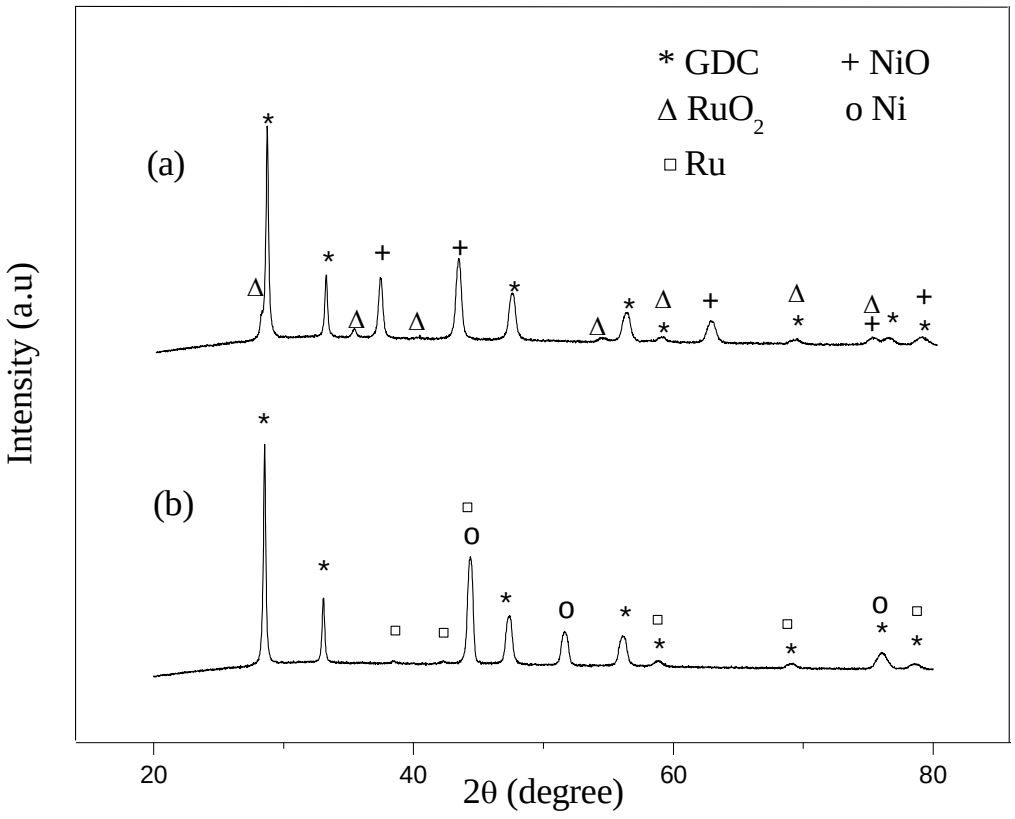

Figure 3. 2. XRD patterns of ruthenium–impregnated Ni–GDC (a) before and (b) after ammonia decomposition test.

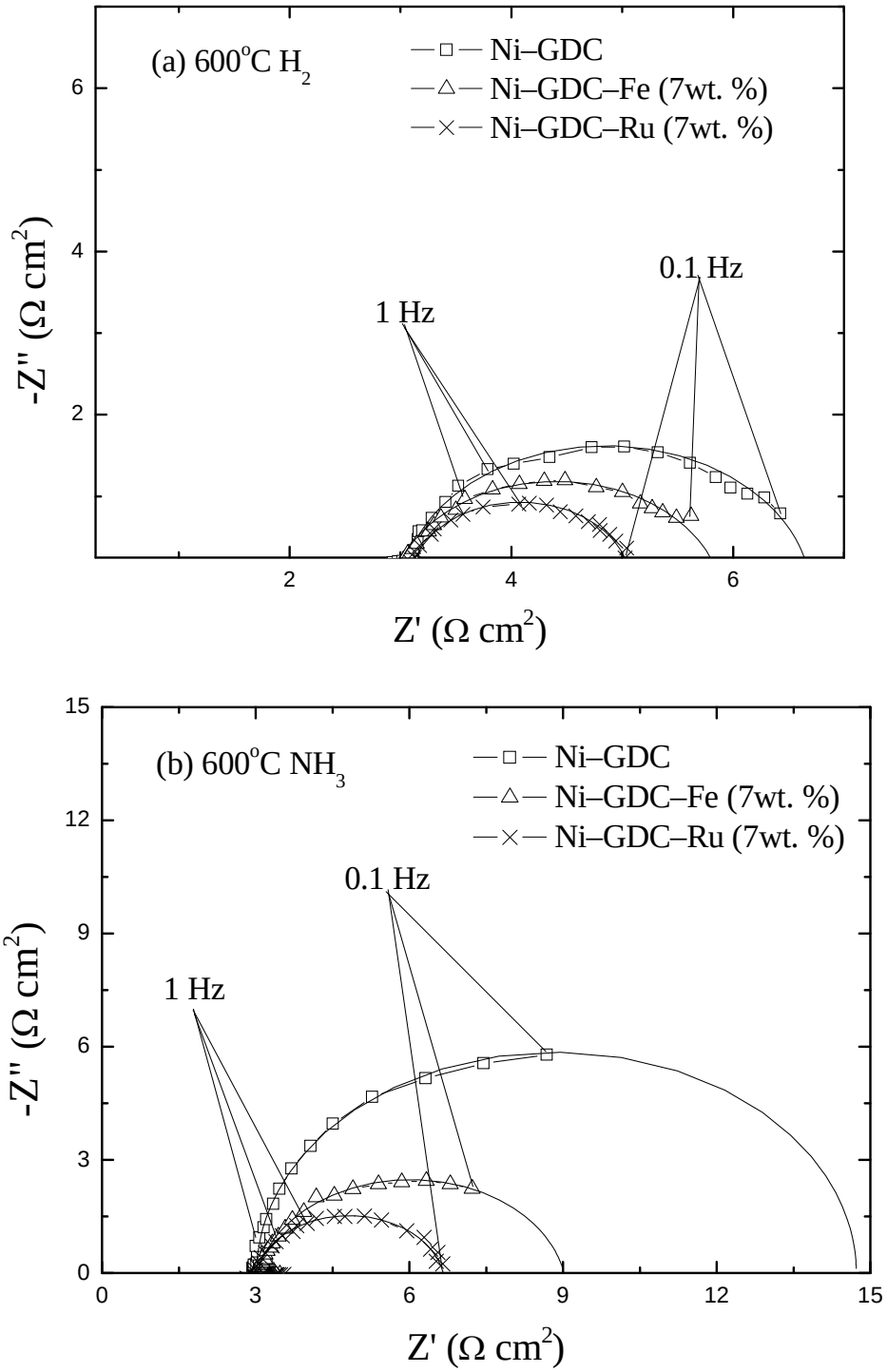

Figure 3. 3. Impedance spectra for Ni–GDC, Ni–GDC–Fe (7wt. %), and Ni–GDC–Ru (7wt. %) anodes at 600°C in wet H_2 and NH_3 fuel. Anode gas; 60% H_2–0.5% H_2O–39.5% Ar (flow rate; 100 ml min^{-1}) and 66.7% NH_3–0.8% H_2O–32.5% Ar (flow rate; 60 ml min^{-1}). Cathode gas; O_2 (flow rate; 100 ml min^{-1}).

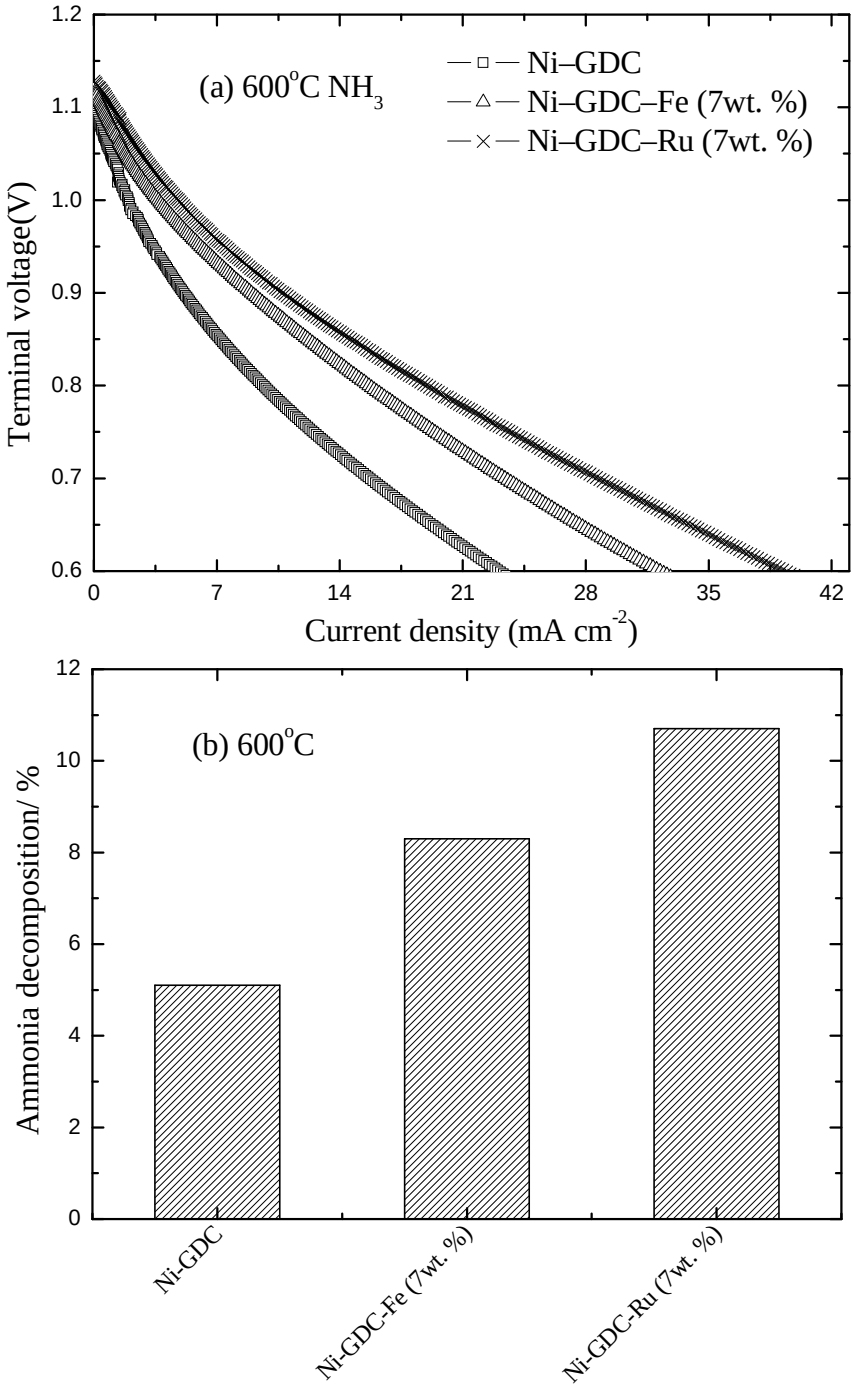

Figure 3. 4. (a) *I*−*V* curves for the cell of Ni−GDC|YSZ|LSM, Ni−GDC−Fe|YSZ|LSM, and Ni−GDC−Ru|YSZ|LSM and (b) ammonia decomposition calculated from the OCV data at 600°C over Ni–GDC, Ni–GDC–Fe (7wt. %), and Ni–GDC–Ru (7wt. %) anodes. Anode gas; 60% H_2–0.5% H_2O–39.5% Ar (flow rate; 100 ml min^{-1}) and 66.7% NH_3–0.8% H_2O–32.5% Ar (flow rate; 60 ml min^{-1}). Cathode gas; O_2 (flow rate; 100 ml min^{-1}).

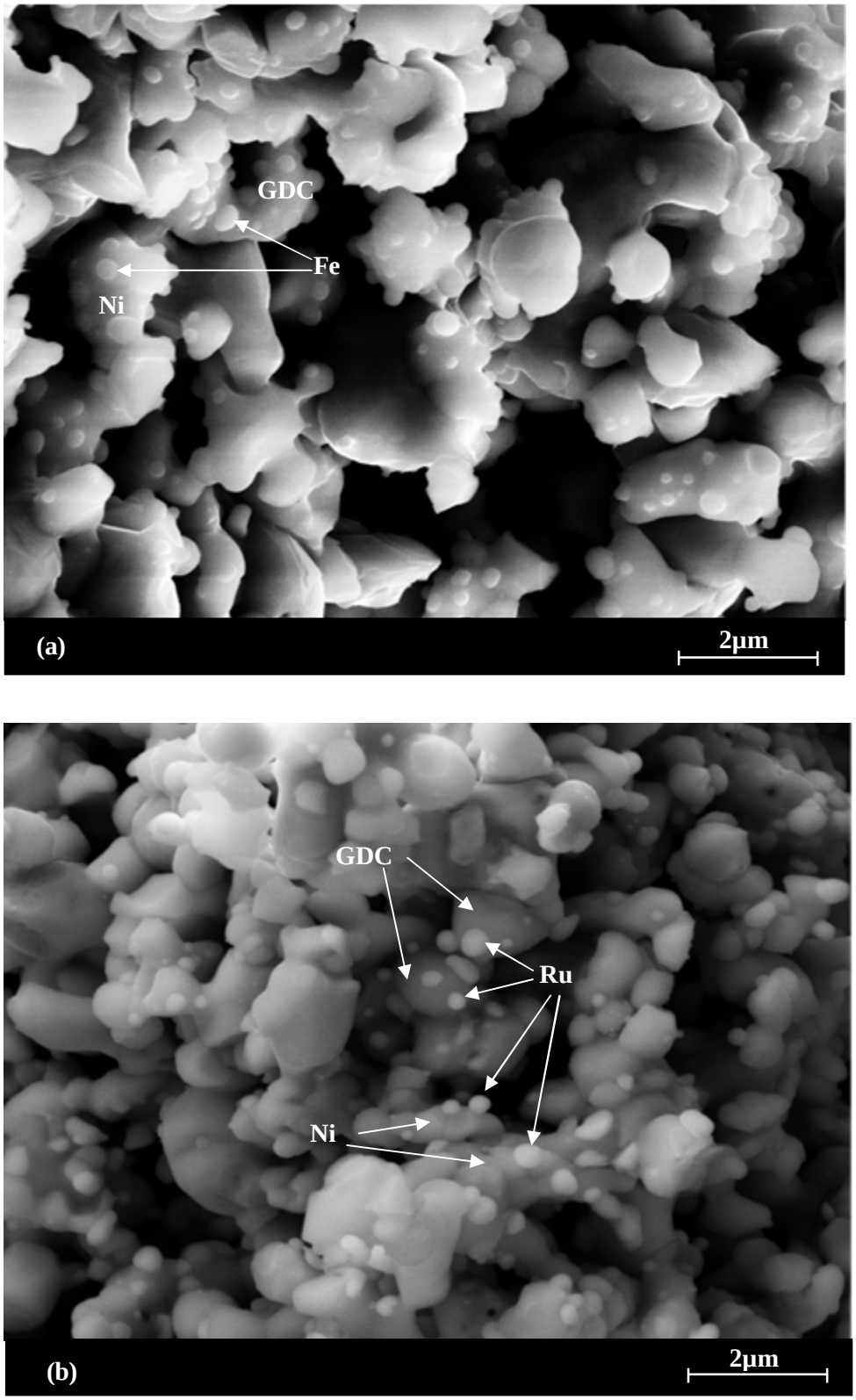

Figure 3. 5. Cross-sectional images obtained by a secondary electron detector of (a) Ni–GDC–Fe (7wt. %) and (b) Ni–GDC–Ru (7wt. %).

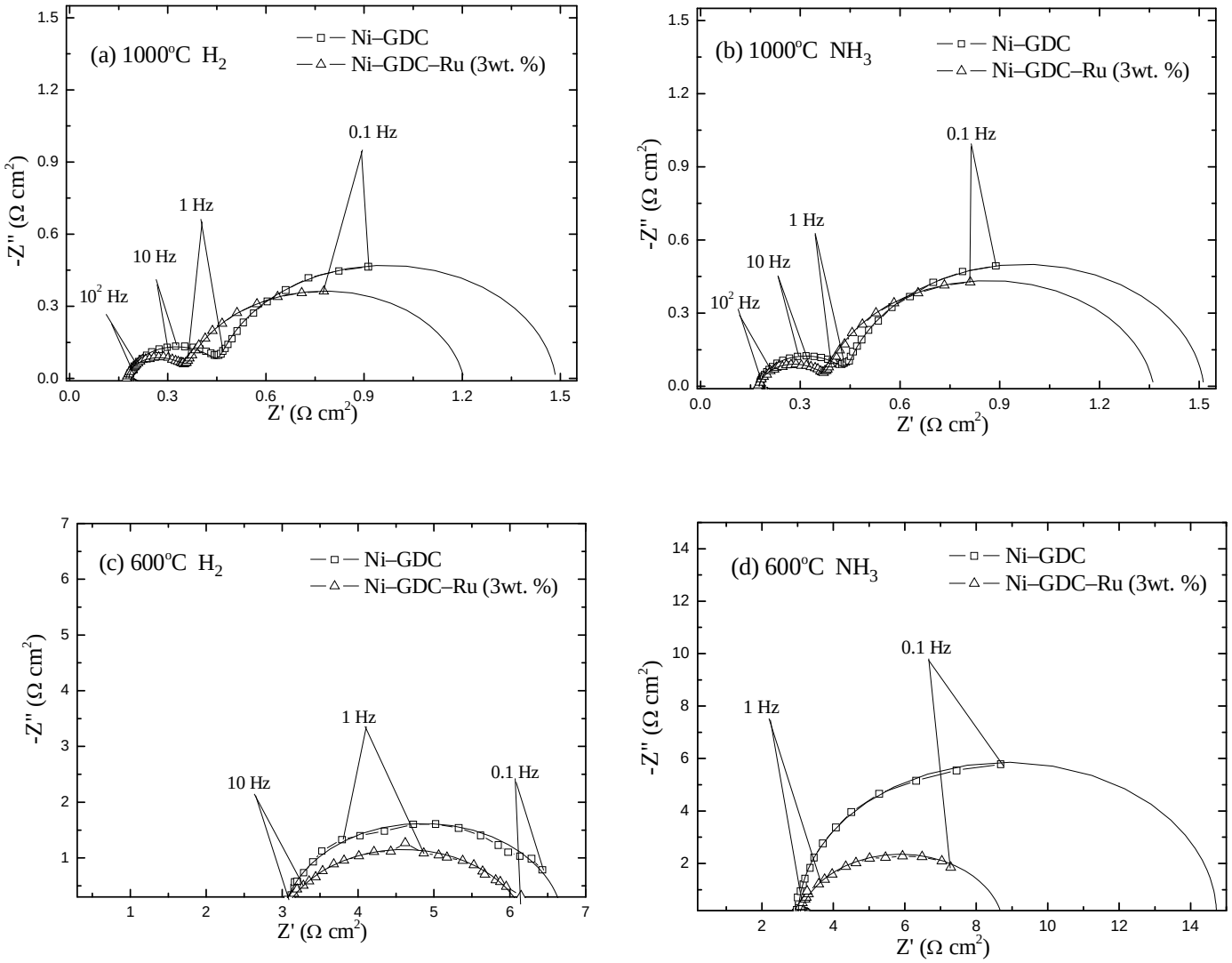

Figure 3. 6. Impedance spectra for Ni–GDC and Ni–GDC–Ru (3wt. %) anodes at 1000°C (a and b) and 600°C (c and d) in wet H_2 and NH_3 fuel. Anode gas; 60% H_2–0.5% H_2O–39.5% Ar (flow rate; 100 ml min^{-1}) and 66.7% NH_3–0.8% H_2O–32.5% Ar (flow rate; 60 ml min^{-1}). Cathode gas; O_2 (flow rate; 100 ml min^{-1}).

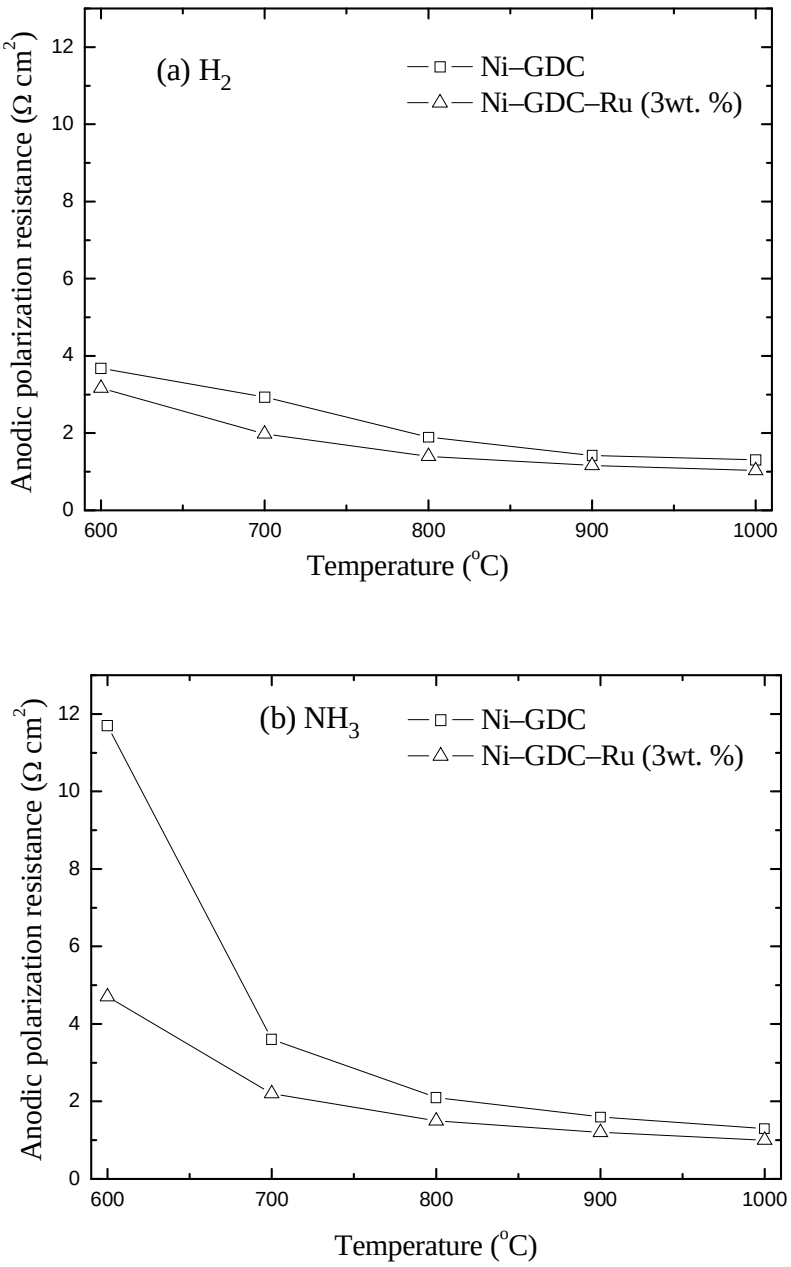

Figure 3. 7. Anodic polarization resistance for Ni–GDC and Ni–GDC–Ru (3wt. %) anode in wet (a) H_2 and (b) NH_3 at 600−1000^{o}C. Anode gas; 60% H_2–0.5% H_2O–39.5% Ar (flow rate; 100 ml min^{-1}) and 66.7% NH_3–0.8% H_2O–32.5% Ar (flow rate; 60 ml min^{-1}). Cathode gas; O_2 (flow rate; 100 ml min^{-1}).

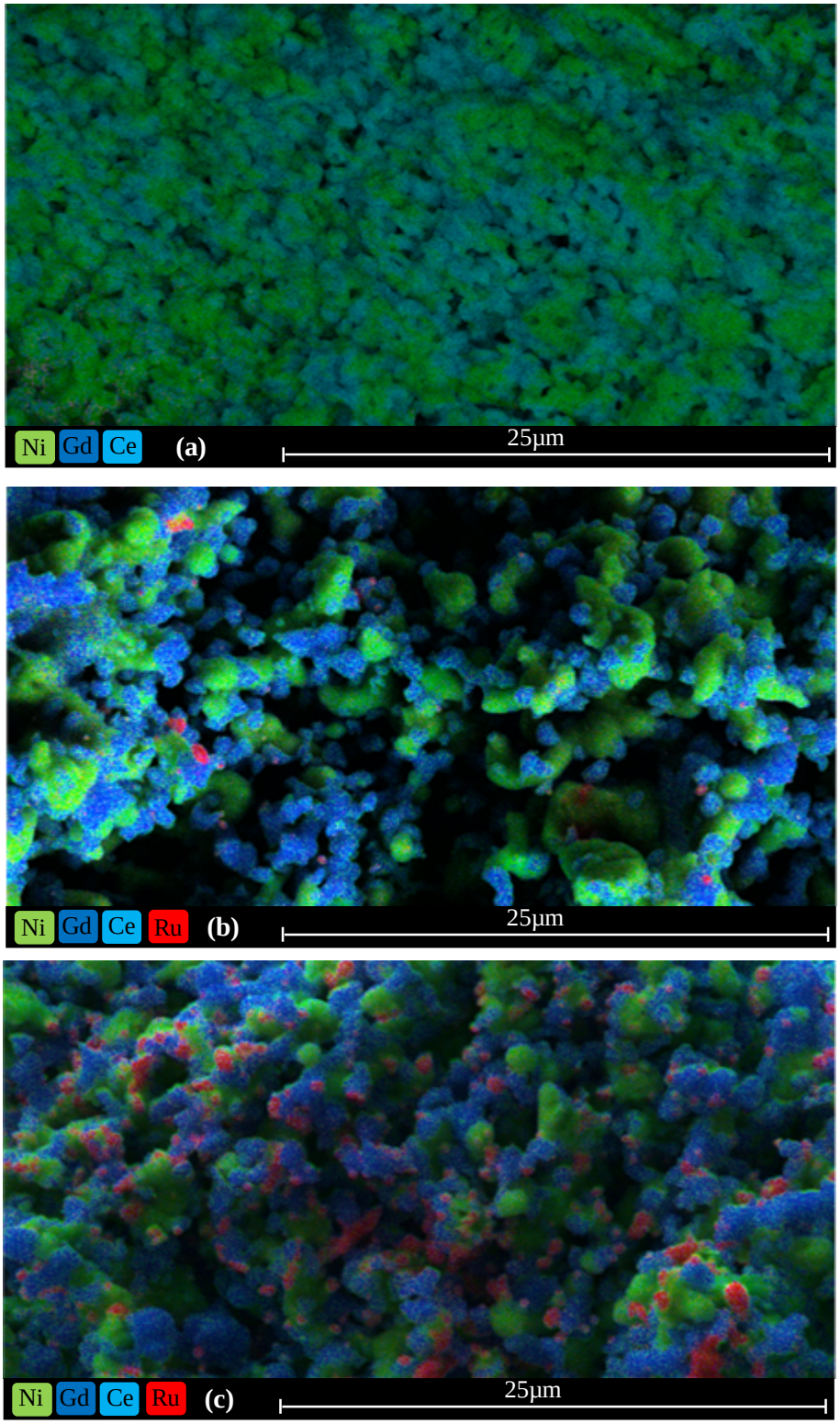

Figure 3. 8. EDS mapping for (a) Ni–GDC, (b) Ni–GDC–Ru (3wt. %), and (c) Ni–GDC–Ru (8wt. %) anodes after power generation test in H_2 and NH_3 fuels.

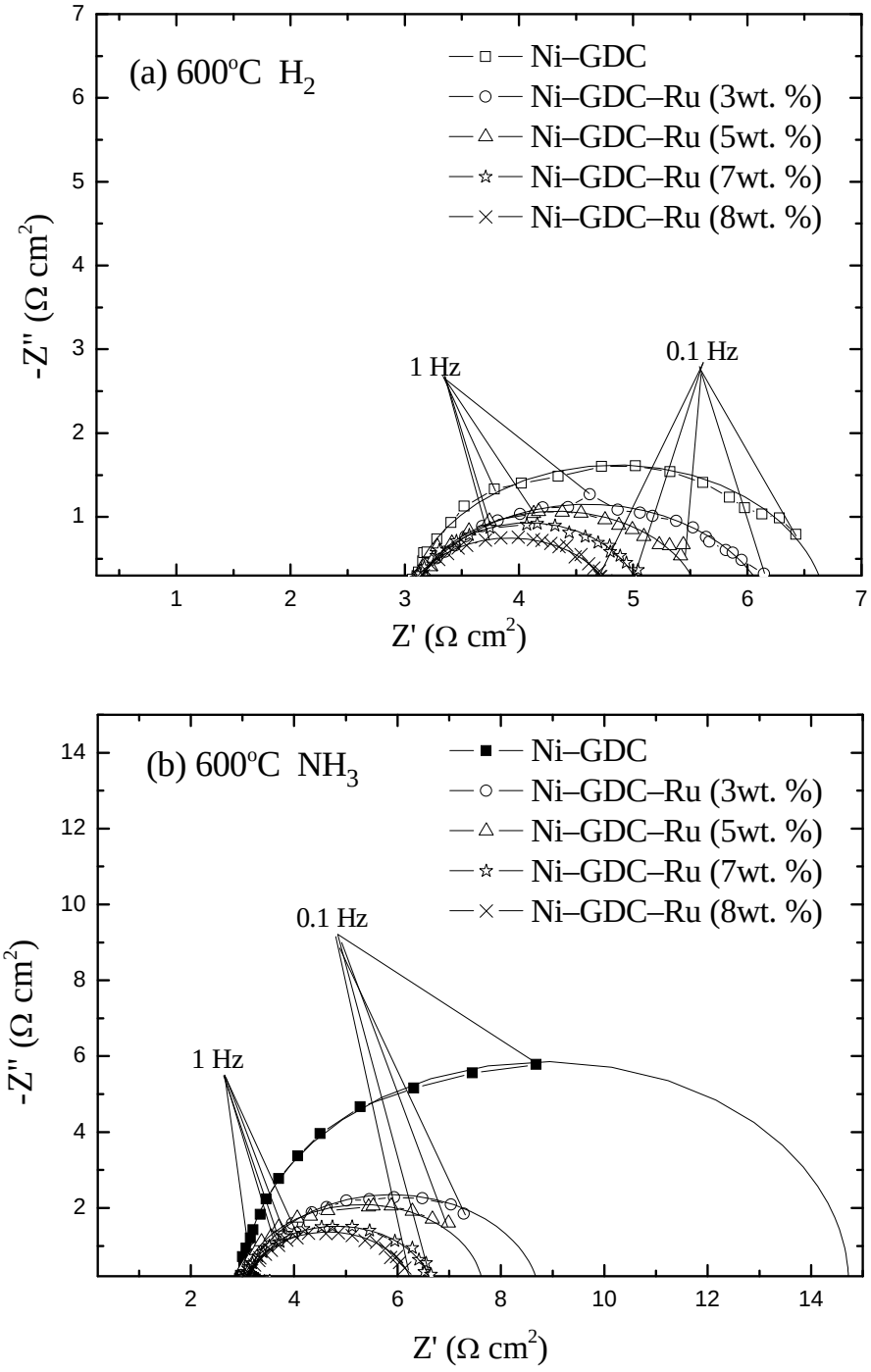

Figure 3. 9. Impedance spectra for Ni–GDC, Ni–GDC–Ru (3wt. %), Ni–GDC–Ru (5wt. %), Ni–GDC–Ru (7wt. %) and Ni–GDC–Ru (8wt. %) anodes at 600°C in wet H_2 and NH_3 fuel. Anode gas; 60% H_2–0.5% H_2O–39.5% Ar (flow rate; 100 ml min^{-1}) and 66.7% NH_3–0.8% H_2O–32.5% Ar (flow rate; 60 ml min^{-1}). Cathode gas; O_2 (flow rate; 100 ml min^{-1}).

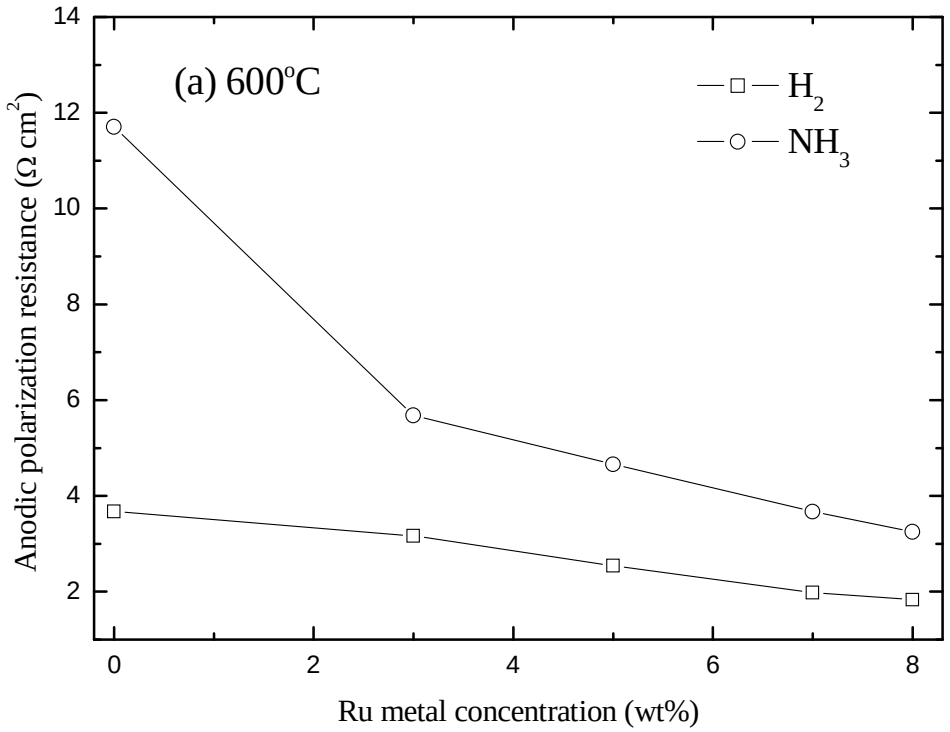

Figure 3. 10. Anodic polarization resistance as a function of ruthenium concentration for Ni–GDC, Ni–GDC–Ru (3wt. %), Ni–GDC–Ru (5wt. %), Ni–GDC–Ru (7wt. %) and Ni–GDC–Ru (8wt. %) anodes in H_2 and NH_3 fuel at 600°C.

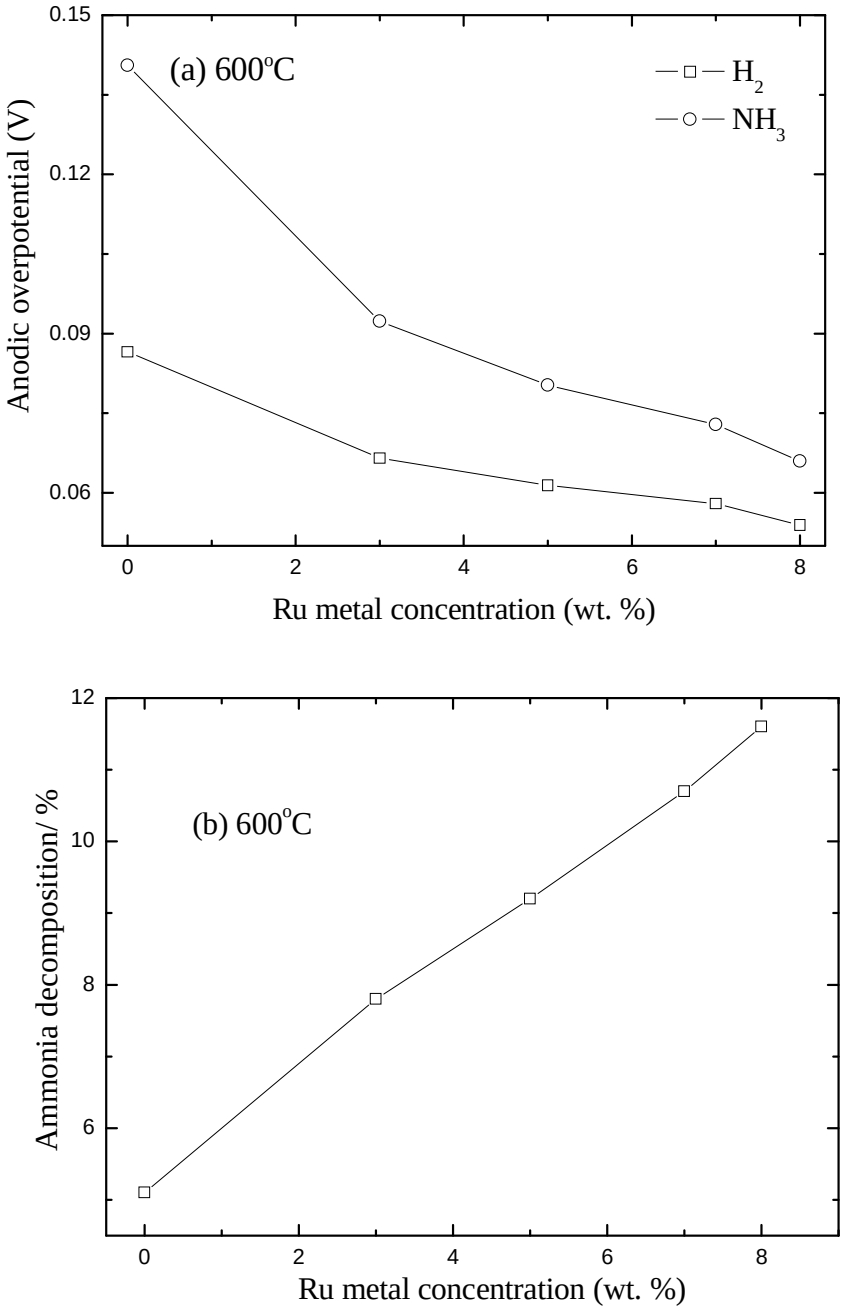

Figure 3. 11. (a) Anodic overpotenyial at current density 30 mA cm^{-2} in H_2 and NH_3 fuel and (b) ammonia decomposition as a function of ruthenium concentration at 600°C. Anode gas; 60% H_2–0.5% H_2O–39.5% Ar (flow rate; 100 ml min^{-1}) and 66.7% NH_3–0.8% H_2O–32.5% Ar (flow rate; 60 ml min^{-1}). Cathode gas; O_2 (flow rate; 100 ml min^{-1}).

Chapter 4

Electrochemical and Catalytic Properties of Ni–$BaCe_{0.75}Y_{0.25}O_{3-\delta}$ Anode for Direct Ammonia–fueled Solid Oxide Fuel Cells

4. 1. Introduction

Nowadays, human society is encountering severe environmental and energy crisis due to the excessive consumption of fossil fuels. Since 1990s a hydrogen society has been expected to suppress the greenhouse effect caused by CO_2 emission. Various kinds of fuel cells using hydrogen as a fuel have been developed. However, it is much more difficult to liquefy pure hydrogen than other fuel gases due to the low boiling point of –253^{o}C, leading to technological difficulties in transportation and storage. In view of this, many studies investigated the feasibility of alternative fuel sources including hydrogen, namely hydrogen carrier. Among them, ammonia has been receiving remarkable attention over the past decade [1].

Ammonia is one of the most produced chemical commodities in this world. It is widely used as fertilizer, refrigerant, and precursor of nitrogenous compounds. As a fuel, ammonia has many advantages such as low cost, high volumetric energy density, and ease in liquefaction (–33^{o}C at atmospheric pressure or 10 atm at ambient temperature). It is expected that the use of ammonia fuel in the following “green” energy chain could contribute to reduce CO_2 emission. Hydrogen is produced by carbon-free technologies such as photochemical water splitting and water electrolysis. Electricity needed is generated by renewable energy technologies such as solar cells, wind power, and water power stations generate electricity, etc. Hydrogen is used for ammonia synthesis by the Haber–Bosch process, which is the most matured large–scale ammonia production method. Ammonia can be easily transported to and stored in the destination field due to the mild requirement for liquefaction. Then, ammonia is

supplied to energy conversion devices such as fuel cells to generate electricity. In this energy chain, the use of hydrocarbon fuels is significantly suppressed, leading to the reduction of CO_2 emission [1]

In recent years, a great deal of effort has been made to develop direct ammonia fuel cells. For low–temperature fuel cells such as anion exchange membrane fuel cells and alkaline fuel cells, there is still a long way to go because the poisoning species generated from the electro–oxidation reaction of ammonia on anode prevent continuous power generation [2, 3]. On the other hand, solid oxide fuel cells (SOFCs), which are characterized by the high temperature operation, are considered to be suitable for the conversion of ammonia to electricity. The feasibility of direct ammonia utilization by SOFCs has been frequently studied in the literatures [4-18]. Some of the results are summarized in Table 4.1. Ammonia was supplied to SOFCs employing oxide ion–conducting electrolytes, and interesting performance was obtained at 700–1000^{o}C [4–12]. At this high temperature region, most of ammonia was decomposed into hydrogen and nitrogen over the Ni–oxide cermet anode, which catalyzed the cracking reaction efficiently. Therefore, the anode outlet gas was mainly composed of pure nitrogen, water, and remained hydrogen whereas the concentration of NO_x was negligibly small [5, 11].

Attractive results were also reported for ammonia–fueled proton–conducting SOFCs (H–SOFCs) [13–18]. Comparing with yttria–stabilized zirconia (YSZ) and gadolinium–doped ceria (GDC), proton–conductive doped barium cerates possess higher electrical conductivity at reduced temperatures (<600^{o}C) [19]. The doped barium cerates exhibit dominant proton conductivity in a wet atmosphere [20]. In this case, it is possible to avoid the generation of NO_x from ammonia and oxide ion *via* electrochemical oxidation on anode. Besides, the reaction between doped barium cerates and high-content carbon dioxide is considered to be the fatal problem that prohibits the use of doped barium cerates for hydrocarbon–fueled SOFCs. This

problem can be avoided by using ammonia as a carbon–free fuel. As is shown in Table 4.1, barium cerates doped with Eu, Nd, Gd, and (Zr+Y) in the B–site have been used for direct ammonia–fueled SOFCs. Although the cell performance at reduced temperatures was not as high as conventional SOFCs at this early stage, the promising prospect of ammonia–fueled H–SOFC has been confirmed.

Among various kinds of doped barium cerates, yttrium–doped barium cerates ($Ba(Ce,Y)O_3$, BCY) possess the highest electrical conductivity. As is the case of other doped barium cerates, BCY shows predominant proton conductivity [20]. Ni–$BaCe_{0.75}Y_{0.25}O_{3-\delta}$ (Ni–BCY25) cermet anode exhibited promising electrochemical performance for direct ammonia–fueled SOFCs [21]. In this chapter, the catalytic properties of Ni–BCY25 cermet powder for ammonia decomposition in a reactant gas simulating anode atmosphere were investigated in details. Furthermore, the influence of catalytic behavior on the electrochemical performance of Ni–BCY25 anode was also studied. Finally, an anode–supported cell was fabricated and its performance was evaluated.

4. 2. Experimental

4. 2. 1. Sample preparation

$BaCe_{0.75}Y_{0.25}O_{3-\delta}$ (BCY25) and $BaCe_{0.90}Y_{0.10}O_{3-\delta}$ (BCY10) were prepared from $Ba(NO_3)_2$ (Wako Pure Chemical Industries, Ltd.), $Ce(NO_3)_3 \cdot 6H_2O$ (Wako Pure Chemical Industries, Ltd.), and $Y(NO_3)_3 \cdot 6H_2O$ (Aldrich Inc.) by using a citric acid complex method. $Sm_{0.5}Sr_{0.5}CoO_{3-\delta}$ (SSC) was prepared from samarium, strontium, and cobalt nitrate hexahydrates (Wako Pure Chemical Industries, Ltd.) following the method in ref. 22. The formation of each phase was confirmed by X–ray diffraction analysis (XRD, Rigaku, Ultima IV X–ray diffractometer). The commercial products of $Ce_{0.9}Gd_{0.1}O_{1.95}$ (GDC, Shin–etsui

Chemical Corp.), 8 mol.% Y_2O_3–stabilized zirconia (YSZ, Tosoh Corp.), and NiO (Wako Pure Chemical Industries, Ltd.) were purchased.

NiO and BCY25 powders were mixed and ground in ethanol overnight and then dried. The mixture was calcined at 1200°C for 5 h, followed by grinding sufficiently in ethanol. The powders of NiO–GDC and NiO–YSZ were prepared in the same manner as NiO–BCY25. The volumetric content of Ni in these three samples after reduction treatment was controlled to be 50%.

4. 2. 2. Catalytic activity tests

The catalytic activity of Ni–BCY25 powder for ammonia decomposition was measured and compared with that of other SOFC anode materials, namely Ni–GDC and Ni–YSZ. The powders of Ni–BCY25, Ni–YSZ, and Ni–GDC were calcined at 1400°C for 5 h prior to catalyst tests, as was the same thermal history of anode, followed by sufficient grind. Each powder was pressed into a pellet at 30 MPa and then pulverized to 7–11 mesh. 0.3 g of the sample was set in a fixed–bed reactor, and reduced at 700°C for 2 h in 50% H_2–50% Ar under an atmospheric pressure. Subsequently, the reactant gas was supplied and the outlet gas was introduced to a sulfuric acid aqueous solution trap to eliminate residual ammonia. Then, the total flow rate of outlet gas was measured as a function of time by a film flow meter (VP 3, Horiba STEC Co., Ltd.). Ammonia conversion rate was calculated by assuming that the decomposition of ammonia only produced hydrogen and nitrogen. For comparison, the catalytic activity of Ni–GDC and Ni–YSZ was evaluated in the same way. In addition, the effect of water and hydrogen contents in reactant gas on the catalytic activity of Ni–BCY25 for ammonia decomposition was also investigated in detail. In every activity test, the space velocity of reactant gas was fixed at 14000 l kg^{-1} h^{-1}.

4. 2. 3. Cell fabrication and testing

Electrolyte–supported and anode–supported cells (hereafter abbreviated as ESC and ASC) were fabricated and tested. BCY10 was used for the electrolyte because it has much higher proton transference number (1.00, 1.00, 0.95, and 0.94 at 500, 550, 600, and 650^{o}C, respectively) than BCY25 (1.00, 0.83, 0.75, and 0.61, at 500, 550, 600, and 650^{o}C, respectively) [20]. For an ESC, BCY10 powder was uniaxially–pressed at 30 MPa into a pellet, and then the resultant pellet was isostatically pressed at 200 MPa and sintered at 1600^{o}C for 5 h. The thickness, diameter, and relative density of as–sintered BCY10 pellet were *ca*. 1 mm, 18 mm, and 97%, respectively. As the electrical conductivity of BCY25 is the highest in $BaCe_{1-x}Y_xO_{3-\delta}$ systems; this composition was adopted for the anode. NiO–BCY25 powder was mixed with 10 wt.% carbon black and polyethylene glycol (molecular weight 400, Wako Pure Chemical Industries, Ltd.) to form slurry, which was subsequently screen–printed on BCY10 pellet and calcined at 1400^{o}C for 5 h. Platinum electrode was applied on the opposite side of electrolyte pellet to serve as a cathode. The area of both electrodes was 0.28 cm^2. The configuration of ESC was Ni–BCY25|BCY10|Pt. To fabricate an ASC of Ni–BCY25|BCY10|SSC, NiO–BCY25 powder was mixed with 10 wt.% polyvinyl alcohol and co–pressed with BCY10 powder to laminate the electrolyte layer at 30 MPa, followed by isostatic–pressing at 200 MPa. The as–prepared disc was sintered at 1350^{o}C for 5 h. The thickness and diameter of electrolyte were *ca*. 0.06 mm and 18 mm, respectively. Subsequently, SSC cathode with a diameter of 10 mm was applied to the surface of BCY10 electrolyte by a screen–printing method and calcined at 1100^{o}C for 5 h.

Both of ESC and ASC were sandwiched by alumina tubes and sealed by Pyrex glass rings. Before electrochemical tests, anode was reduced in 15% H_2/85% Ar at 650^{o}C for 2 h. Humidified ammonia– and hydrogen–containing gaseous mixtures were supplied to the anode, and oxygen was used as an oxidant for the cathode. The composition of

hydrogen–containing gas was determined by assuming that ammonia in the ammonia–containing gas decomposed to nitrogen and hydrogen completely. For example, the ammonia–containing gas with a composition of 42.9% NH_3-0.8% H_2O-54.5% is converted to hydrogen–containing gas with a composition of 45.0% H_2–1.0% H_2O–54.0% N_2. The details of anode gas composition for ESC and ASC are explained in the following section. The cathode gas was pure oxygen with a flow rate of 100 ml min^{-1}. For an ESC, current–voltage (*I–V*) characteristics and impedance spectra under different conditions were measured by the CellTest system (Solartron Analytical, UK, potentiostat/galvanostat 1470E and frequency response analyzer 1455). In addition, the anode off–gas was analyzed by a mass spectrometer (OmniStar GSD 320, Pfeiffer Vacuum AG) in order to monitor the change in gas composition caused by the galvanostatic operation. In the case of ASC, *I–V* characteristics of the cell fueled with ammonia and hydrogen were recorded at 550–650^oC.

4. 3. Results and discussion

The catalytic activity of Ni–BCY25 for ammonia decomposition was compared with Ni–GDC and Ni–YSZ as shown in Fig. 4. 1. Diluted ammonia (42.9% NH_3–57.1% Ar; total flow rate: 70 ml min^{-1}) was supplied to the catalyst. For every catalyst, the activity for ammonia decomposition increased significantly with rising temperature. At each temperature, the Ni–BCY25 cermet exhibited the highest activity; a high ammonia conversion rate of 98.6% was obtained at 600^oC.

The anode gas for ammonia–fueled SOFC usually consists of ammonia, water, nitrogen, and hydrogen. It was confirmed in the literature that nitrogen concentration would not affect ammonia decomposition over Ni catalyst but hydrogen has a poisoning effect [23]. On the other hand, the effect of water concentration on the activity for ammonia decomposition has not been investigated yet. In this study, therefore, the influence of hydrogen and water

concentrations on the catalytic activity of anode materials was studied.

A number of studies suggested that the presence of hydrogen in the reactant gas exhibited a poisoning effect on ammonia decomposition over Ni and Ru catalysts because hydrogen would occupy the active reaction sites on catalyst surface [23-27]. The reaction rate of ammonia, r_{NH_3}, ml min^{-1}, can be described by the following equation:

$$r_{NH_3} = -\frac{dP_{NH_3}}{dt} = kP_{NH_3}{}^{\alpha} P_{H_2}{}^{\beta} \qquad (4\text{–}1)$$

where P_{NH_3} and P_{H_2} are partial pressure of ammonia and hydrogen, Pa, respectively. *k*, α, and β are constants [23]. In this work, the reaction order of hydrogen, β, was used to evaluate the resistance of catalyst to the hydrogen poisoning effect. In order to obtain β, the reactant gas with fixed P_{NH_3} and different P_{H_2} was supplied to Ni–BCY25 and Ni–GDC in order to measure the reaction rate of ammonia was measured as a function of P_{H_2} at 450–550^{o}C. Similar experiment was carried out on Ni–YSZ at 500–550^{o}C because of its low catalytic activity. The P_{H_2} dependence of r_{NH_3} for Ni–BCY25 and Ni–GDC at 450^{o}C is shown in Fig. 4. 2(a). With increasing P_{H_2}, the rate, r_{NH_3}, decreased apparently at 450^{o}C regardless of catalyst. The constant of β for each catalyst was calculated according to equation (4–1) and plotted as a function of temperature in Fig. 4. 2(b). Minus sign indicates that the existence of hydrogen in the reactant gas retards the reaction rate. The β value of Ni–BCY25 was much closer to zero than Ni–GDC and Ni–YSZ, representing superior resistance to hydrogen poisoning effect. Moreover, Fig. 4. 2(b) shows that the poisoning effect of hydrogen for three catalysts was significantly relieved at higher temperatures, which would be resulted from the

weaker adsorption of hydrogen on the active reaction sites.

The influence of water content in the reactant gas on ammonia decomposition over Ni–BCY25 is shown in Fig. 4. 3. The ammonia conversion over Ni–BCY25 decreased significantly even with an addition of 0.8% water. The poisoning effect of water for Ni–BCY25 was compared with Ni–GDC and Ni–YSZ in Fig. 4. 4. The ammonia conversion over Ni–BCY25 at 600^{o}C dropped sharply from 98.6% to 55.0% when water 0.8% was added, and subsequently decreased gradually with increasing water concentration. Similar tendency was observed for Ni–GDC and Ni–YSZ but the extent of drop in ammonia conversion was much smaller. It was reported that the dissociative adsorption of water occurs readily on the surface of BCY25 [28]. Thus, the resultant species such as hydroxide group and proton might occupy active reaction sites at the interface between Ni and BCY25, resulting in the strong water poisoning effect.

Then, the influence of catalytic properties of Ni–BCY25 for ammonia decomposition on electrochemical performance was studied by using the ESC (Ni–BCY25|BCY10|Pt). Ammonia–containing and hydrogen–containing gases were supplied to the Ni–BCY25 anode. Two kinds of anode gases should have the same gas composition if ammonia decomposes to nitrogen and hydrogen completely. Since BCY10 electrolyte possesses a proton transference number close to unity at the temperature range of 500–650^{o}C, the influence of oxide ion conduction is negligible in this work. If ammonia is directly converted to electricity, the anode reaction is expressed as follow:

$$2NH_3 \rightarrow 6H^+ + N_2 + 6e^- \qquad (4\text{–}2)$$

The total reaction in the cell can be written as follow.

$$4NH_3+3O_2 \rightarrow 2N_2 +6H_2O \quad (4–3)$$

The hydrogen generated from ammonia decomposition also serves as the fuel. The reaction is described as

$$H_2 \rightarrow 2H^+ +2e^- \quad (4–4)$$

As a result, the total electrochemical reaction is as follow:

$$2H_2 +O_2 \rightarrow 2H_2O \quad (4–5)$$

According to thermodynamics and Nernst equation, the theoretical open circuit voltages (OCVs) calculated from reaction (4–3) is much higher than that from reaction (4–5), as can be seen in Fig. 4. 5. The experimental OCVs of ESC fueled with two kinds of anode gases were compared with the theoretical ones. When the anode was exposed to the H_2–containing gas, the OCV was slightly lower than the theoretical one and decreased linearly with a rise in temperature. This tendency agreed well with thermodynamics. The experimental OCV for NH_3–containing anode gas was even lower than that for H_2–containing one. Moreover, the gap between the OCVs for H_2–containing and NH_3–containing anode gases was enlarged apparently at lower temperatures. Analogous tendency was also found for Ni–YSZ and Ni–$Ce_{0.8}Sm_{0.2}O_{1.9}$ anodes [21]. It is reasonable to consider that the hydrogen generated from ammonia decomposition served as the main fuel at the anode. The catalytic activity of Ni–BCY25 anode for ammonia decomposition deteriorated at lower temperatures, leading to an increase in the deviation of experimental OCVs for the two kinds of anode gases.

Figure 4. 6 shows *I–V* characteristics of the ESC with Ni–BCY25 anode at 550–650^{o}C. Since the cathode gas composition was fixed, the difference in *I–V* curves reflects the response of anode performance to different anode gases. At each temperature, the cell performance was higher in the H_2–containing fuel than in NH_3–containing one. Moreover, the difference in cell performance for the H_2–containing and NH_3–containing anode gases enlarged apparently with decreasing temperature. The negative effect of temperature decline on catalytic activity of Ni–BCY25 anode for ammonia decomposition was responsible for this phenomenon.

The influence of water content on the cell performance is shown in Figs. 4. 7 and 4. 8. The OCV decreased slightly with increasing water content in anode gas from 0.4 % to 2.9% while the current density at low terminal voltage region was apparently raised. Figure 4. 8 shows that with increasing humidity of anode gas, the ohmic resistance, which was dominant for cell performance, was reduced significantly; the polarization resistance was almost stable. As a result, the poisoning effect of water for ammonia decomposition described in Fig. 4. 4 did not apparently degrade the cell performance. The proton conductivity of yttrium–doped barium cerate in the presence of water originates from the incorporation of $OH_{O}^{\bullet}$ (according to Kröger-Vink denotation) at oxygen vacancies ($V_O^{\bullet\bullet}$). The reaction is expressed as follows.

$$H_2O + V_O^{\bullet\bullet} + O_O^{\times} \rightarrow 2OH_O^{\bullet} \qquad (4\text{–}6)$$

The resultant proton localized on the lattice oxygen can hop to neighboring oxygen site to exhibit proton conductivity. Increasing humidity raises the concentration of $OH_{O}^{\bullet}$, and thus elevates the proton conductivity.

After experiments in Figs. 4. 7 and 4. 8, the cell was discharged with a supply of ammonia–containing anode gas at current densities of 0.7 A cm^{-2}, 1.1 A cm^{-2}, and 1.4 A cm^{-2}

for 600 s, as shown in Fig. 4. 9(a). The changes of H_2, N_2, and NO_x (NO, NO_2, and N_2O) signals in the anode outlet gas under polarization were monitored by the mass spectrometer. Figure 4. 9(b) shows that when the discharge started, the mass signal of H_2 decreased rapidly and then kept nearly stable for *ca*. 400 s. After the interruption of current, the mass signal of H_2 increased to the original level before galvanostatic operation. It is noted that the decrement of H_2 signal during discharge became prominent by increasing current loading. Simultaneously, the mass signal of N_2 increased at the beginning of current loading (see Fig. 4. 9(c)). The increment of N_2 signal indicated the promotion effect of anodic current for ammonia decomposition over Ni–BCY25 anode. This is reasonable because hydrogen is consumed under polarization conditions, which has a poisoning effect for ammonia decomposition as is observed in Fig. 4. 2. Throughout this experiment, NO_x (NO, N_2O, and NO_2) species was scarcely detected (<20 ppm). However, considering the ohmic resistance was dominant in this study, the anode polarization was rather small. Therefore, the condition of NO_x formation over anode needs further investigation.

An anode–supported cell, ASC (Ni–BCY25|BCY10|SSC), was fabricated. The cell performance at 550–650^{o}C is shown in Fig. 4. 10. At each temperature, the OCV and cell performance under NH_3–fueled condition was closer to that under H_2–fueled one comparing with the case of ESC. This is because the ASC is composed of more amount of anode catalyst than the ESC, leading to larger gas hourly space velocity. Therefore, ammonia decomposition proceeded sufficiently for ASC. The maximum powder density achieved was 216 mW cm^{-2} and 165 mW cm^{-2} at 650^{o}C and 600^{o}C, respectively. It is expected that the cell performance could be further improved by optimizing the fabrication parameters of cell and electrodes such as using thinner electrolyte film.

4. 4. Conclusions

In this work, the catalytic activity of Ni–BCY25, Ni–GDC, and Ni–YSZ for ammonia decomposition was investigated. It was found that Ni–BCY25 was more active for ammonia decomposition and more resistant to the hydrogen poisoning effect than Ni–GDC and Ni–YSZ. However, ammonia decomposition over Ni–BCY25 was significantly suppressed by water. The electrochemical properties of Ni–BCY25 anode were also investigated with supply of ammonia– and hydrogen–fueled conditions. An anode–supported single cell, Ni–BCY25|BCY10|SSC, demonstrated attractive performance was obtained. Based on these results, it was concluded that Ni–BCY25 anode possessed excellent electrochemical and catalytic activities, and thus is promising for direct ammonia-fueled SOFCs.

References

[1] L. Rong, J. Irvine, S. Tao, *Int. J. Hydrogen Energy*, **37**, 1482–1494 (2012).

[2] K. Endo, Y. Katayama, T. Miura, *Electrochimi. Acta.*, **49**, 1635–1638 (2004).

[3] J. Yang, H. Muroyama, T. Matsui, K. Eguchi, *J. Power Sources*, **245**, 277–282 (2014).

[4] A. Wojcik, H. Middleton, I. Damopoulos, J. Van herle, *J. Power Sources*, **118**, 342–348 (2003).

[5] G. Fournier, I. Cumming, K. Hellgardt, *J. Power Sources*, **162**, 198–206 (2006).

[6] Q. Ma, R. Peng, L. Tian, G. Meng, *Electrochem. Commun.*, **8**, 1791–1795 (2006).

[7] L. Zhang, Y. Cong, W. Yang, L. Lin, *Chinese J. Catal.*, **28**, 749–751 (2007).

[8] Q. Ma, J. Ma, S. Zhou, R. Yan, J. Gao, G. Meng, *J. Power Sources*, **164**, 86–89 (2007).

[9] G. Meng, C. Jiang, J. Ma, Q. Ma, X. Liu, *J. Power Sources*, **173**, 189–193 (2007).

[10] N. Dekker, G. Rietveld, *J. Fuel Cell Sci. Technol.*, **3**, 499–502 (2006).

[11] L. Liu, K. Sun, X. Wu, X. Li, M. Zhang, N. Zhang, X. Zhou, *Int. J. Hydrogen Energy*, **37**, 10857–10865 (2012).

[12] W. Akimoto, T. Fujimoto, M. Saito, M. Inaba, H. Yoshida, T. Inagaki, *Solid State Ionics*,

256, 1–4 (2014).

[13] L. Pelletier, A. McFarlan, N. Maffei, *J. Power Sources*, **145**, 262–265 (2005).

[14] N. Maffei, L. Pelletier, J. Charland, A. McFarlan, J. Power Sources, **162**, 165–167 (2006).

[15] Q. Ma, R. Peng, Y. Lin, J. Gao, G. Meng, *J. Power Sources*, **161**, 95–98 (2006).

[16] K. Xie, Q. Ma, B. Lin, Y. Jiang, J. Guo, X. Liu, G. Meng, J. Power Sources, 170, 38–41 (2007).

[17] L. Zhang, W. Yang, *J. Power Sources*, **179**, 92–95 (2008).

[18] Y. Lin, R. Ran, Y. Guo, W. Zhou, R. Cai, J. Wang, Z. Shao, *Int. J. Hydrogen Energy*, **35**, 2637–2642 (2010).

[19] T. Hibino, A. Hashimoto, M. Suzuki, M. Sano, *J. Phys. Chem*., **B105**, 11399–11401 (2001).

[20] W. Suksamai, I. Metcalfe, *Solid State Ionics*, **178**, 627–634 (2007).

[21] J. Yang, T. Akagi, T. Okanishi, H. Muroyama, T. Matsui, K. Eguchi, *Fuel cells*, **15**, 390 (2015).

[22] M. Koyama, C. Wen, T. Masuyama, J. Otomo, H. Fukunag, K. Yamada, K. Eguchi, H. Takahashi, *J. Electrochem. Soc*., **148**, A795–A801 (2001).

[23] J. Zhang, H. Xu, W. Li, *Appl. Catal. A: Gen*., **296**, 257-267 (2005).

[24] K. Okura, T. Okanishi, H. Muroyama, T. Matsui, K. Eguchi, *Appl. Catal. A: Gen.*, **505**, 77-85 (2015). .

[25] S. Yin, B. Xu, X. Zhou, C. Au, *Appl. Catal. A: Gen.*, **277**, 1–9 (2004).

[26] F. Hayashi, Y. Toda, Y. Kanie, M. Kitano, Y. Inoue, T. Yokoyama, M. Hara, H. Hosono, *Chem. Sci*., **4**, 3124–3130 (2013).

[27] M. Bradford, P. Fanning, M, Vannice, *J. Catal*., **172**, 479–484 (1997).

[28] A. Kruth, J, Irvine, *Solid State Ionics*, **162-163**, 83-9 (2003).

Table 4.1

Publication list of fuel cell performance using ammonia–containing fuel.

Electrolyte	Cathode	Oxidant	Anode	Fuel	Temperature (^oC)	Max Power density ($mW\ cm^{-2}$)	Ref.
8 mol.% Y_2O_3-ZrO_2 (YSZ)	Pt	O_2	Pt	7% NH_3/93% N_2	1000	130	4
YSZ	Ag	Air	Ni–YSZ	NH_3	800	60	5
$Ce_{0.8}Sm_{0.2}O_{1.9}$	$Sm_{0.5}Sr_{0.5}CoO_{3-\delta}$–$Ce_{0.8}Sm_{0.2}O_{1.9}$	O_2	Ni–$Ce_{0.8}Sm_{0.2}O_{1.9}$	NH_3	750	250	6
YSZ	$La_{0.67}Sr_{0.33}MnO_{3+\delta}$–YSZ	Air	Ni–YSZ	NH_3	800	200	7
YSZ	YSZ–$La_{0.5}Sr_{0.5}MnO_{3+\delta}$	Air	Ni–YSZ	97% NH_3/3% H_2O	750	299	8
$Ce_{0.8}Sm_{0.2}O_{1.9}$	$Ba_{0.5}Sr_{0.5}Co_{0.8}Fe_{0.2}O_{3-\delta}$	Air	Ni–$Ce_{0.8}Sm_{0.2}O_{1.9}$	NH_3	650	1190	9
YSZ	$La_{0.6}Sr_{0.4}Co_{0.2}Fe_{0.8}O_{3-\delta}$	Air	Ni–YSZ	NH_3	700	400	10
$Sc_{0.1}Zr_{0.9}O_{1.95}$	LSM–YSZ	Air	Fe/Ni–YSZ	NH_3	800	1150	11
$La_{0.90}Sr_{0.10}Ga_{0.80}Mg_{0.20}O_{2.85}$	$Sm_{0.5}Sr_{0.5}CoO_{3-\delta}$	Air	Fe–$Ce_{0.8}Sm_{0.2}O_{1.9}$	NH_3	900	390	12
$BaCe_{0.8}Gd_{0.19}Pr_{0.01}O_{3-\delta}$	Pt	Air	Pt	NH_3	700	35	13
$BaCe_{0.85}Eu_{0.15}O_{3-\delta}$	Pt	Air	Pt	NH_3	700	38	14
$BaCe_{0.8}Gd_{0.2}O_{3-\delta}$	$La_{0.5}Sr_{0.5}CoO_{3-\delta}$–$BaCe_{0.8}Gd_{0.2}O_{3-\delta}$	97% O_2/3% H_2O	Ni–$BaCe_{0.8}Gd_{0.2}O_{3-\delta}$	NH_3	750	380	15
$BaCe_{0.9}Nd_{0.1}O_{3-\delta}$	$La_{0.5}Sr_{0.5}CoO_{3-\delta}$– $BaCe_{0.9}Nd_{0.1}O_{3-\delta}$	Air	Ni–$BaCe_{0.9}Nd_{0.1}O_{3-\delta}$	NH_3	700	315	16
$BaCe_{0.8}Gd_{0.2}O_{3-\delta}$	$Ba_{0.5}Sr_{0.5}Co_{0.8}Fe_{0.2}O_{3-\delta}$–$Ce_{0.8}Gd_{0.2}O_{1.9}$	O_2	Ni–$Ce_{0.8}Gd_{0.2}O_{1.9}$	NH_3	600	147	17
$BaZr_{0.1}Ce_{0.7}Y_{0.2}O_{3-\delta}$	$Ba_{0.5}Sr_{0.5}Co_{0.8}Fe_{0.2}O_{3-\delta}$	Air	Ni–$BaZr_{0.1}Ce_{0.7}Y_{0.2}O_{3-\delta}$	NH_3	600	190	18

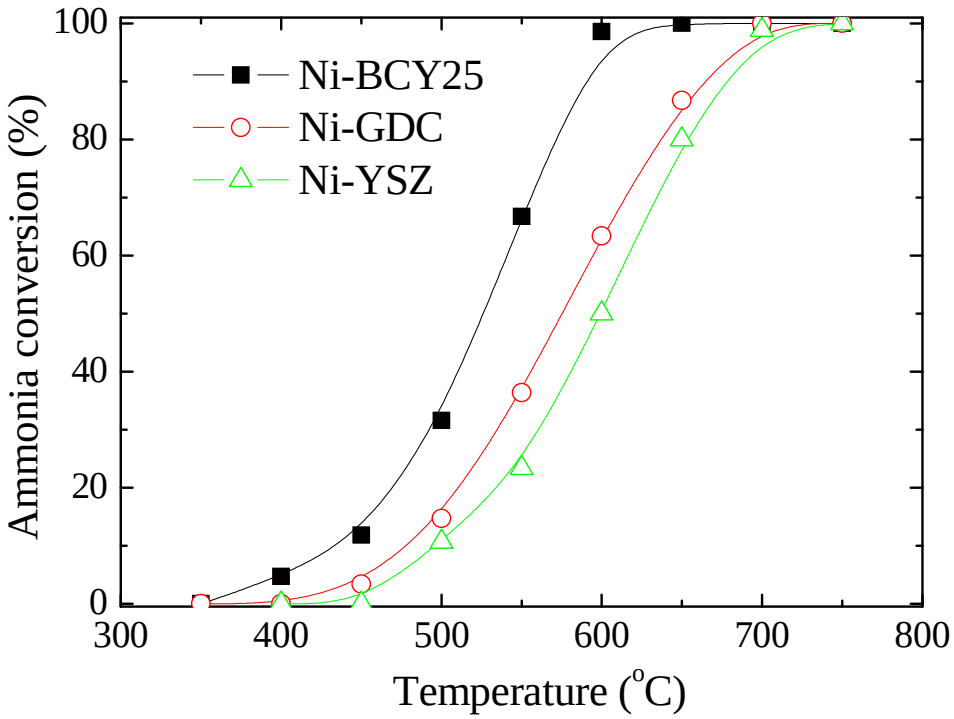

Figure 4. 1. Ammonia conversion over Ni–BCY25, Ni–GDC, and Ni–YSZ with reactant gas of 42.9% NH_3–57.1% Ar; gas space velocity: 14000 l kg^{-1} h^{-1}.

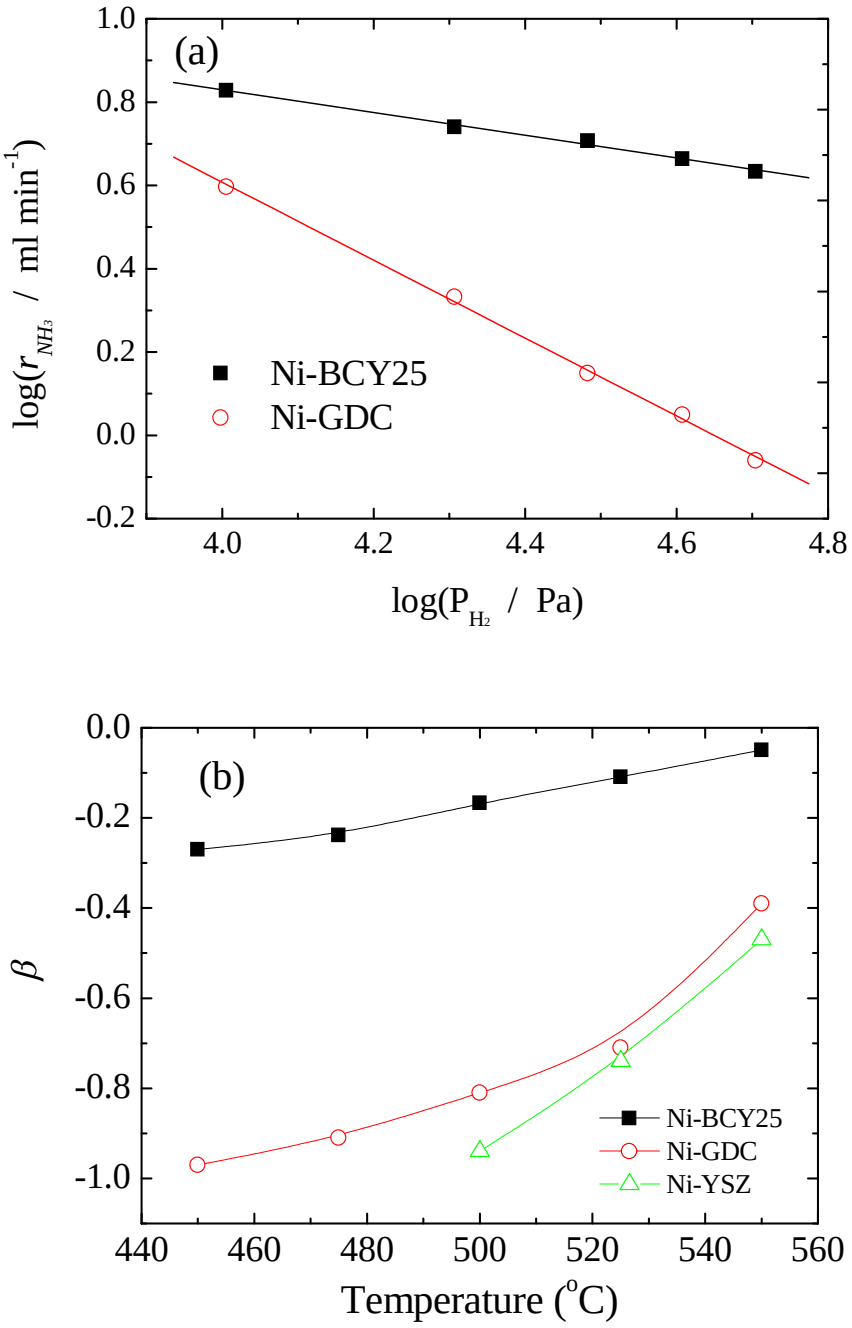

Figure 4. 2. (a) Ammonia reaction rate (r_{NH_3}) for Ni–BCY25 and Ni–GDC as a function of hydrogen partial pressure (P_{H_2}) at 450°C; (b) β value of Ni–BCY25, Ni–GDC, and Ni–YSZ as a function of temperature; reactant gas: 50.0 % NH_3–x% H_2–(50.0–x)% Ar; gas space velocity: 14000 l kg^{-1} h^{-1}.

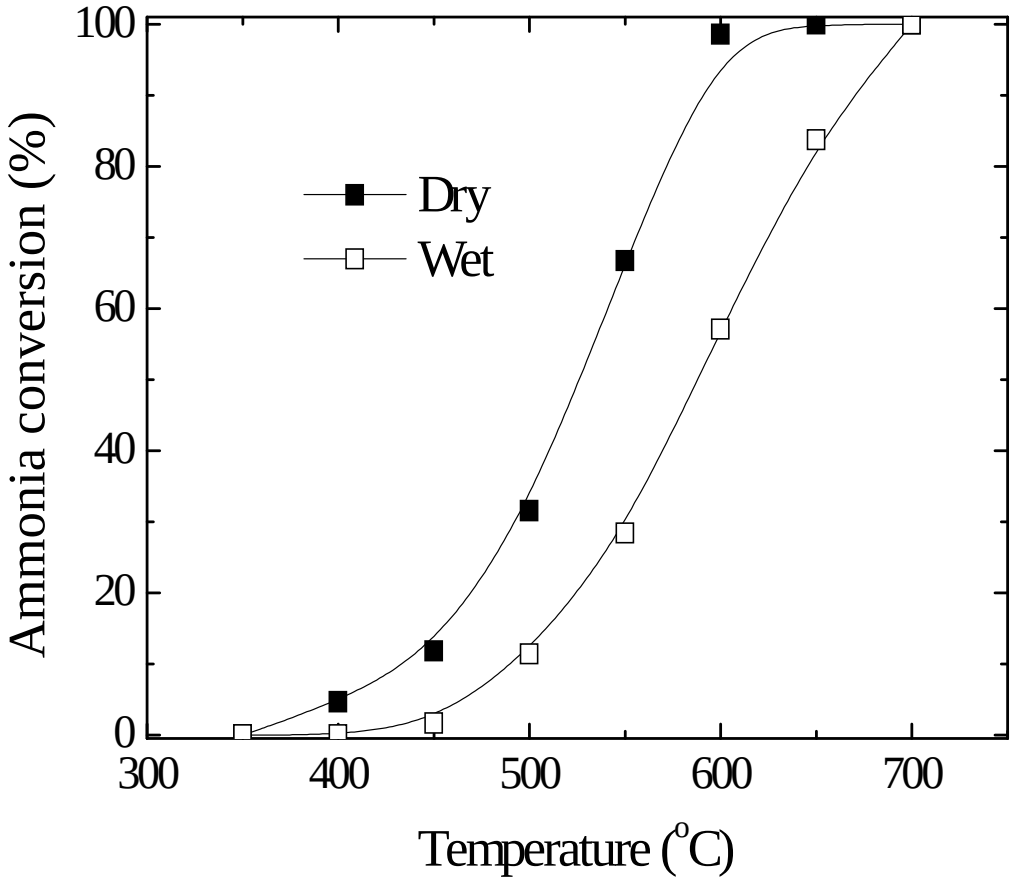

Figure 4. 3. Ammonia conversion over Ni–BCY25 with reactant gases of 42.9% NH_3–57.1% Ar (dry) and 42.9% NH_3–0.8% H_2O–54.5% Ar (wet); gas space velocity: 14000 l kg^{-1} h^{-1}.

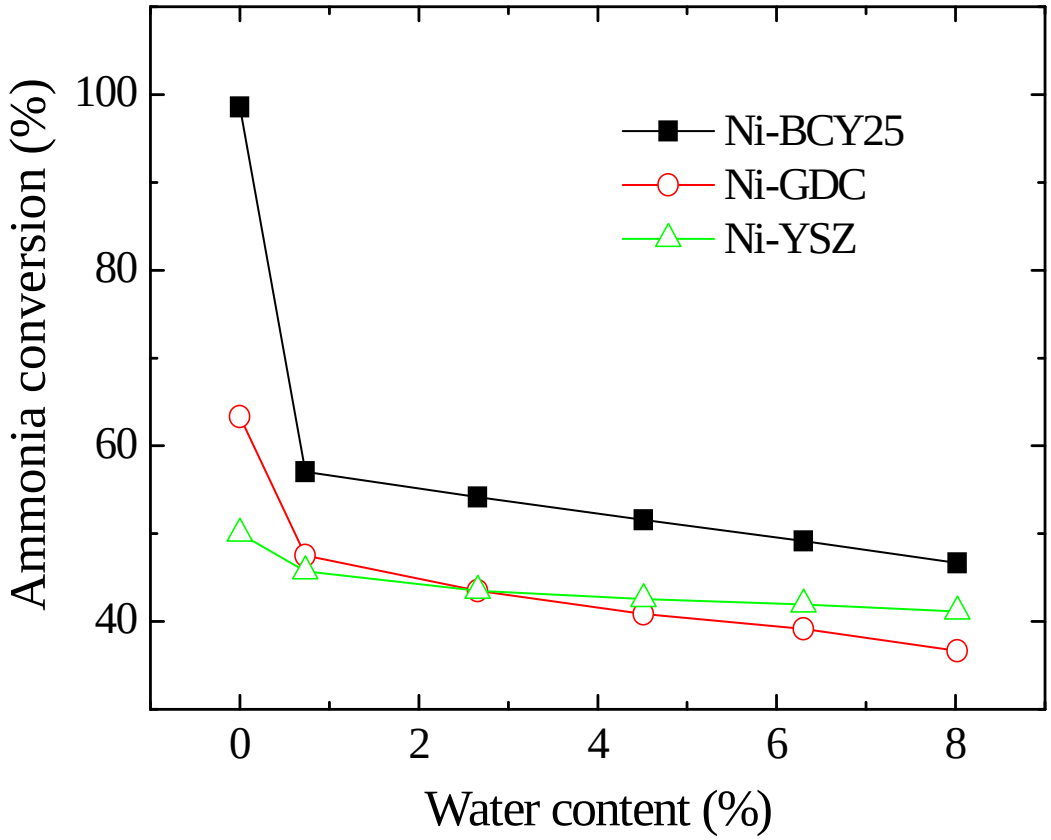

Figure 4. 4. Ammonia conversion over Ni–BCY25, Ni–GDC, and Ni–YSZ as a function of water concentration at 600°C; reactant gas: 42.9% NH_3–*x*% H_2O–(57.1–*x*)% Ar; gas space velocity: 14000 l kg^{-1} h^{-1}.

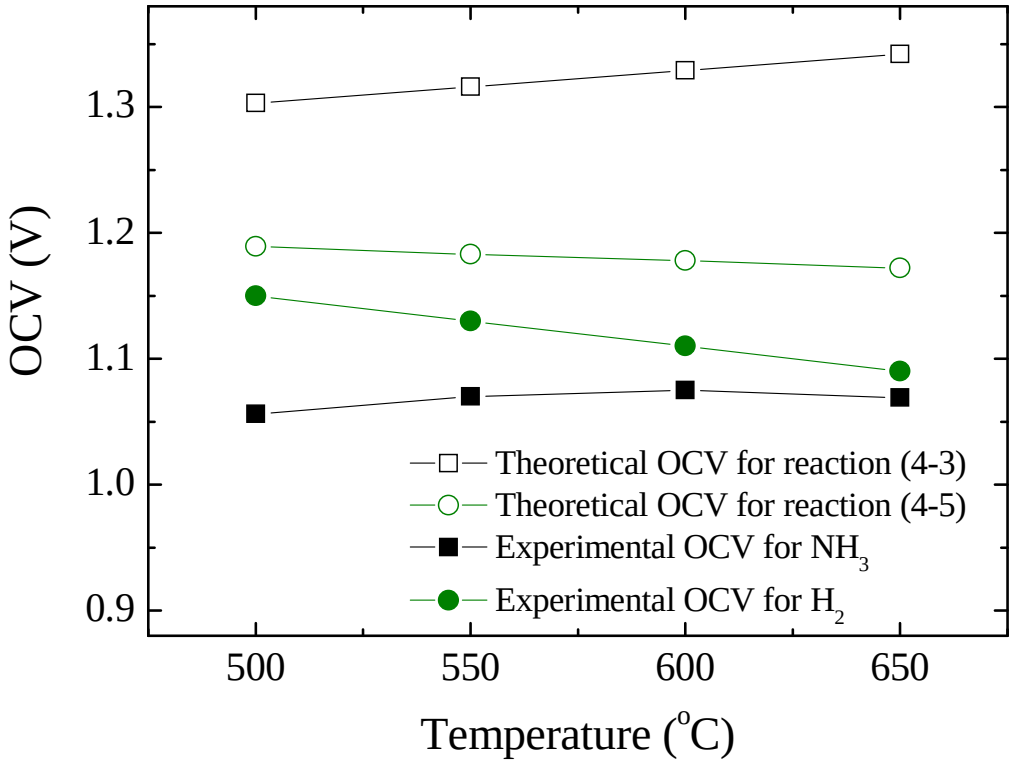

Figure 4. 5. Theoretical and experimental OCVs for ESC (Ni–BCY25|BCY10|Pt) fueled with 45.0% H_2–1.0% H_2O–54.0% N_2 and 42.9% NH_3–1.4% H_2O–55.7% N_2 at 500–700°C.

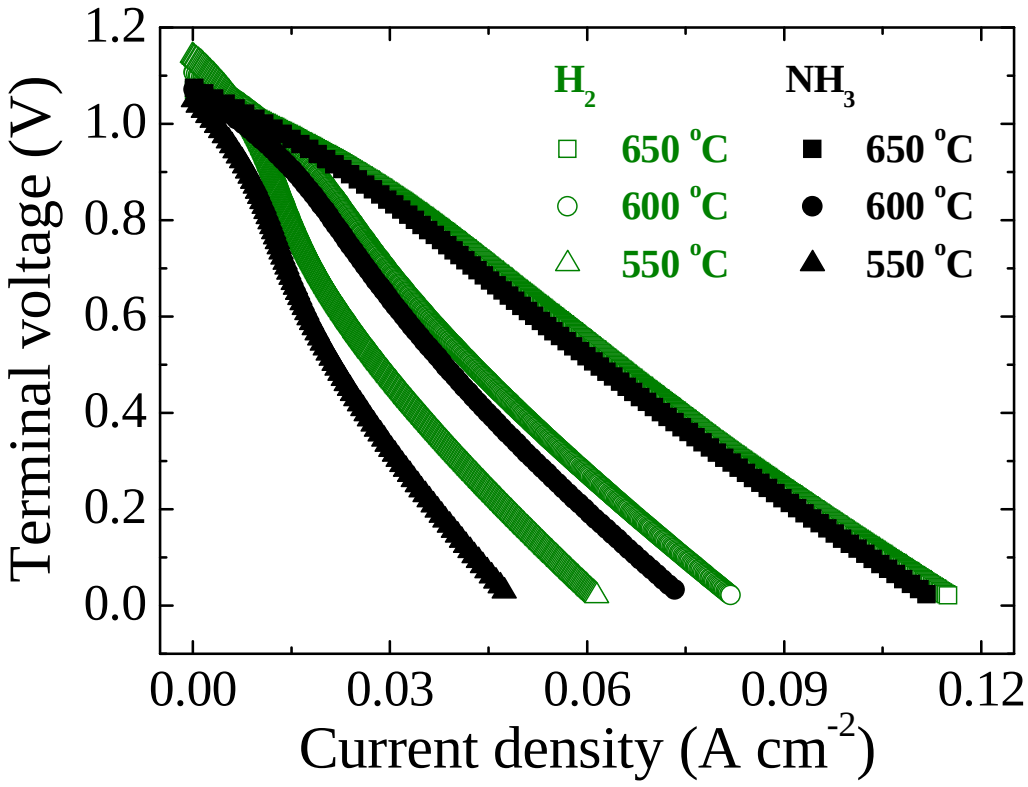

Figure 4. 6. *I–V* curves of ESC (Ni–BCY25|BCY10|Pt) fueled with 45.0% H_2–1.0% H_2O–54.0% N_2 and 42.9% NH_3–1.4% H_2O–55.7% N_2; cathode gas: O_2.

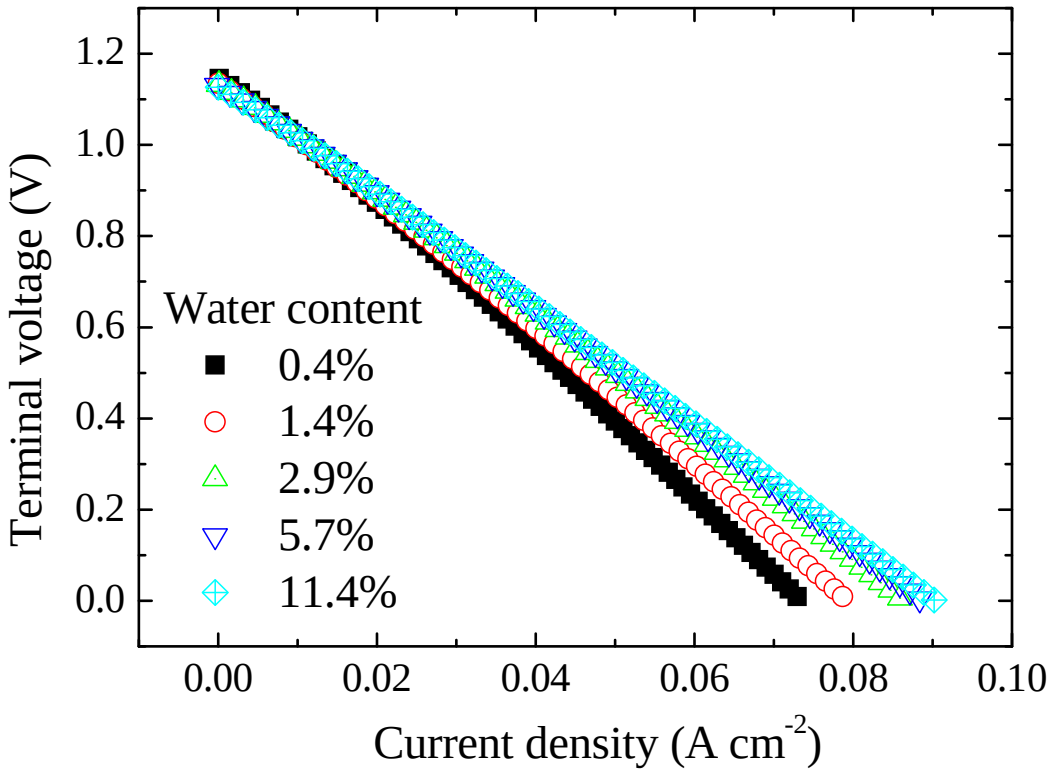

Figure 4. 7. *I–V* curves of ESC (Ni–BCY25|BCY10|Pt) fueled with 42.9% NH_3–*x*% H_2O–(57.1–*x*)% Ar (*x*, water content); cathode gas: O_2; temperature: 600^oC.

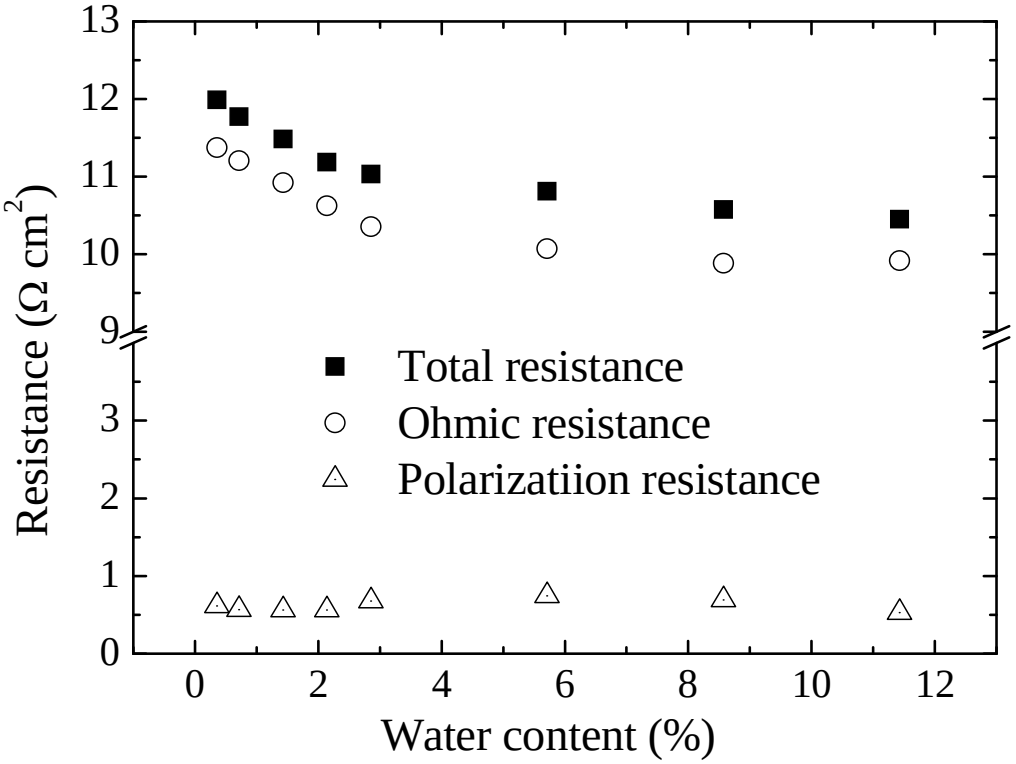

Figure 4. 8. Total, ohmic, and polarization resistances under the open circuit state of ESC: Ni–BCY25|BCY10|Pt fueled with 42.9% NH_3–*x*% H_2O–(57.1–*x*)% Ar (*x*, water content); cathode gas: O_2; temperature: 600^oC.

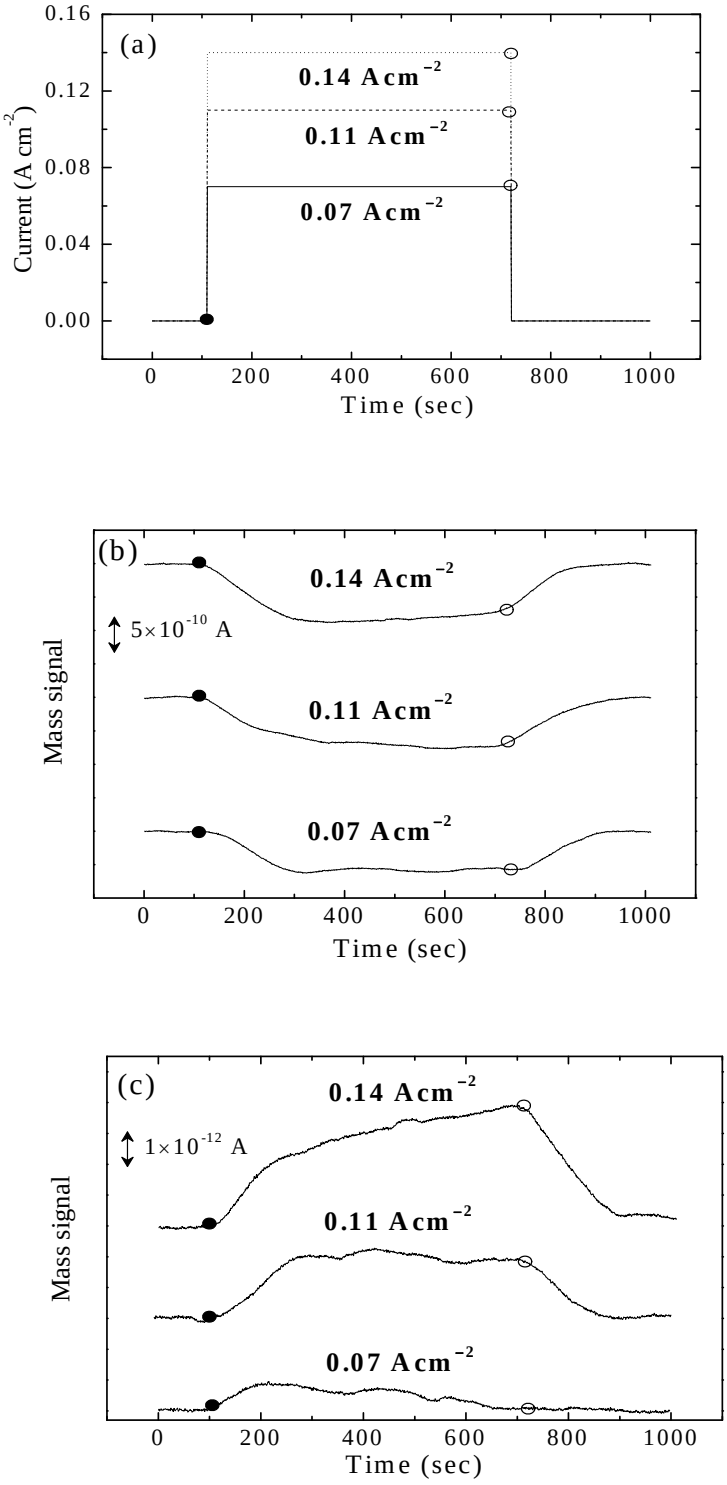

Figure 4. 9. (a) ESC was operated under galvanostatic condition of 0.07, 0.11, and 0.14 A cm^{-2} at 600^{o}C and the mass signals of (b) H_2 and (c) N_2 in the anode off–gas was monitored in response to current loading; solid and open circles represent current on and off,

respectively; anode gas: 42.9% NH_3–1.4% H_2O–55.7% N_2; cathode gas: O_2.

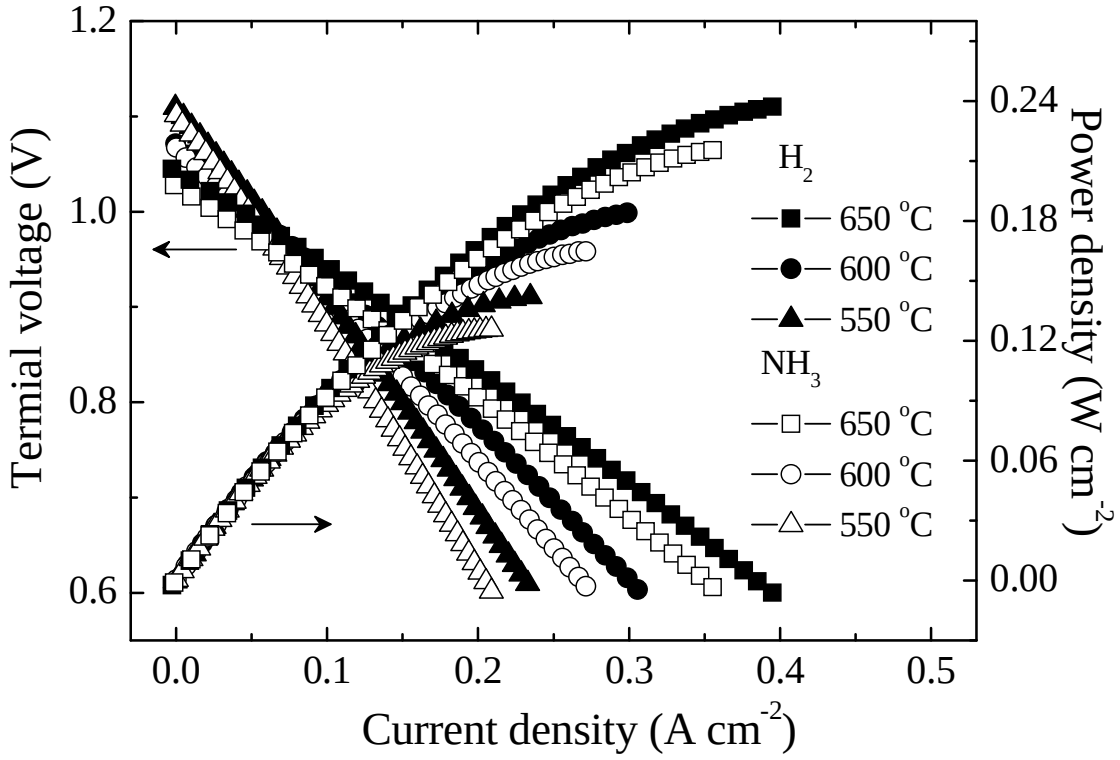

Figure 4. 10. *I–V* curves of ASC at 550–650°C: Ni–BCY25|BCY10|SSC fueled with 45.0% H_2–1.0% H_2O–54.0% N_2 and 42.9% NH_3–1.4% H_2O–55.7% N_2; cathode gas: O_2

Chapter 5

A Stability Study of Ni–Yttria-Stabilized Zirconia Anode for Direct Ammonia Solid Oxide Fuel Cells

5. 1. Introduction

The rapidly increasing fossil fuel consumption is regarded as the main reason of global warming, leading to an urgent demand for low carbon energy technologies. Power generation technologies using hydrogen can avoid carbon emission during electricity production. However, the technological difficulties in storage and transportation of hydrogen cause significant cost and safety risk and thus limit its wide application. Comparing with hydrogen, ammonia has many advantages such as low cost, high volumetric energy density, and ease to be liquefied under mild conditions. Recently, a carbon–free energy strategy using ammonia as a hydrogen carrier has been attracting considerable interest: Hydrogen is produced by water splitting driven by electricity or solar power, and then utilized for the synthesis of ammonia through Haber–Bosch process. Ammonia can be conveniently stored and transported in the liquid state. Finally, ammonia is consumed directly or indirectly for the power generation. Carbon emission is expected to be significantly reduced by creating such an energy chain [1].

In the past decade, a great effort has been devoted by many groups on developing power generation systems using ammonia as a fuel, such as combustion engines, fuel cells, and gas turbines, etc. [2–5]. Among them, solid oxide fuel cells directly fueled with ammonia have been frequently reported [6].

The operating temperature of SOFCs is as high as 550–750^{o}C due to the use of solid oxide electrolytes. At this temperature range, ammonia tends to be decomposed into nitrogen and hydrogen over Ni–based cermet anodes. Several studies have demonstrated the promising initial performance of conventional SOFCs using doped zirconia electrolytes [7–12]. For example, Ma *et al*. reported a maximum power density of 299 mW cm^{-2} at 750^{o}C for a direct ammonia–fueled SOFC with the configuration of Ni–YSZ|YSZ|$La_{0.5}Sr_{0.5}MnO_{3+\delta}$–YSZ [10]. However, detailed studies on the long–term stability of direct ammonia SOFCs are still

lacked in the literatures.

In our previous work, it was demonstrated that the utilization of ammonia over Ni–YSZ cermet anode proceeded in two steps [13]. Ammonia diffuses into anode chamber and then decomposes to nitrogen and hydrogen. Subsequently, the generated hydrogen is electrochemically oxidized to produce steam and electron. At low temperature region where ammonia cannot be completely decomposed, the Ni–YSZ anode is actually exposed to a gaseous mixture of N_2, H_2, H_2O, and NH_3. In this case, the surface of nickel might be nitrided by the remained ammonia, leading to a volumetric change of Ni particles [14, 15]. This possibility brings a risk to the long–term stability of direct ammonia SOFCs with Ni–YSZ cermet anode. In this work, therefore, an ammonia fuel was directly supplied to an anode–supported button cell (ASC) with Ni–YSZ cermet anode. The influence of nickel nitriding in ammonia atmosphere on electrochemical performance, microstructure, and long–term stability of the ASC were investigated in details.

5. 2. Experimental

5. 2. 1. Electrochemical tests on ASC

An anode–supported button cell (ASC, Noritake Co. Ltd.) was used in this work. The information of ASC is summarized in Table 5.1. The ASC was sandwiched with alumina tubes and sealed by Pyrex glass rings, as is described in our previous report [13]. A platinum mesh was attached closely to the electrode for the current collection. Prior to electrochemical tests, the anode was reduced in 85.0% N_2–15.0% H_2 at 700^{o}C for 1 h. Then, the fuel gas was supplied to the Ni–YSZ anode. If not specified otherwise, the composition and total flow rate of the ammonia containing fuel were 66.7% NH_3–1.7% H_2O–31.6% N_2 and 60 ml min^{-1}, respectively. If the ammonia fuel with this composition and flow rate decomposes completely, the resultant gas would be 60.0% H_2–1.0% H_2O–39.0% N_2 with a total flow rate of 100 ml min^{-1}. This hydrogen-containing mixture gas was also used as a fuel for comparison. The oxygen was supplied as a cathode gas with a flow rate of 100 ml min^{-1}. The open–circuit voltages (OCVs), impedance spectra, and current–voltage (*I–V*) characteristics of ASC fueled with the two kinds of fuels described above were measured at 600^{o}C and 700^{o}C using the

solartron analytical 1400/1470E cell test system. In order to investigate the stability of Ni–YSZ anode under an ammonia atmosphere, the ammonia–fueled ASC was held at the open circuit state. During this holding period, the OCV and impedance spectra were recorded. Then, the outer surface of Ni–YSZ anode before and after the holding test was observed by a scanning electron microscope (SEM, Nvision 40, Carl Zeiss–SIINT) equipped with energy dispersive X–ray spectrometer (EDX, Inca x–act, Oxford Analytical Instruments).

In addition, a temperature cycling test was carried out on the ASC. The cell was held at 700^{o}C for 1 h. Then, the temperature was decreased to 600^{o}C within 15 min and held at 600^{o}C for 1 h. Subsequently, the temperature was raised back to 700^{o}C within 15 min. This process was repeated 8 times. During the temperature cycling test, oxygen with a flow rate of 100 ml min^{-1} was supplied to the cathode. Hydrogen or ammonia fuels were supplied to the anode, and the OCV was recorded as a function of time. The cell performance before and after the temperature cycling test was evaluated by *I–V* characteristics and impedance spectroscopy. After the electrochemical tests, the cell was cooled down with the same cathode and anode gases to room temperature within 2 h.

5. 2. 2. Catalytic study on Ni–YSZ cermet powder nitrided in NH_3

The effect of nitriding treatment on the microstructure of Ni–YSZ cermet powder was investigated. NiO (Wako Pure Chemical Industries, Ltd.) and YSZ ($(Y_2O_3)_{0.08}$–$(ZrO_2)_{0.92}$; Tosoh Corp.) with a volume ratio of 1:1 was mixed and then calcined at 1400^{o}C for 5 h. The resultant mixture was sufficiently ground and uniaxially pressed into a pellet at 50 MPa. Then, the pellet was pulverized to 7–11 mesh. 0.3 g of the sample was set in a quartz tube and heated to 600^{o}C at a rate of 30^{o}C min^{-1}. After that pure NH_3 was flowed to the sample for 1 h, followed by Ar flow for 1 h to expulse the residual NH_3. Subsequently, the temperature was raised to 700^{o}C at a rate of 10^{o}C min^{-1}. The outlet gas was monitored by a mass spectrometer (OmniStar GSD 320, Pfeiffer Vacuum AG). In another experiment, the Ni–YSZ cermet powder was heated to the designated temperatures (500^{o}C, 600^{o}C, and 700^{o}C) and nitrided in NH_3. After the expulsion of remained NH_3 by Ar, H_2 was supplied. During these experiments, the outlet gas was continuously analyzed by a mass spectrometer. The flow rate of Ar, H_2, and

NH_3 was always set at 30 mL min^{-1}.

5. 2. 3. Characterization of Ni film on YSZ disk nitrided in NH_3

In order to investigate the morphological change of Ni surface due to the nitriding treatment in ammonia, the Ni film with an area of 1 cm^2 was fabricated on the YSZ disc (8 mol.% Y_2O_3–92 mol.%ZrO_2, Tosoh Corp; thickness: 500 µm, diameter: 24 mm) by radio frequency sputtering (Showa Shinku SPH–04H; power 60 W for 4.5 h) in 0.5 Pa of Ar atmosphere. The Ni film on YSZ disk was heated at 700°C for 1 h in air and then reduced in 85% N_2–15% H_2 to obtain the sintered Ni film with a thickness of *ca*. 150 nm. The obtained YSZ disk was set in the same apparatus for the electrochemical measurement of ASC. The NH_3 gas (100 ml min^{-1}) was supplied to the Ni film side for 1 h, followed by cooled down in an NH_3 flow to room temperature within 2 h. The Ni film before and after nitriding treatment was characterized by X-ray diffraction analysis (XRD, Rigaku, Ultima IV X-ray diffractometer) and SEM.

5. 3. Results and discussion

The initial performance of the cell fueled with hydrogen and ammonia is shown in Fig. 5. 1. In an ammonia fuel, the cell performance as well as OCV was lower than that in a hydrogen fuel regardless of temperature. This result was consistent with that obtained for electrolyte–supported cells [13]. The hydrogen generated from ammonia decomposition over Ni–YSZ cermet anode is consumed as a main fuel and the influence of residual ammonia on OCV can be neglected [13]. If ammonia decomposed completely, the final compositions of ammonia–and hydrogen–containing anode gases would be exactly the same. Otherwise, the hydrogen concentration in the ammonia–containing fuel was less than that in the hydrogen fuel. This explains the difference in the cell performance and OCVs for ammonia and hydrogen anode gases. Note that the maximum power density of the ASC fueled with ammonia was *ca*. 325 mW cm^{-2} at 700°C.

In order to investigate the stability of direct ammonia–fueled ASC under the open circuit state, ammonia was supplied to the cell at 600°C and 700°C. Figure 5. 2 shows the OCV

recorded as a function of time. The OCV at 700°C increased slightly for the first few minutes (*ca*. 3 mV) and then decreased at a very slow rate. At 600°C, the OCV increased from 1.043 V to 1.067 V within the initial 1 h, and then was quite stable until *ca*. 15 h. After that the OCV started to oscillate with a range of *ca*. ± 5 mV. The reason for this oscillation has not been elucidated at the current state.

The cell performances before and after OCV holding for 24 h in an ammonia atmosphere at 700°C and 600°C are shown in Figs. 5. 3 and 5. 4, respectively. Note that the OCV, *I*–*V* curves, and impedance spectra were measured in the NH_3 fuel. The long-term exposure to NH_3 at 700°C resulted in apparent performance degradation especially at lower terminal voltage. Furthermore, polarization and ohmic resistances increased at first and then reached a stable state. However, the tendency was obviously different at 600°C, as can be seen in Fig. 5. 4(a). After exposure to ammonia at 600°C, the current density increased slightly at a high terminal voltage region but reached almost the same value at a low voltage region. Moreover, Fig. 5. 4(b) shows that an increase in polarization resistance mainly occurred at a low frequency region while the ohmic resistance remained almost unchanged for 24 h. Since impedance spectra were measured at OCV, an enlargement in spectrum was consistent with a change in the slope at a high voltage region of *I*–*V* curves in Fig. 5. 4(a). A series of changes in the cell performance and impedance spectra were reproducible.

The SEM images of the outer surface of Ni–YSZ anode before and after exposure to ammonia for 24 h are shown in Fig. 5. 5. Fig. 5. 5(a) shows that the surface of as–reduced Ni particle was smooth. However, after the heat treatment in an ammonia atmosphere at 700°C, the surface of Ni particles was considerably roughened and many pores with a diameter less than 100 nm were observed (see Fig. 5. 5(b)). It is reasonable to conjecture that the contact between Ni and YSZ particles were weakened due to the formation of nickel nitride, resulting in the increase of ohmic resistance. Analogous pores were also found on Ni particles subjected to an exposure to ammonia fuel at 600°C (see Fig. 5. 5(c)). Moreover, the Ni particles in Fig. 5. 5(c) were apparently sintered and its surface was significantly roughened as compared to those in Figs. 5. 5(a) and (b). The EDX results in Fig. 5. 5(d) suggested the existence of nitrogen element on Ni surface at the designated points in Figs. 5. 5(b) and (c),

and the intensity of nitrogen for the Ni particle annealed at 600°C was higher than that for 700°C. These results strongly imply the occurrance of nickel nitriding. Thus, the formation and decomposition processes of nickel nitride on Ni–YSZ cermet in an ammonia atmosphere were further investigated by mass spectroscopy. The Ni–YSZ powder annealed at 600°C in an ammonia flow was heated to 700°C at a rate of 10°C min^{-1} in Ar. The mass signals of outlet gas was monitored during heating and shown in Fig. 5. 6. The mass signal of N_2 in the outlet gas increased gradually with arising temperature while those of NH_3 and H_2 remained unchanged. N_2 should be generated from the decomposition of nickel nitride, which was formed during annealing in ammonia at 600°C.

In order to investigate the effect of temperature on the nitridation of nickel, the Ni–YSZ powder was heated in NH_3 at 500–700°C. The obtained sample was reduced in H_2 at the same temperature of nitriding treatment and the outlet gas was monitored by a mass spectrometer. Figure 5. 7 shows the time courses of mass signal of NH_3 (mass/charge = 17) for the Ni–YSZ powder after the heat treatment in NH_3 at 500–700°C. At each temperature, when H_2 was supplied, the signal of NH_3 increased and then decreased back to the background level. The increment in NH_3 signal was prominent at lower temperature. Thus, it can be concluded that lower temperature is preferable for the nitriding of nickel.

The Ni–YSZ powders after annealing in an ammonia atmosphere for 5 h at 600°C were characterized by XRD analysis. However, only Ni and YSZ phases were detected, indicating that the amount of nickel nitride was quite small. This is because the ammonia conversion over Ni–YSZ cermet was very high, considering the high temperature and small gas space velocity (6000 L kg^{-1} h^{-1}). In this case, only a very small part of Ni–YSZ in the upstream contacted with pure ammonia, which subsequently decomposed to N_2 and H_2 soon. The ratio of NH_3 to H_2 in the reactant gas decreased rapidly along the flow direction. The generated H_2 prevented the nitriding of nickel in the downstream part. In order to better observe the structure and morphology of Ni before and after nitriding treatment at 600°C, the Ni film coated on YSZ disk was used instead of the Ni–YSZ cermet powder. Figure 5. 8 shows that the Ni film before nitriding treatment consisted of many small grains and the surface of each nickel grain was smooth. After nitriding treatment, the grain boundary of Ni disappeared,

accompanied with the formation of a number of nanosized pores. The Ni film after exposure to ammonia was characterized by XRD and the peaks ascribable to Ni_3N were detected (see Fig. 5. 9). This agrees with the Ni–N phase diagram proposed by Wriedt et al, which indicated that Ni_3N was the stable phase of nickel nitride in pure ammonia at 600°C [15].

Based on these results, it is concluded that Ni particles in Ni–YSZ cermet anode can be nitrided in a pure ammonia atmosphere as follows:

$$6Ni + 2NH_3 \rightarrow 2Ni_3N + 3H_2 \quad (5\text{–}1)$$

The decomposition of nickel nitride in a reducing atmosphere or at higher temperature proceeds according to equations (5–2) and (5–3), respectively.

$$3H_2 + 2Ni_3N \rightarrow 2NH_3 + 6Ni \quad (5\text{–}2)$$

$$2Ni_3N \rightarrow N_2 + 6Ni \quad (5\text{–}3)$$

Furthermore, it was confirmed that the nitriding of nickel caused the microstructural change of Ni–YSZ anode, of which extent was significantly influenced by the temperature. This phenomenon should be considered as a serious risk factor for a direct NH_3–fueled SOFC because the temperature vibration occurs frequently in practical SOFC power systems. In view of this, a temperature cycling test was performed on a direct NH_3–fueled SOFC to investigate the stability of Ni–YSZ anode against temperature change.

The temperature cycling operation was conducted on the ASC between 600–700 °C. For comparison, H_2 or NH_3 fuels were supplied to the anode and the OCVs were monitored as a function of time. Figure 5. 10 shows that the OCV for H_2 anode gas was constant at each temperature. In particular, the OCV at 600 °C was higher than that at 700 °C, which agreed well with thermodynamics. Within every single cycle for NH_3 anode gas, the OCV at 600 °C was lower than that at 700 °C due to the lower ammonia conversion over Ni–YSZ anode.

Moreover, the OCV decreased continuously with increasing cycle number. According to the *I–V* characteristics shown in Fig. 5. 11, the temperature cycling operation resulted in severe performance degradation for the ammonia–fueled cell.

After cooling to room temperature in H_2, the cell after temperature cycling test in H_2 was not damaged at all. However, in the case of the ASC fueled with NH_3, the support layer of Ni–YSZ anode was found to be destructed (as illustrated in Fig. 5. 12). The reproducibility of this phenomenon was confirmed. It is considered that the ammonia conversion increased rapidly along the direction from anode surface towards electrolyte/anode interface, resulting in an ammonia concentration gradient. At low temperature, Ni particles in the ammonia–rich region, which is a thin layer from the outer surface of anode towards electrolyte, was nitrided. At elevated temperatures, the formed nickel nitride far from the outer surface of anode was reduced to nickel again due to the enhanced ammonia conversion. When the temperature decreases, the reduced nickel particles are nitrided again. This process proceeds with a repeated volumetric change as well as stress change during the temperature–cycling test. As a result, the anode support layer is gradually damaged with an increase of cycle number, and eventually delaminated near the outer surface (see Fig. 5. 12). As a result, gas leakage occurs via the cracks and lowers the OCV.

5. 4. Conclusions

The influence of ammonia treatment on the electrochemical performance and microstructural change of Ni–YSZ anode was studied in details. After a long period of exposure to ammonia at a constant temperature, the performance of the ASC did not apparently change but the Ni surface on the outer surface of Ni–YSZ anode was significantly roughened. The fundamental studies on Ni–YSZ powder and Ni film deposited on YSZ disk revealed that Ni was partially nitridized under an ammonia atmosphere, which led to a considerable morphology change. Moreover, a temperature cycling test between 600^{o}C and 700^{o}C was conducted on an anode-supported cell fueled with hydrogen or ammonia. It was clarified that the nitriding phenomenon of Ni caused a partial delamination of the support layer of Ni–YSZ anode, leading to a severe degradation of the cell. These results in this work

are very important because there is a stability risk of practical SOFC systems with Ni–YSZ anode directly fueled with ammonia.

References

[1] L. Rong, J. Irvine, S. Tao, *Int. J. Hydrogen Energy*, **37**, 1482–1494 (2012).

[2] D. Miura, T. Tezuka, *Energy*, **68**, 428–436 (2014).

[3] J. Yang, H. Muroyama, T. Matsui, K. Eguchi, *J. Power Sources*, **245**, 277–282 (2014).

[4] C. Zamfirescu, I. Dincer, *J. Power Sources*, **185**, 459–465 (2008).

[5] Power generation from ammonia combustion by using gas turbine, http://www.aist.go.jp/aist_j/press_release/pr2014/pr20140918/pr20140918.html.

[6] J. Yang, A. Molouk, T. Okanishi, H. Muroyama, T. Matsui, K. Eguchi, *ACS Appl. Mater. Inter.*, **7**, 7406-7412 (2015).

[7] A. Wojcik, H. Middleton, I. Damopoulos, J. Van herle, *J. Power Sources*, **118**, 342–348 (2003).

[8] G. Fournier, I. Cumming, K. Hellgardt, *J. Power Sources*, **162**, 198–206 (2006).

[9] N. Dekker, G. Rietveld, *J. Fuel Cell Sci. Technol.*, **3**, 499–502 (2006).

[10] Q. Ma, J. Ma, S. Zhou, R. Yan, J. Gao, G. Meng, *J. Power Sources*, **164**, 86–89 (2007).

[11] L. Zhang, Y. Cong, W. Yang, L. Lin, *J. Catal.*, **28**, 749–751 (2007).

[12] G. Meng, C. Jiang, J. Ma, Q. Ma, X. Liu, *J. Power Sources*, **173**, 189–193 (2007).

[13] J. Yang, T. Akagi, T. Okanishi, H. Muroyama, T. Matsui, K. Eguchi, *Fuel cells*, **15**, 390-397 (2015).

[14] A. Alexander, J. Hargreaves, C. Mitchell, *Topics in Catalysis*, **55**, 1046-1053 (2012).

[15] H. Wriedt, *Bull. Alloy Phase Diagr.*, **6**, 558-563 (1985).

Table 5.1

The configuration of ASC.

Layers	Composition	Thickness (μm)	Diameter (mm)
Anode–support layer	NiO–YSZ	465–555	20.0
Anode functional layer	NiO–YSZ	5–10	20.0
Electrolyte layer	YSZ	4–6	20.0
Barrier layer	Gadolinium–doped ceria (GDC)	2–4	20.0
Cathode composition	$La_{0.6}Sr_{0.4}Co_{0.2}Fe_{0.8}O_{3-\delta}$ (LSCF)	30–60	12.5

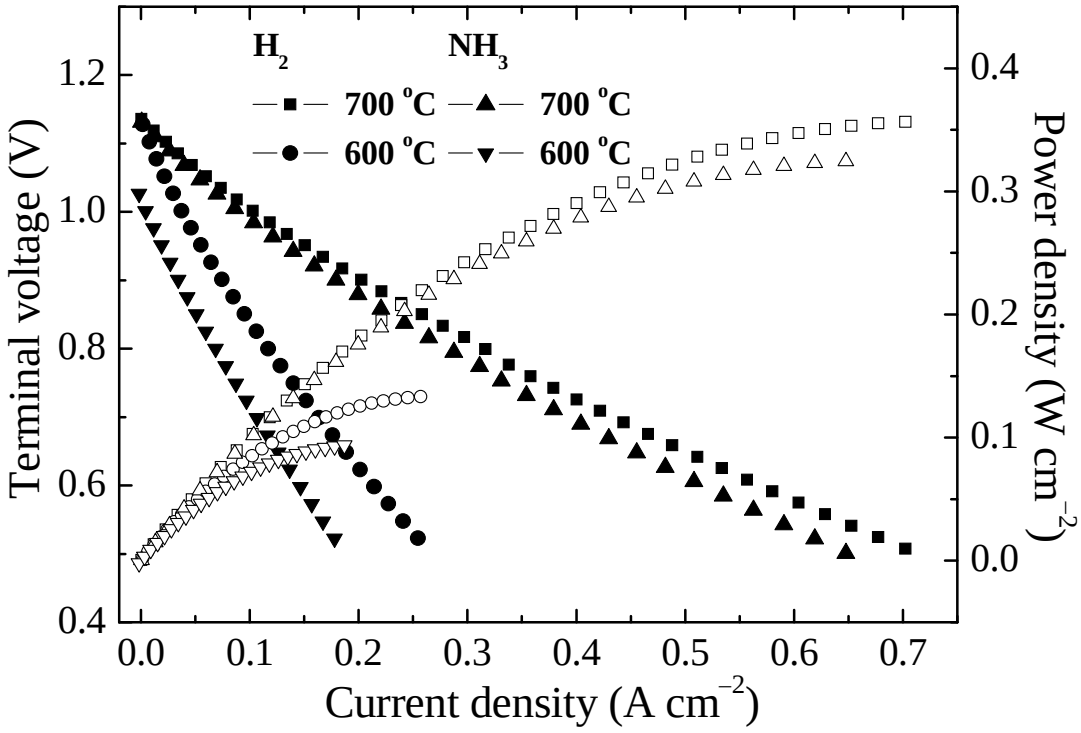

Figure 5. 1. *I–V* characteristics of the ASC at 600°C and 700°C fueled with 66.7% NH_3–1.7% H_2O–31.6% N_2 and 60.0% H_2–1.0% H_2O–39.0% N_2 gases; cathode gas: O_2.

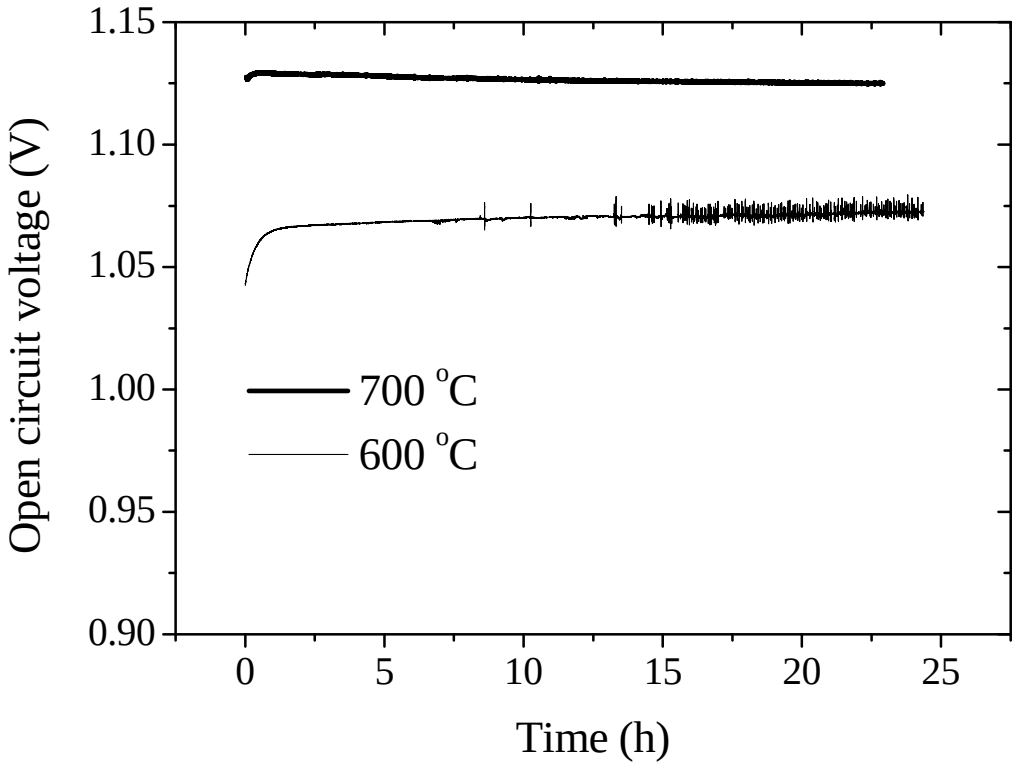

Figure 5. 2. Time courses of OCV of the ASC at 600°C and 700°C; cathode gas: O_2; anode gas: 66.7% NH_3–1.7% H_2O–31.6% N_2.

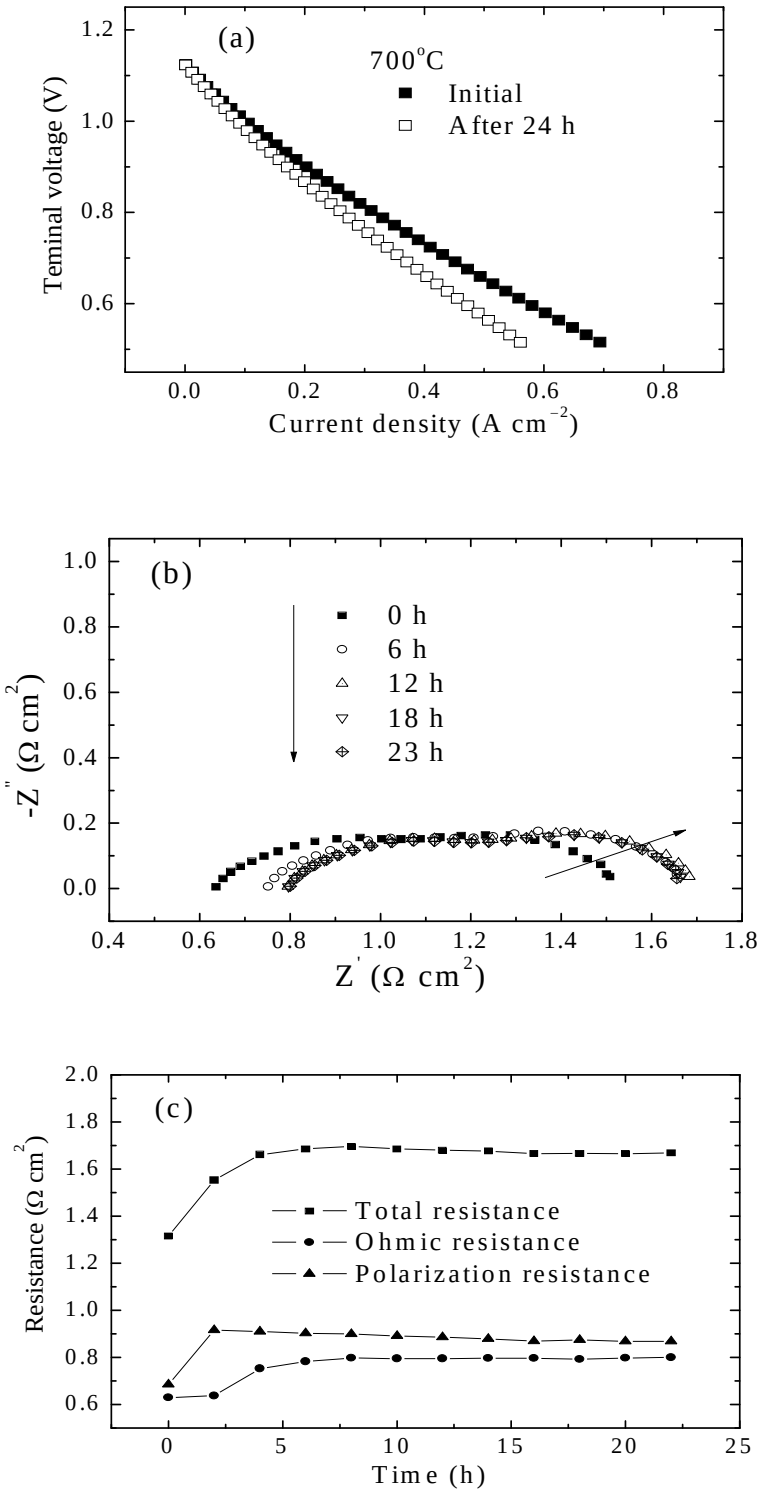

Figure 5. 3. (a) *I–V* characteristics and (b) impedance spectra of the ASC before and after fueled with 66.7% NH_3–1.7% H_2O–31.6% N_2 for 24 h at 700°C; the total, ohmic, and polarization resistances obtained from (b) are plotted as a function of time in (c); cathode: O_2.

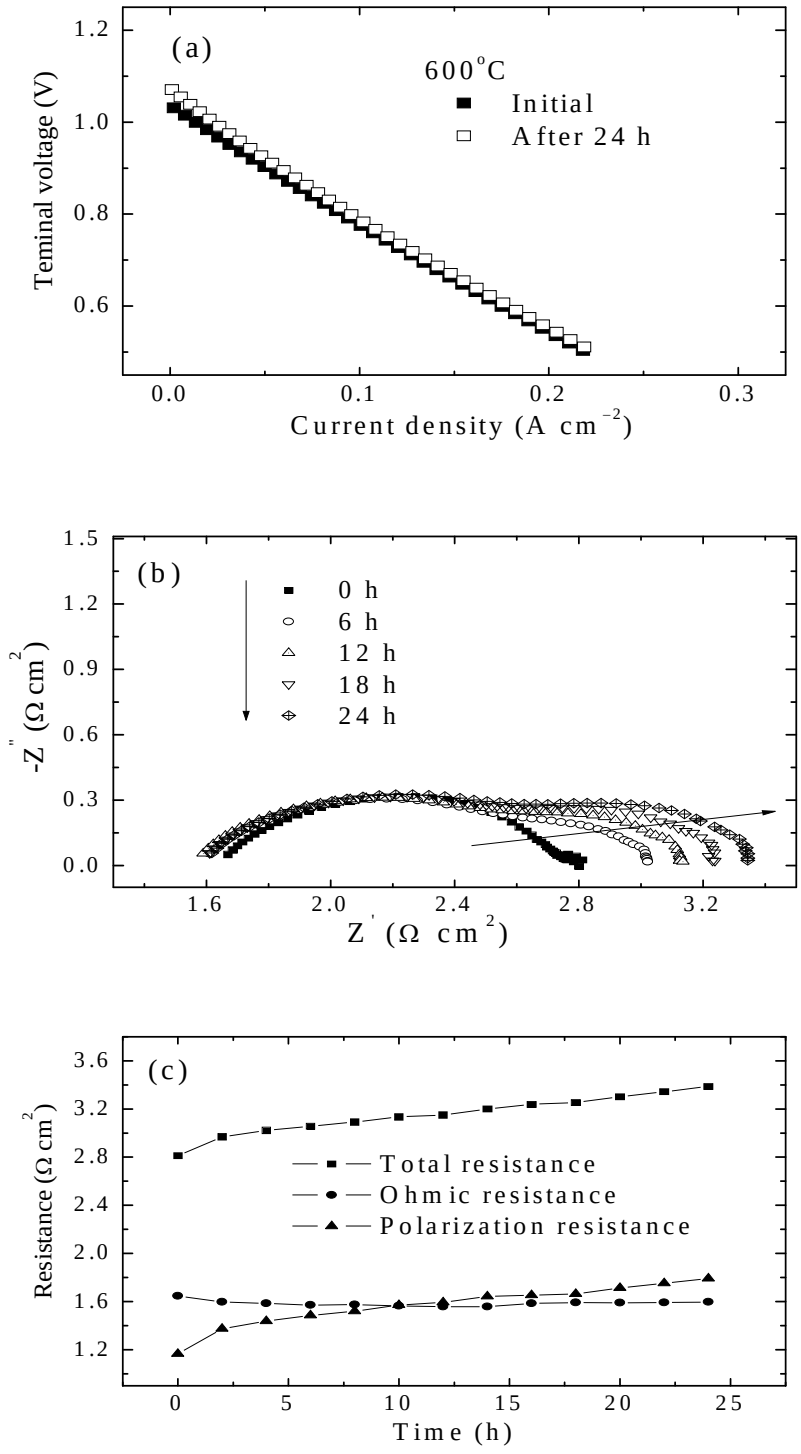

Figure 5. 4. (a) *I–V* characteristics and (b) impedance spectra of the ASC before and after fueled with 66.7% NH_3–1.7% H_2O–31.6% N_2 for 24 h at 600°C; the total, ohmic, and polarization resistances obtained from (b) are plotted as a function of time in (c); cathode: O_2.

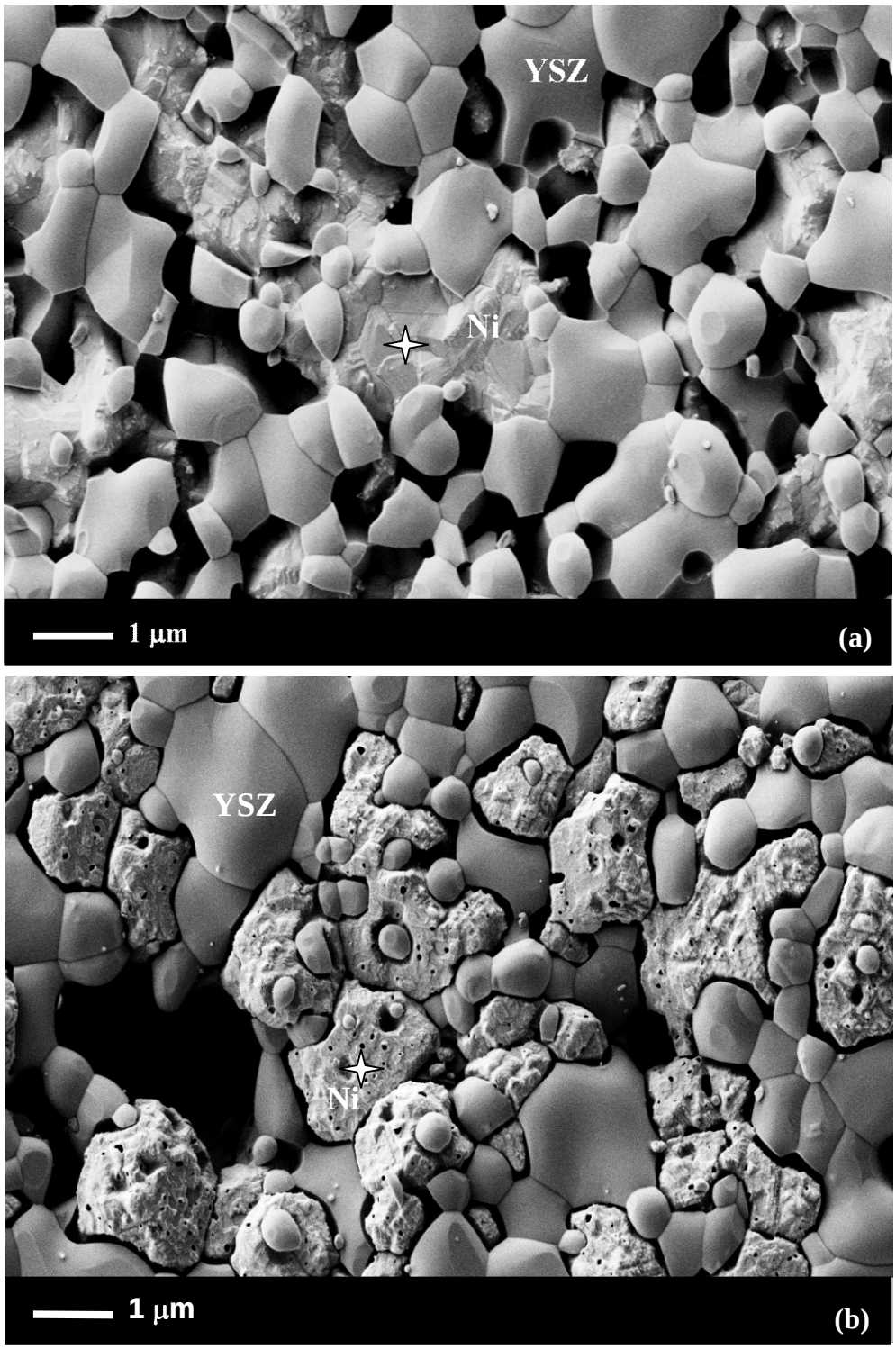

Figure 5. 5. SEM images of Ni–YSZ cermet anode surface (a) as–reduced in 15% H_2–85% Ar and (b) fueled with 66.7% NH_3–1.7% H_2O–31.6% N_2 at 700^oC for 24 h.

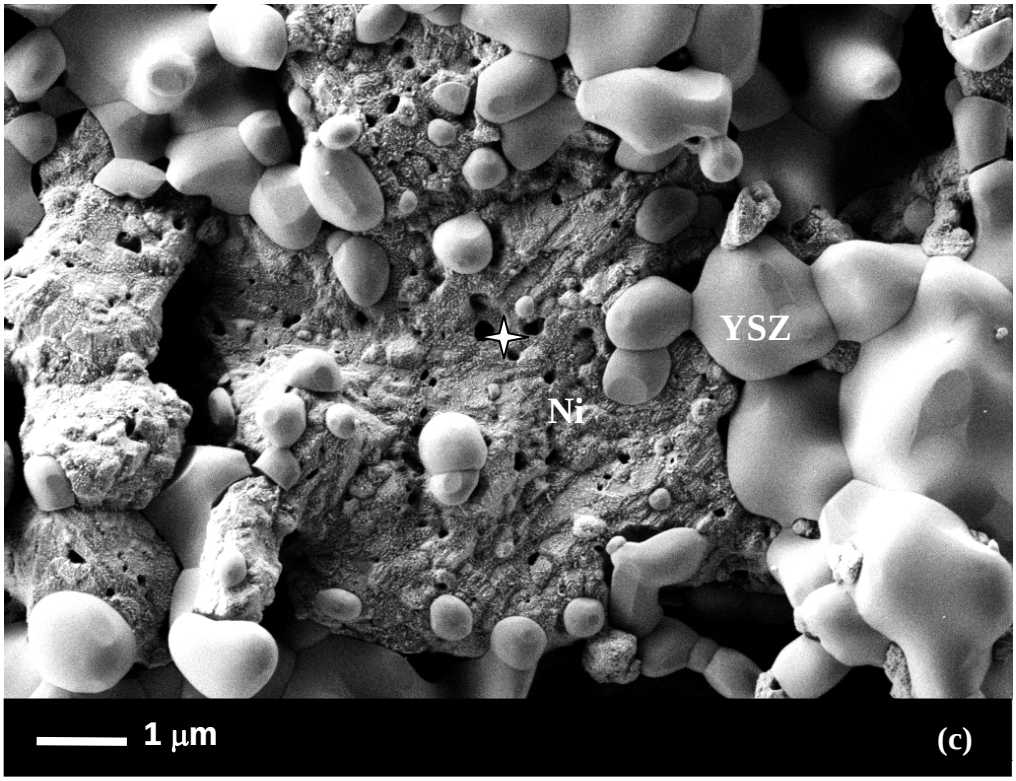

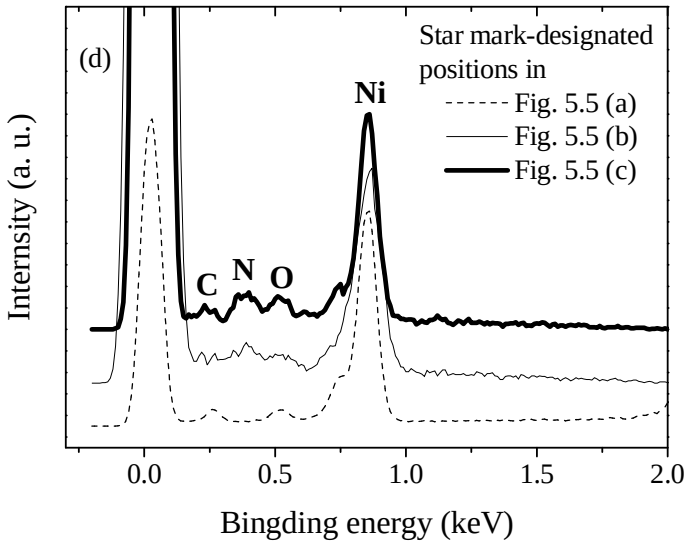

Figure 5. 5. SEM images of Ni–YSZ cermet anode surface (c) fueled with 66.7% NH_3–1.7% H_2O–31.6% N_2 at 600^oC for 24 h; (d) EDX spectra at the spots marked with a star in (a), (b), and (c).

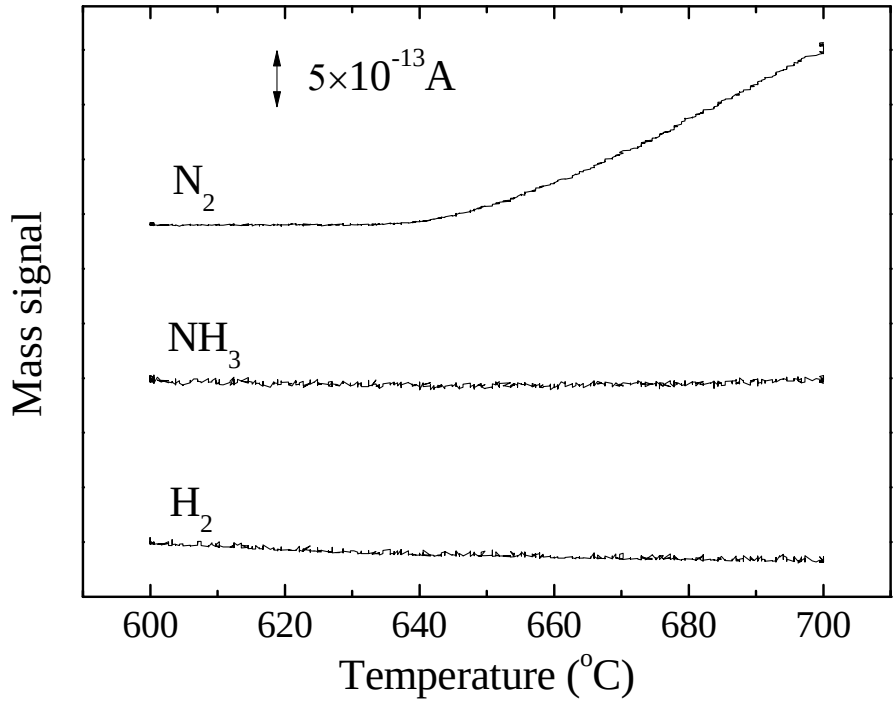

Figure 5. 6. Mass signals of N_2, NH_3, and H_2 for NH_3-treated Ni–YSZ powder during heating from 600°C to 700°C at a rate of 10°C min^{-1}; carrier gas: Ar (30 mL min^{-1}).

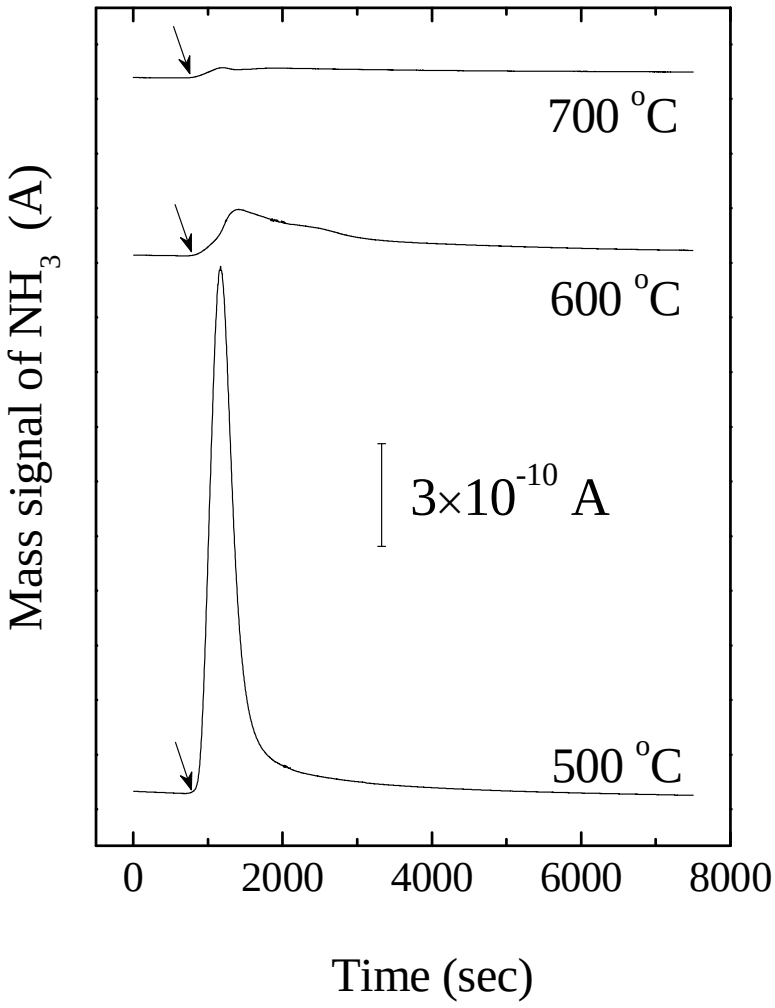

Figure 5. 7. Mass signal of NH_3 for the reduction of Ni–YSZ powder in H_2 at 700°C, 600°C, and 500°C; the arrows indicated the beginning of replacing Ar with H_2 flow; gas flow rate: 30 mL min^{-1}.

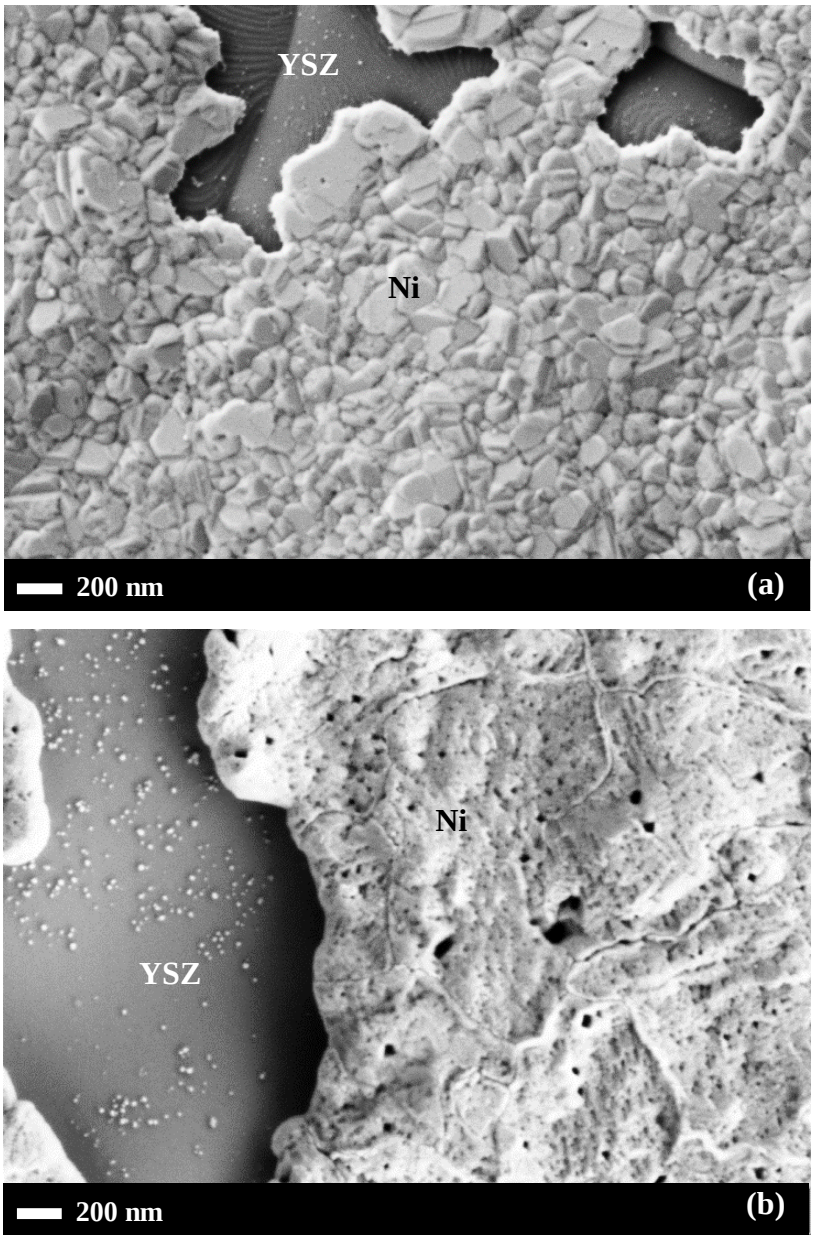

Figure 5. 8. SEM images of Ni film on YSZ disc (a) as reduced in H_2 at 600^{o}C and (b) after subsequent exposure to NH_3 for 5 h at 600^{o}C.

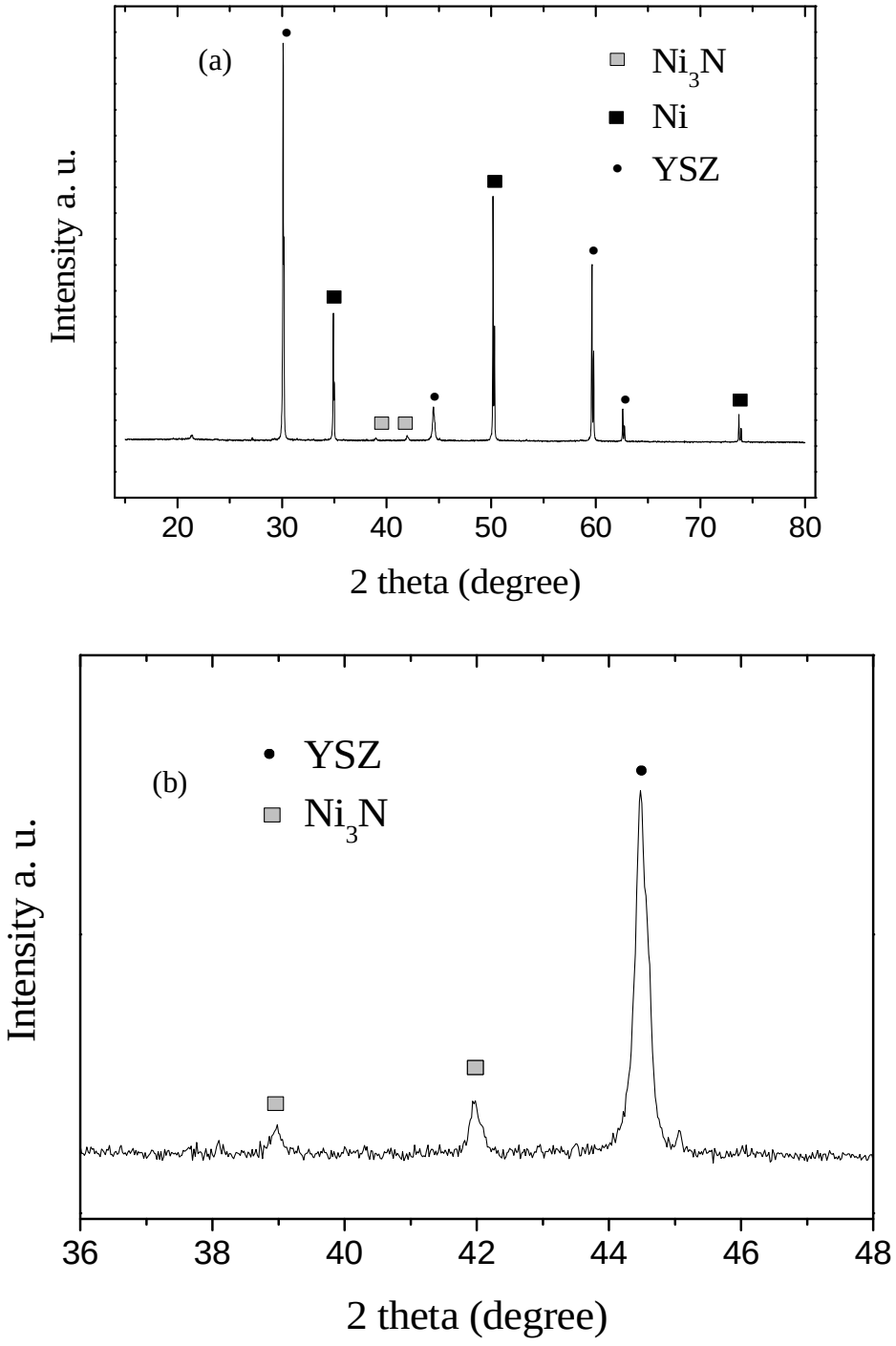

Figure 5. 9. (a) XRD pattern of Ni film on YSZ disc after exposed to NH_3 (100 ml min^{-1}) at 600°C for 1 h; (b) enlarged image of (a) from 36° to 48°.

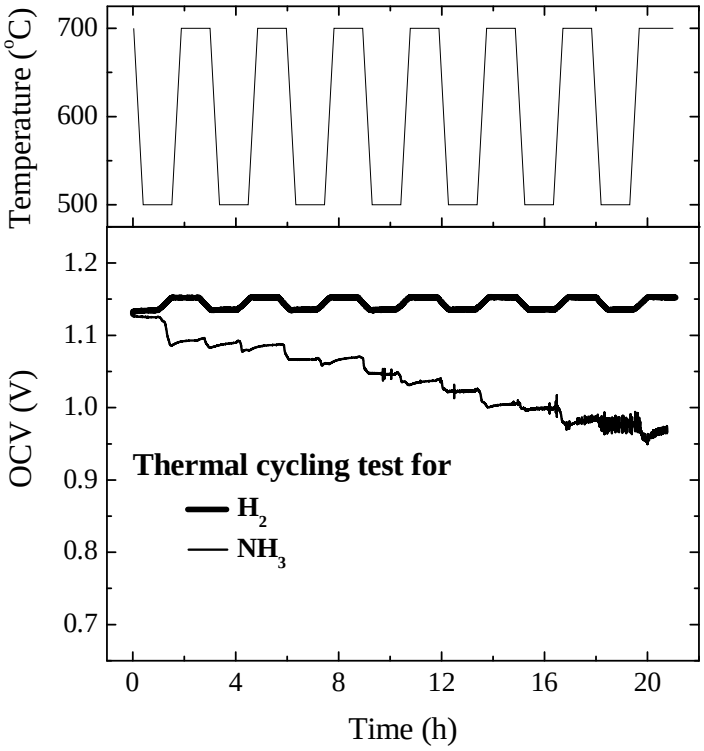

Figure 5. 10. Time courses of OCV of the ASC fueled with 60.0% H_2–1.0% H_2O–39.0% N_2 and 66.7% NH_3–1.7% H_2O-31.6% N_2 during thermal cycling tests; cathode gas: O_2.

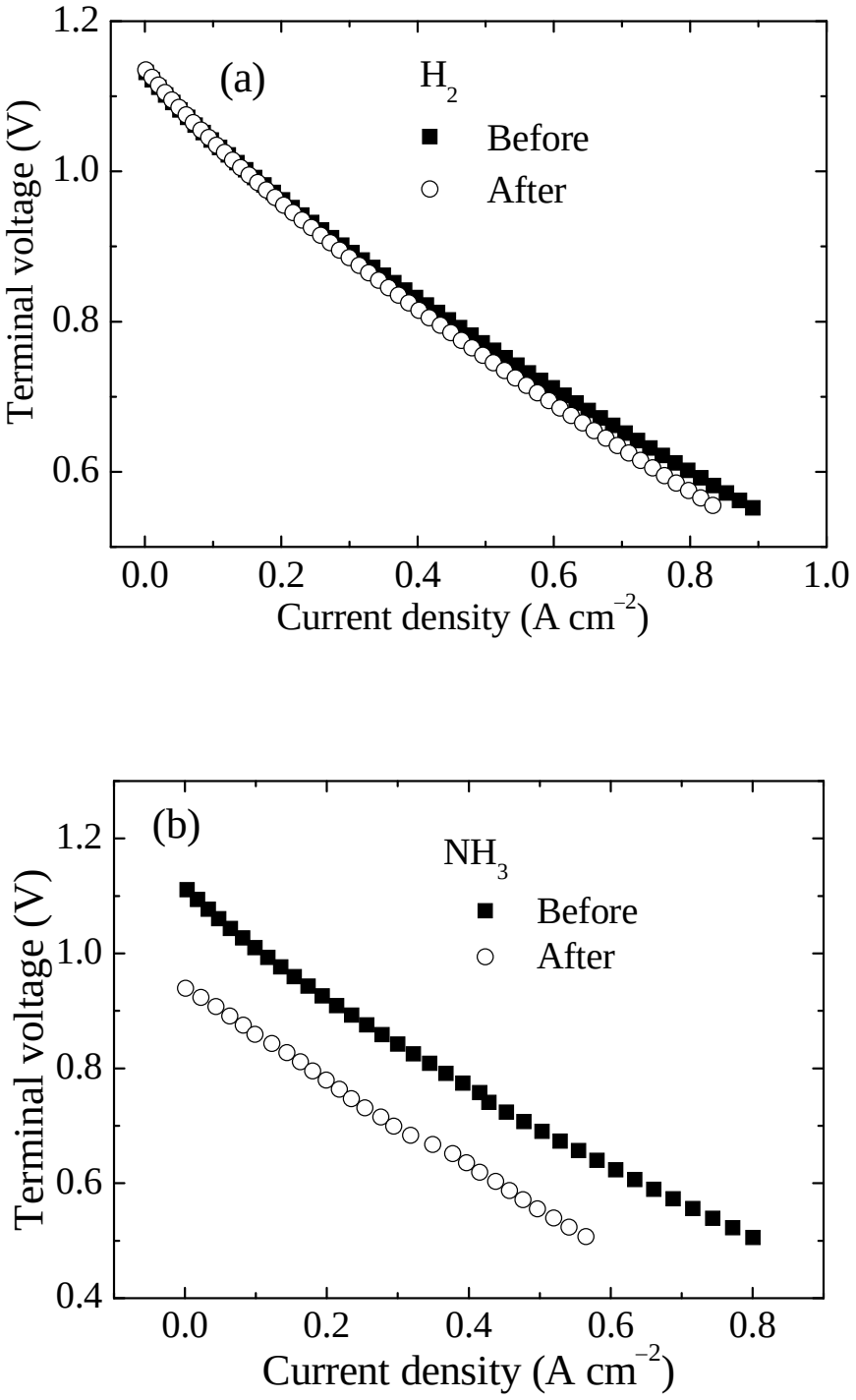

Figure 5. 11. *I-V* characteristics (measured at 700°C) of the ASC fueled with (a) 60.0% H_2-1.0% H_2O-39.0% N_2 and (b) 66.7% NH_3–1.7% H_2O–31.6% N_2 before and after the temperature cycle test in Fig. 10.

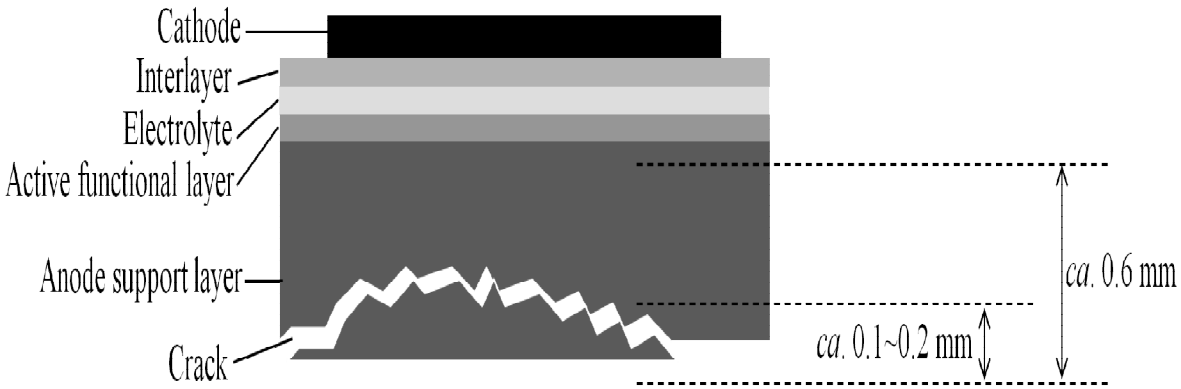

Figure 5. 12. Illustration of the ASC after the temperature cycling test in NH_3.

General conclusions

This thesis was dedicated to highlights the superiority and possibility of using ammonia directly as a fuel for solid oxide fuel cells. Understanding the ammonia utilization mechanism within SOFCs is one of the main goals of this work and is the only way to modify the anode for better performance of direct NH_3–fueled SOFCs.

In chapter 1, the electrochemical behaviour for the cell of Ni–YSZ | YSZ | LSM in wet hydrogen, ammonia, and methane fuels under almost the same partial pressure of oxygen at 500–800^oC was studied. The results revealed that the cell performance was significantly affected by fuel species and operating temperature. The single cell exhibited higher performance in wet NH_3 compared with that in wet CH_4 which was caused by the difference in the catalytic activity of anode for the hydrogen production. Thus, it was clarified that NH_3 is a preferable fuel rather than CH_4 for the direct use in SOFCs with using a Ni–YSZ anode. Furthermore, the kinetics study on ammonia decomposition over a Ni–YSZ anode was conducted at 600^oC. Although the ammonia decomposition increased with increasing ammonia concentration, the decomposition rate was reduced in the presence of hydrogen in the reactant gas. Such a behavior was not confirmed at 850^oC.

In chapter 2, the catalytic activity of both Ni–YSZ and Ni–GDC for ammonia conversion was measured. The cermet of Ni–GDC showed higher catalytic activity for ammonia decomposition than Ni–YSZ. In response to this, the performance of a direct NH_3–fueld SOFC was improved by using Ni–GDC anode. The hydrogen concentration produced from ammonia decomposition at the limiting current region over Ni–GDC was higher compared with that over Ni–YSZ. For the better understanding of the superiority of Ni–GDC anode for direct NH_3–fueld SOFCs, the surface basicity of GDC and YSZ was estimated and GDC demonstrated higher number of basic sites. Such a behaviour enhances the ammonia

conversion rate over Ni–GDC compared with Ni–YSZ. On the other hand, the analysis of anode microstructure revealed that GDC prevented the sintering of nickel particles under operating conditions. Moreover, the cell performance and the catalytic activity for ammonia decomposition were further enhanced with applying Ni−GDC anode synthesised by the glycine–nitrate combustion process. These results revealed that the high performance of Ni–GDC anode for the direct NH_3–fueled SOFC resulted from its mixed ionic– electronic conductivity as well as high catalytic activity for ammonia decomposition.

In chapter 3, in order to enhance the performance of direct NH_3–fueled SOFCs, catalytic activities of metal (Pd, Ru, Rh, Mo, Fe, and Ir) promoted Ni–GDC for ammonia decomposition were investigated. The ammonia decomposition over Ru–promoted Ni–GDC catalyst was the highest among the studied metal modified Ni–GDC. Therefore, Ru–promoted Ni–GDC anode was prepared by the infiltration technique and the electrochemical performance was studied and compared with that of Ni–GDC and Fe–promoted Ni–GDC anodes with a supply of hydrogen and ammonia. The polarization resistance for Ni–GDC anode slightly decreased with an addition of 3 wt% of Ru in hydrogen, whereas that in ammonia reduced significantly reduced at 600^{o}C. The reduction of anodic polarization resistance in presence of Ru was particularly pronounced when using ammonia fuel. The open circuit voltage of ammonia–fueled SOFC was elevated by increasing Ru loading at 600^{o}C. The addition of Ru to Ni–GDC anode promoted the ammonia decomposition reaction and the infiltration technique is a promising method for enhancing the anode performance for direct NH_3–fueled SOFCs.

In chapter 4, Ni–$BaCe_{0.75}Y_{0.25}O_{3-\delta}$ was investigated as an anode for direct ammonia-fueled SOFCs. The catalytic activity of Ni–BCY25 for ammonia decomposition was found to be remarkably higher than Ni–YSZ and Ni–GDC. The poisoning effect of water and hydrogen on ammonia decomposition reaction over Ni–BCY25 was confirmed. In

addition, an electrolyte–supported SOFC employing $BaCe_{0.90}Y_{0.10}O_{3-d}$ (BCY10) electrolyte and Ni–BCY25 anode was fabricated, and its electrochemical performance was investigated at 550–650^{o}C with feeding ammonia and hydrogen fuel gases. The effect of water content in the anode gas on the cell performance was also studied. Based on these results, it was concluded that Ni–BCY25 was a promising anode for direct ammonia–fueled SOFCs. An anode–supported single cell denoted as Ni–BCY25|BCY10|$Sm_{0.5}Sr_{0.5}CoO_{3-\delta}$ was also fabricated, and maximum powder density of 216 and 165 mW cm^{-2} was achieved at 650 and 600^{o}C, respectively.

In chapter 5, ammonia fuel was supplied to the Ni–YSZ cermet anode at 600^{o}C and 700^{o}C and the changes of electrochemical performance and microstructure under the open-circuit condition was studied in details. The influence of ammonia exposure on the microstructure of Ni was also investigated by using Ni–YSZ powder and Ni film deposited on YSZ disk. The obtained results demonstrated that Ni in the cermet anode was partially nitrided under an ammonia atmosphere, which considerably roughened the Ni surface. Moreover, the destruction of anode support layer was confirmed for the anode-supported cell (ASC) upon the temperature cycling test between 600^{o}C and 700^{o}C because of the nitriding phenomenon of Ni, resulting in severe performance degradation.

Ultimately, the author hopes this systematic study contributes strongly to the progress in the development of anode for direct ammonia–fueled solid oxide fuel cells.

Publication list

Chapter 1

Electrochemical and Catalytic Behaviors of Ni–YSZ Anode for the Direct Utilization of Ammonia Fuel in Solid Oxide Fuel Cells.

Ahmed Fathi Salem Molouk, Jun Yang, Takeou Okanishi, Hiroki Muroyama, Toshiaki Matsui, and Koichi Eguchi

Journal of the Electrochemical Society, **162**, F1268-F1274 (2015).

Chapter 2

Comparative Study on Ammonia Oxidation Over Ni-based Cermet Anodes for Solid Oxide Fuel Cell.

Ahmed Fathi Salem Molouk, Jun Yang, Takeou Okanishi, Hiroki Muroyama, Toshiaki Matsui, and Koichi Eguchi

Journal of Power Sources **305**, 72–79 (2016).

Chapter 3

Ruthenium–promoted Nickel–ceria Anode Prepared by Infiltration Technique for Direct Ammonia Solid Oxide Fuel Cells

Ahmed Fathi Salem Molouk, Takeou Okanishi, Hiroki Muroyama, Toshiaki Matsui, and Koichi Eguchi

To be submitted.

Chapter 4

Electrochemical and Catalytic Properties of Ni–$BaCe_{0.75}Y_{0.25}O_{3-\delta}$ Anode for Direct Ammonia–fueled Solid Oxide Fuel Cells

Jun Yang, Ahmed Fathi Salem Molouk, Takeou Okanishi, Hiroki Muroyama, Toshiaki Matsui, and Koichi Eguchi

ACS Applied Materials & Interfaces, **7**, 7406–7412 (2015).

Chapter 5

A Stability Study of Ni–Yttria-Stabilized Zirconia Anode for Direct Ammonia Solid Oxide Fuel Cells

Jun Yang, Ahmed Fathi Salem Molouk, Takeou Okanishi, Hiroki Muroyama, Toshiaki Matsui, and Koichi Eguchi

ACS Applied Materials & Interfaces (DOI: 10.1021/acsami.5b11122) (2015).

Other publication list

Electrochemical and Catalytic Behavior of Ni-based Cermet Anode for Ammonia-Fueled SOFCs

Ahmed Fathi Salem Molouk, Jun Yang, Takeou Okanishi, Hiroki Muroyama, Toshiaki Matsui, and Koichi Eguchi

ECS Transactions, **68**, 2751-2762 (2015).

Some β-Aminoketone Derivatives as Corrosion Inhibitors for Nickel in Hydrochloric Acid Solution.

G.Y. Elewady, A.H. El-Askalany and A.F. Molouk

Portugaliae Electrochimica Acta, **26/6**, 503-516 (2008).

Acknowledgments

I would like to thank everyone who supports me in the doctoral working period during 2013-2016 in the Department of Energy and Hydrocarbon Chemistry, Graduate School of Engineering, Kyoto University.

First and foremost, I wish to express my sincere gratitude to my advisor *Professor Koichi Eguchi*, Department of Energy and Hydrocarbon Chemistry, Graduate School of Engineering, Kyoto University, for accepting me into his group and the continuous support of my Ph.D study and related research, for his patience, motivation, and immense knowledge. His guidance helped me in all the time of research and writing of this thesis. I could not have imagined having a better advisor and mentor for my Ph.D study.

I would like to thank my examiner committee *Professor Takeshi Abe, and Professor Hiroshi Kageyama* Department of Energy and Hydrocarbon Chemistry, Graduate School of Engineering, Kyoto University for being examiners of the thesis and for their constructive discussion.

My sincere thanks also goes to *Associate Professor Toshiaki Matsui*, *Assistant professor Hiroki Muroyama*, and *Research Assistant Professor Takeou Okanishi* Department of Energy and Hydrocarbon Chemistry, Graduate School of Engineering, Kyoto University, for their precious advices and precise guidance. I would thank *Dr. Jun Yang* for his fruitful cooperation and helpful suggestion. I thank all the members in Eguchi lab for their stimulating discussions and friendly environment. The financial support by the Egyptian Ministry of Higher Education, Mission section, and Mansoura University Faculty of Science Chemistry Department are gratefully acknowledged. Furthermore, I will never forget the support and kindness which I received from all the members of Egyptian Cultural and Educational Bureau in Tokyo.

Last but not the least; I would like to address my deep thanks and appreciation to my beloved wife *Mona Askar*, parents *Fathi Molouk* and *Sohir Hwidy*, brothers *Mohamed Molouk* and *Mahmoud Molouk*, my kids, and all my friends in Arab communities in Japan for supporting me spiritually throughout writing this thesis and my life in general.

Ahmed Fathi Salem Molouk

2016